

POLITECNICO DI TORINO

DEPARTMENT OF CONTROL AND COMPUTER ENGINEERING

Master degree course in Mechatronic Engineering

Master Degree Thesis

Investigation on short circuit severity for Li-ion batteries under mechanical abuses and its empiric model development



Supervisor
Prof.ssa Silvia Bodoardo

Cosupervisor
Prof. Marcello Chiaberge

Company Supervisor
Dott. Mag. Luigi Aiello

Candidate
Mariagrazia Montaruli
ID Number: 254530

Academic Year 2019/2020

Table of contents

Introduction.....	I.
1. Literature review on Lithium-ion batteries.....	1
1.1 Working principle of a lithium-ion cell (chemical aspects).....	1
1.2 Main electrochemical processes.....	2
1.2.1 Solid Electrolyte interface.....	3
1.2.2 Electrical Double Layer.....	4
1.2.3 Charge Transfer.....	4
1.2.4 Diffusion.....	5
1.3 Internal layers arrangement and battery formats.....	6
2. One-dimensional electrical model development.....	8
2.1 Experimental measurements.....	8
2.1.1 Battery under test.....	8
2.1.2 Microscopic analysis: materials characterization and internal layers thickness.....	9
2.1.3 Charging and discharging curves.....	10
2.1.4 Thermal characterization: thermal conductivities evaluation.....	16
2.2 Equivalent electric circuit modelling.....	19
2.2.1 Equivalent electric circuit models in literature: an overview.....	19
2.2.2 Weilin Luo's equivalent electric circuit model.....	20
2.2.3 Lumped parameters evaluation.....	23
2.2.4 Dependency of the lumped parameters on the electric current.....	25
2.2.5 First validation of the model.....	29
2.2.6 EIS measurements and upgrade of the model.....	30
2.2.7 Validation of the updated model: discharging curves fitting and energy check.....	35
3. FEM Model Development.....	37
3.1 Reasons.....	37
3.2 Software description.....	37
3.2.1 General Simulation Process.....	37
3.3 Custom model development.....	40
3.3.1 Geometry and mesh description.....	41
3.3.2 Employed physics models.....	43
3.3.3 Discretization strategy: equivalent circuit splitting.....	47

3.3.4	Modelling of an elementary cell	50
3.3.5	Modelling of a single-layer cell	54
3.3.6	Electrical behaviour validation of a single-layer cell.....	56
3.3.7	Modelling of the complete cell	60
3.3.8	Model validation: controlled temperature constant-e-current discharge.....	63
4.	Nail Penetration Test	68
4.1	Regulations and Motivations	68
4.2	Nail penetration tests description	69
4.2.1	Used nail	69
4.2.2	Test settings	70
4.2.3	Test results	72
4.3	Electro-thermal modelling of a nail-penetrated battery cell	74
4.3.1	Meshing of the components	74
4.3.2	Contacts definition and boundary conditions	75
5.	Simulation Results.....	77
5.1	Electric current	77
5.2	Electric Potential	81
5.3	Temperature	82
6.	Conclusions.....	86
	References.....	89

List of Figures

Figure 1.1 - Example of REDOX reaction in a Li-ion battery cell	1
Figure 1.2 - Intercalation and de-intercalation process of Li ⁺ in the electrodes (picture from the Web).....	2
Figure 1.3 - Electrochemical processes during discharge [11]	3
Figure 1.4 - Solid Electrolyte Interface [16].....	3
Figure 1.5 - Electric Double Layer (picture from the Web)	4
Figure 1.6 - Schematic view of the Li ⁺ charge transfer process during discharge [17]	5
Figure 1.7 - Scheme of the diffusion of redox species M through the porous electrode [14].....	5
Figure 1.8 - Different common form factors for lithium-ion cells [8]	6
Figure 1.9 - Internal layers structure of a pouch battery cell [18].....	7
Figure 2.1 - Disassembling of a battery module in order to get a single cell [18].....	8
Figure 2.2 - Sample generation and layers arrangement [18].....	9
Figure 2.3 - Thickness measurements of the anode, the cathode and the separator [18].....	10
Figure 2.4- EA-PSI 9080-340 3U technical data [19].....	11
Figure 2.5 - Front (top) and rear (bottom) views of the Power supply unit (left) and the electronic load (right) [19] [20]	12
Figure 2.6 - Sensors positioning.....	12
Figure 2.7 - CCCV charging method [21]	13
Figure 2.8 - Discharge curves at different C-rates	14
Figure 2.9 - Terminal voltage and temperature profile at 2C-rate	14
Figure 2.10 - Temperature controlled measurements: a) General assembly of a Peltier Plate [5]. b) Temperature controlled discharge curves. c) Temperature evolution at 0.5C (left) and 2C (right) discharge rate using Peltier Plate	15

Figure 2.11 - Comparison between total discharge capacities and temperature increase without (left) and with (right) Peltier Plate.....	16
Figure 2.12 - Description of the test settings: a) Longitudinal thermal conductivity measurements. b) Transversal thermal conductivity measurement	17
Figure 2.13 - Electrical analogy: a) Equations. b) Series configuration (transversal direction). c) Parallel configuration (longitudinal directions)	18
Figure 2.14 - Example of an equivalent electric circuit model with R-RC elements.....	20
Figure 2.15 - Open Circuit Voltage in function of the Discharged Capacity (Ah)	21
Figure 2.16 - Split of the internal total resistance	22
Figure 2.17 - Ohmic resistance evaluation	23
Figure 2.18 - Polarization Resistance evaluation	24
Figure 2.19 - Regression of [a1,a2,a3] parameters	24
Figure 2.20 - Discharging curves at different C-rates	25
Figure 2.21 - Polarization Resistance at different C-rates	26
Figure 2.22 – Example of computation of the polarization resistance value at different C-rate.....	27
Figure 2.23 - η parameter as function of electric current	28
Figure 2.24 - Comparison between measured and simulated discharge curves at different C-rates	29
Figure 2.25 - Mismatch between simulated and measured terminal voltages at high C-rates	29
Figure 2.26 – EIS measurements: a)schematic representation of the potential excitation and current response in the measurement setup (from literature); b)Resulting cell internal impedance at different SoC: Nyquist plot (b) and Bode diagram (c) [27]	31
Figure 2.27 - Parameters extraction from EIS measurements: a) equivalent electric circuit model; b) Regressed parameters values at 100% SoC; c) Fitting of the Bode Diagrams with a 5th-order equivalent circuit	31
Figure 2.28 - SoC dependency of the 5th-order equivalent electric circuit resistances	32
Figure 2.29 - Updated 1D-equivalent electric circuit model	33

Figure 2.30 - Comparison between measured and simulated discharge curves at different C-rates (new model).....	35
Figure 2.31 - 1D Simulation: (a) Equivalent electric circuit with constant load resistance; Total Heat Generated (b); Battery Average Temperature (c)	36
Figure 3.1 - Siemens STAR-CCM+: General Workflow	38
Figure 3.2 - Siemens STAR-CCM+ client workspace	40
Figure 3.3 - FEM modelling: main steps	41
Figure 3.4 - Detailed geometry of the battery cell	42
Figure 3.5 - Modelling Strategy (a) and modified 1D-equivalent circuit model (b).....	49
Figure 3.6 - Mapping of the equivalent electric circuit into a single elementary block	50
Figure 3.7 - STAR-CCM+ interface: a) Declaration of the Electric Potential boundary profile; b) Import of a file table; c) Introduction of a user function.....	52
Figure 3.8 - Laboratory Reference System.....	53
Figure 3.9 - Relationship between a single-layer cell and an elementary cell.....	54
Figure 3.10 - Review of the main steps for the set up of a simulation	56
Figure 3.11 - Simulated procedure: 0.5C discharge ($I = 20A$)	56
Figure 3.12 - Electric current density distribution in the (a) cathode current collector, (b) anode current collector, (c) cathode active material, (d) anode active material.....	57
Figure 3.13 - State of Charge distribution over the (a) Cathode and (b) Anode active material.....	58
Figure 3.14 - Electric Potential in (a) Anode current collector, (b) Cathode current collector; (c) Terminal voltage simulation and comparison with measurements	58
Figure 3.15 - Relaxation time simulation: a) imposed electric current step; b) terminal voltage recovering; c) State of charge before e-current step; d) State of charge at the end of the relaxation time	59
Figure 3.16 - Geometrical parameters of a complete cell.....	60
Figure 3.17 - Siemens STAR-CCM+ for macros recording and playing.....	61

Figure 3.18 - Contacts creation among tabs: contact surface highlighted in yellow	62
Figure 3.19 - Electric current density path in the active material (complete cell) during discharge.....	62
Figure 3.20 - Imposed thermal boundaries and current conditions.....	63
Figure 3.21 - Point probes position	64
Figure 3.22 - Electric current distribution in the (a) cathode and (b) anode current collectors	64
Figure 3.23 - Absolute state of charge distribution on the cathode active material at $t = 203s$	65
Figure 3.24 – Comparison between the time evolution of the absolute and relative state of charge.....	65
Figure 3.25 - Electric potential distribution in the (a) anode and (b) cathode current collectors; (c) Simulated terminal voltage.....	66
Figure 3.26 - Temperature distribution.....	67
Figure 3.27 - Simulated VS Measured temperatures.....	67
Figure 4.1 - Accidents related with lithium-ion battery failure, and correlated abuse conditions [1].....	68
Figure 4.2 - Used cross-section nail	70
Figure 4.3 - Positioning of the battery cell in the hydraulic press	71
Figure 4.4 - Thermocouples positioning.....	71
Figure 4.5 - Measured terminal voltage at the tabs	72
Figure 4.6 - Measured temperatures (100% state of charge).....	73
Figure 4.7 - Hexahedral mesh of the modelled components	74
Figure 4.8 - Conformal mesh between battery cell and nail	75
Figure 4.9 - Contact surface (highlighted in green) between battery cell and steel plate.....	76
Figure 5.1 - Estimation of the electric current through the nail	77
Figure 5.2 - Polarization Resistance (average)	78

Figure 5.3 - Electric current density in the current collectors at the (a) beginning and (b) after 76s from the complete penetration of the cell. (c) Electric current density distribution at the tabs	79
Figure 5.4 - Electric Potential Distribution on the Cathode Current Collectors	79
Figure 5.5 - Electric current density magnitude on the active material.....	80
Figure 5.6 – State of charge on the active material	80
Figure 5.7 - Comparison between simulated and measured terminal voltage	81
Figure 5.8 - Electric potential distribution in the current collectors	82
Figure 5.9 - temperature distribution on top side of the cell.....	83
Figure 5.10 - temperature distribution on bottom side of the cell.....	84
Figure 5.11 - Comparison between simulated and measured temperature at the tabs	85

List of Tables

Table 2.1 - Thicknesses of Single Layer Component Samples.....	10
Table 2.2 - Transversal and Longitudinal thermal conductivities of the cell (final values)	17
Table 2.3 – Thermal conductivity values of the internal battery materials	18
Table 2.4 - Estimated parameters values	25
Table 2.5 - Order of magnitude of the regressed parameters.....	33
Table 2.6 - SoC-invariant parameter values: old model VS new model	34
Table 3.1 - Geometrical characterization of the constitutive layers.....	42
Table 3.2 - materials physical properties	43
Table 3.3 -Selected models for anode/cathode active material and current collectors	44
Table 4.1 - Main features of the used nail	70
Table 4.2 - Nail material properties.....	70
Table 4.3 - Maximum temperatures (in °C) observed for each test at 100% SoC.....	74

Abstract

The increase of CO₂ emissions and the threat of global warming is leading to find technological solutions to reduce the greenhouse gases. Since the usage of fossil fuels for mobility produces a significant slice of CO₂ emissions, the electric-mobility represents an alternative solution with lower CO₂ impact. However, electric vehicles must guarantee safety requirements in order to make the public opinion feel confident towards this new technology. Consequently, compulsory tests defined by international standards (GTR20) must be performed on the EVs (Electrical Vehicles) components, before launching them on the market. Therefore, since performing tests is time and money consuming, it is beneficial to develop simulation models - based on the evaluation of some specified parameters - able to predict if a newly proposed design can be either accepted or rejected. This is called simulation-design loop and its target is the improvement of performances (ex. driving range) withstanding the safety requirements. With simulation models, the number of needed tests can be sensibly reduced having a beneficial impact on costs and time.

In this work an empirical multi-physics numerical model has been developed, with the purpose to predict the voltage distribution, the electric current and the temperature of a Li-ion battery in case of electrical short circuit or nail penetration. Simulations have been validated with experimental tests. The battery under analysis - obtained by disassembling the battery pack of a commercial vehicle - it is a laminate pouch-type cell, composed by Graphite as anode material, a spinel of NMC and LMO as Cathode material. The cell showed a rated capacity of 41 Ah and a nominal voltage of 3.7 V. The correct evaluation of these parameters allows to tell in advance if the tested cell will incur in a thermal runaway. The obtained model can be employed for a preliminary study of the thermal propagation on the newly designed cells.

Introduction

In the last years, the concept of Electric-mobility is fast spreading all over the world. Indeed, owing to the advent of clean and high-efficiency technologies able to convert nuclear, wind and solar energy into electric energy, EVs represent the most viable solution able to face environmental problems besides the energy crisis [1]. Researches in this field, mainly involving the development of suitable storage and propulsion systems [2], interest also governments, which are asked to meet increasingly stringent requirements about emissions [3]. Obviously, the spread of the EVs on the market most depends on the public opinion, which may be undermined if serious accidents occur. Thus, in order to guarantee safety, compulsory tests standard must be successfully passed. Those tests are collected in the United Nations Global Technical Regulation (UN GTR) No. 20 (Electric Vehicle Safety), which main purpose is to address the safety of EVs, while in use and after a crash event [4]. In particular, it includes the potential hazards associated with Rechargeable Electrical Energy Storage Systems (REESS) containing flammable electrolyte, as lithium-ion batteries, widely used in this field due to their high energy density and extended cycle life [1].

On the other hand, the searching for the fulfilment of safety requirements lowers the performances of the EVs, such as the maximum allowed driving range, which is strictly connected with the total volumetric energy stored by the system [5]. Such kind of limitation, together with the lack of suitable infrastructures as the charging stations, make EVs still not competitive enough with fossil fuels based vehicles. As consequence, continuous improvements in the design of battery packs is required in order to achieve the best compromise between safety and performance.

In this perspective, it is easy to understand the crucial importance, in terms of costs and time saving, of developing suitable models able to capture the behavioural aspects of the implemented batteries. Particularly, it has been seen that the main external features of a battery during operation (with a focus on Lithium-ion batteries) can be easily described, from an electric point of view, through an equivalent electric circuit model, essentially made up of a voltage source and some passive components like resistances and capacitances [6]. Among many purposes that this kind of modelling can serve, such electrical abstraction, joined with a thermal characterization, can be exploited in order to set up a multi-physics electro-thermal FEM model of the battery providing a prediction of the heat generated and of the temperature

distribution over its volume under particular load conditions. This kind of model finds a practical application in the thermal propagation test, aimed at analysing the hazards on the occupants of the vehicle when a thermal runaway due to an internal short circuit (provoked, for example, by a nail penetration) occurs [4].

From a design perspective, the electro-thermal model can be used in order to test the newly designed battery packs firstly in simulation (simulation design-loop). Then in case of positive results, the real test will be performed. Otherwise, adjustments in the design are needed.

This work takes part to the “SafeBattery” research project, funded by FFG and seven industrial partners (Audi, AVL, Bosch, Daimler, Kreisler, Porsche, SFL), with the main objective of understanding which are the hazards of Li-ion batteries under various mechanical load conditions. In particular, the Thesis focuses on the development of an electro-thermal FEM model for a Li-ion pouch cell used in a commercial EV, with the purpose of predicting the voltage distribution, the electric current and the temperature of a Li-ion battery in case of electrical short circuit or nail penetration. This evaluation is useful in order to predict if the cell will incur into Thermal Runaway, according to the conditions prescribed by the Global Technical Regulation (GTR20) on Electric Vehicle Safety [4]. The modelling has been carried into Siemens STAR-CCM+.

The presented work has been organized as follows: the first chapter resumes the working principle of a Lithium-Ion battery cell and the main electrochemical processes that contribute to the determination of its internal impedance. An overview of the internal layer arrangement and the most employed battery-cell formats is also provided. In the first part of the second chapter measurement procedures and results used to characterize the tested battery cell from an electro-thermal point of view are briefly shown. In the second part, the main steps for the derivation of a 1D-equivalent electric circuit model have been documented. The third chapter deals with the development of the FEM multi-physics model into STAR-CCM+ environment, with a complete description of the discretization strategy and of the main modelling steps. The documentation of a first validating simulation has been also included. In the fourth chapter, a resume of the performed nail penetration tests is provided, with particular focus on the measurements set-up and the sensors positioning. In the last part, a description of the settings for the FEM simulation with the nail is depicted. Finally, in the fifth chapter, the main results are shown and a comparison with real measurements is performed.

CHAPTER 1

1. Literature review on Lithium-ion batteries

1.1 Working principle of a lithium-ion cell (chemical aspects)

Lithium ion batteries comprise a family of battery chemistries that employs various combination of anode and cathode materials. Each combination shows different advantages and disadvantages in terms of safety, performance and costs. In automotive applications, the most used technologies are lithium-nickel-cobalt-aluminium (NCA), lithium-nickel-manganese-cobalt (NMC), lithium-manganese spinel (LMO), lithium titanate (LTO), and lithium-iron phosphate (LFP) [7].

No matter of the used materials, the main aspects that characterize the working principle of Li-ion batteries are almost the same. Generally speaking, they are considered secondary battery systems, since they can be charged and discharged many times. From a chemical point of view, this means that the electrochemical reactions that take place at the electrodes are reversible. In other words the original chemical compounds can be reconstituted by the injection of energy into the cell, which causes electrons and positive ions (Li^+) to move from the cathode (positive electrode) back to the anode (negative electrode), storing charges [8]. Due to the reversibility of the process, lithium-ions cells are also defined rocking chair cells.

The main purpose of the electrochemical reactions is to sustain a steady state current flow into the galvanic circuit and in particular at the electrodes/electrolyte interface. Indeed, due to their different nature, two different carriers, which are electrons and ions, characterizes the electrodes and the electrolyte. Thus, particles at the interfaces cannot be exchanged directly, but an oxidation-reduction reaction is needed [9].



Full Cell Reaction:

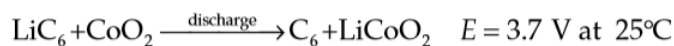


Figure 1.1 - Example of REDOX reaction in a Li-ion battery cell

Differently from a common redox chemical reaction, in Li-ion batteries an “insertion-electrode reaction” happens: lithium does not react directly with the electrode materials. Instead it is either absorbed from the electrolyte and inserted into the structure of the electrode material (process known as intercalation) or expelled from the electrode material into the electrolyte (process known as de-intercalation), depending on the direction of the current flow. During this process, the crystal structure of the electrodes is not changed from a chemical point of view, but can be subject to structural changes when the lithium is inserted or removed.

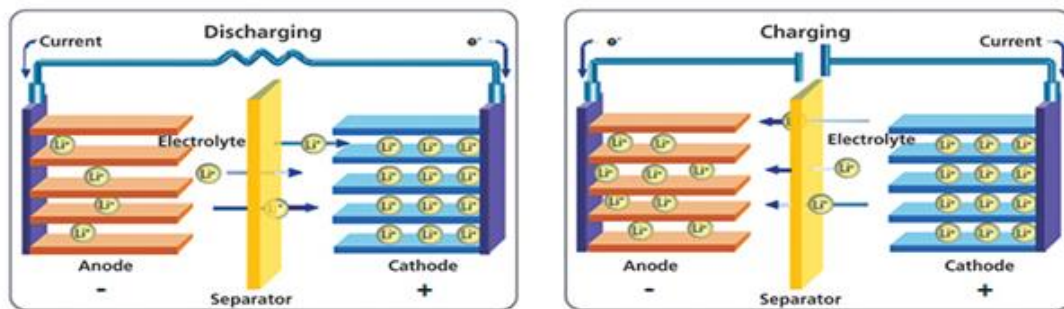


Figure 1.2 - Intercalation and de-intercalation process of Li^+ in the electrodes (picture from the Web)

1.2 Main electrochemical processes

Inside a Li-ion battery cell, a number of electrochemical processes happens, which contribute to the definition of its impedance. Their knowledge is useful to model properly the passive electrical components that build up the equivalent electric circuit, as will be shown in the following chapters. [8] [10].

At a very high level, the discharging process can be described as follows: at the anode/electrolyte interface, lithium is oxidised to form Li^+ ions. Thus, the Li^+ ions migrate through the electrolyte due to potential gradient. Then reduction takes place at the interface between electrolyte and cathode. Finally, atoms diffuse into the positive electrode [11]. A similar description can be provided for the charging process.

During charge/discharge, every phenomenon related to a mass transfer mechanism, can be depicted as a diffusive process. Particularly, diffusion occur both in the electrolyte and in the electrodes (the latter is known as solid state diffusion) [10].

On the other hand, phenomena related to chemical reactions at the interfaces between electrodes and electrolyte are described as charge transfer processes [12].

Other electrochemical aspects that it is worth taking into account for the description of the overall impedance of the cell are the Solid Electrolyte Interface and the Electric Double Layer [8] [9].

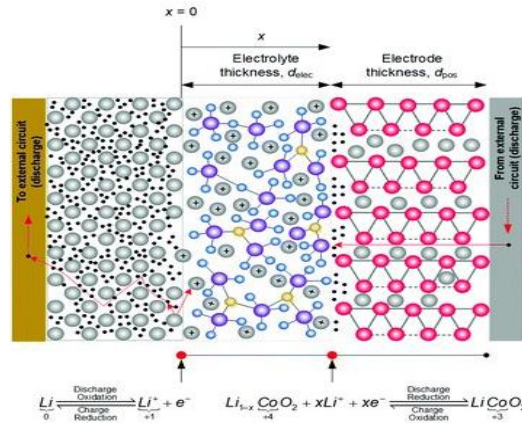


Figure 1.3 - Electrochemical processes during discharge [11]

1.2.1 Solid Electrolyte interface

The Solid Electrolyte Interface (also known as SEI Layer) is a passivating film that typically develops on the surface of the anode. Its development is caused by the violent reaction of the organic solvent making up the electrolyte with the graphitic negative electrode. Such a reaction causes an irreversible lithium consumption and, consequently, a reduction of the energy that the battery can deliver [8] [13].

The SEI layer is formed mainly during the first charging cycle (formation process). Then it keeps growing much more slowly and prevents the anode material from further corrosion due to uncontrolled reactions with the electrolyte solution [8].

Even if the real nature of the SEI layer is not still known completely, generally it is constituted of both organic and inorganic compounds that are electronically non-conducting and lithium-ion conducting [8]. The status of the SEI film contributes to the impedance of the overall battery, since lithium-ions migrate through it [14] [15].

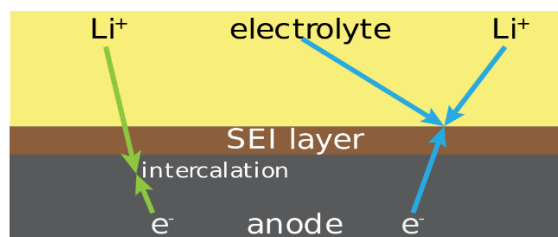


Figure 1.4 - Solid Electrolyte Interface [16]

1.2.2 Electrical Double Layer

The electrical double layer (EDL) is a structure that appears on the phase boundary, so at the interface between the electrode (solid) and the electrolyte (liquid). The name “Double Layer” refers to two parallel layers of charges that develops at the interface. Physically speaking, the EDL forms due to the potential difference existing between electrode and electrolyte, depending on the excess of charges accidentally accumulated on the boundary surface. Due to chemical interactions, a unidirectional chemical force will result, that makes the charges moving, forming the first layer. This excess of charges causes a development of electrical forces (Coulomb forces) that attract charges of opposite sign, so that the second layer appears [9].

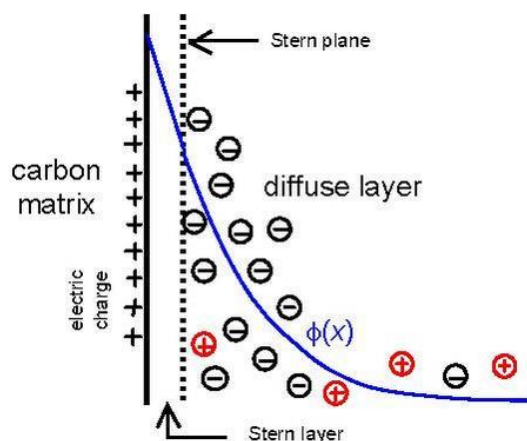


Figure 1.5 - Electric Double Layer (picture from the Web)

From a modelling point of view, a very high capacitance can be associated to the electric double layer. Indeed, it is made of two parallel layers of charges with opposite sign, each on the surface of one of the contacting phases, separated by a very thin layer of solvent molecules [9].

1.2.3 Charge Transfer

As already said, a battery cell is a galvanic cell, so the carriers belong to two different species: ions and electrons. As consequence, a sink/source for arriving/departing particles is needed in order to sustain a steady current flow through the cell. This movement of charges at the electrode/electrolyte interface is known as charge transfer and it is sustained by the chemical reactions [9]. In particular, referring to a lithium-ion battery, the Li^+ charge transfer process is

defined as the process of turning a solvated Li^+ in the electrolyte into Li in the electrode, by accepting an electron from the electrode [17].

An impedance can be associated to the charge transfer kinetics, which mainly depend on the activation energy of the reaction and on the availability and mobility of the ions.

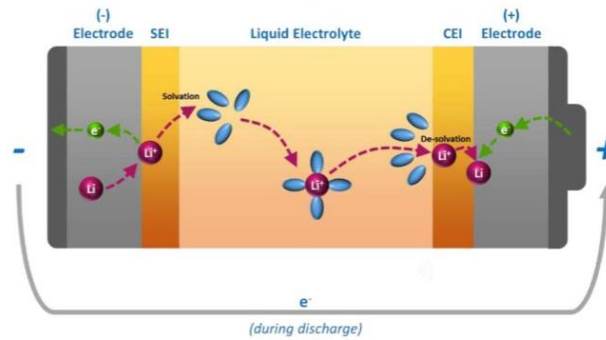


Figure 1.6 - Schematic view of the Li^+ charge transfer process during discharge [17]

1.2.4 Diffusion

Diffusive processes take place both in the electrolyte and in the electrodes and concern transfer of mass.

While the Li -ions migration in the electrolyte is very fast and driven by a potential gradient [10] [11], the solid state diffusion, taking place in the electrodes, is caused by a gradient in composition rather than an electric field. The associated solid-state diffusion impedance originates from the concentration gradient of Li^+ through the porous electrode filled with electrolyte and it is larger at lower frequencies (so its contribution become more evident in longer times), where there is a deeper diffusion of Li^+ into the electrodes [14].

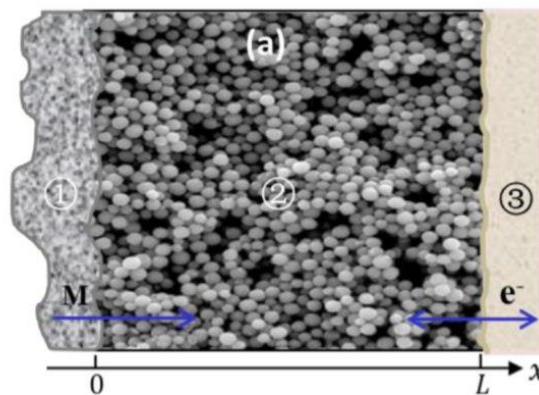


Figure 1.7 - Scheme of the diffusion of redox species M through the porous electrode [14]

1.3 Internal layers arrangement and battery formats

Independently on the shape that the battery has, the basic elements that build up a cell are always the same. These are:

- Negative Electrode (anode): made of a carbonaceous material, usually Graphite.
- Positive Electrode (cathode): made of more complex materials, as NMC. These materials must be intercalation compounds, allowing the lithium movement through their crystal structure.
- Electrolyte: made of non-aqueous organic solvents plus a lithium salt. Water cannot be used as solvent, since lithium reacts violently with it. Only the salt participates in the chemical process of the cell. Thus, the solvent is typically ignored in the description of the electrolyte.
- Separator: permeable membrane with holes large enough to let the movement of lithium ions through it, but small enough to prevent any contact between negative and positive electrode particles. It is also an electronic insulator.
- Current collectors: metallic foils that coat the active electrode materials and that are in charge of conducting current into and out of the cell. Copper is used as anode current collector, while aluminium is employed for the cathode current collector [8].

Cells contain more negative and positive electrodes, which are electrically connected inside the cell, so that they form a single logical negative and positive electrode.

The elements that make up a battery cell can be arranged in different ways, depending on the chosen form factor. Mainly, it is possible to distinguish three types of cells:

- Cylindrical cells
- Prismatic cells
- Pouch cells

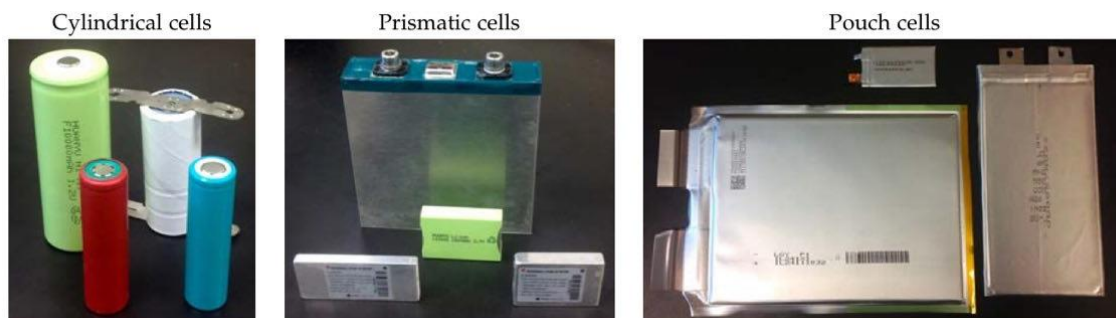


Figure 1.8 - Different common form factors for lithium-ion cells [8]

For high-capacity battery applications, like the ones in the automotive field, prismatic and pouch cells are usually preferred, in order to optimize the use of the volume in the battery packs [8]. Anyway, cylindrical cells are still used since they are cheaper than the other formats.

In this work, pouch cells are considered. They are assembled by stamping the electrode plates out of the reels of electrode-coated foil. Negative and positive electrode plates are alternately stacked, with separator material between them. Then, in order to obtain a single logic negative (positive) electrode, all the negative (positive) electrode tabs are welded in parallel and to the cell's negative (positive) terminal [8].

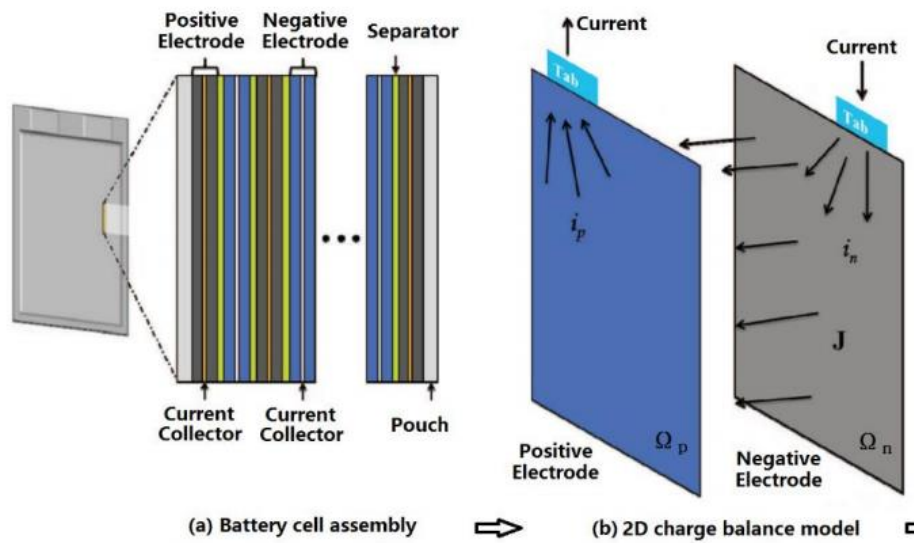


Figure 1.9 - Internal layers structure of a pouch battery cell [18]

CHAPTER 2

2. One-dimensional electrical model development

2.1 Experimental measurements

The set-up of an empiric model able to fit faithfully the behaviour of the battery cell under test, requires some input data. Firstly, a geometrical characterization of the pouch cell in terms of dimensions and internal layers structure is needed in order to build a correct CAD model to be used in simulation. Secondly, the understanding of the electrical properties is required, so that a correct description of the overall battery voltage response to different current stimuli can be provided through a suitable one-dimensional equivalent electric circuit model. Finally, for the building of the complete three dimensional electro-thermal FEM model, also the thermal characteristics of the constitutive layers, as the thermal conductivity and the specific heat, must be evaluated.

2.1.1 Battery under test

The battery under analysis is a laminate pouch-type cell with a rated capacity of 41Ah and cut-off voltage limits of 2.5V and 4.2V. The cell is extracted from one of the 24 modules making up the 2016 Nissan Leaf battery pack.



Figure 2.1 - Disassembling of a battery module in order to get a single cell [18]

2.1.2 Microscopic analysis: materials characterization and internal layers thickness

In order to get information about the material composition, the thickness of the layers and their arrangement in a single battery cell, a microscopic analysis of suitably prepared samples is required.

The way in which electrode layers are stacked was investigated by cutting the pouch cell in large areas (i.e. 50mm x 50mm). Then, the obtained samples were embedded in epoxy resin, polished with grinding papers and finally analysed at the scanning electron microscope (SEM). Results show that the battery under test is made of 22 anode layers, 21 cathode layers and 44 separator foils. On both terminal sides of the stack, anode layers are present [18].

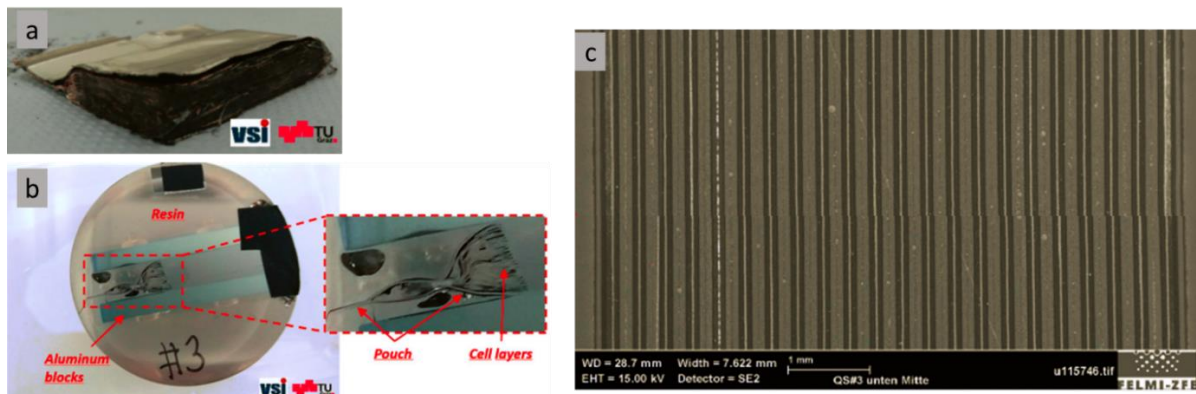


Figure 2.2 - Sample generation and layers arrangement [18]

On the other hand, to explore the thickness of the layers and their material composition, smaller samples (5mm x 5 mm) from the battery anode, cathode and separator were cut. Thicknesses were evaluated with the SEM, while in order to investigate the chemical composition of each compound an Edex Super Octane energy-dispersive X-ray spectroscopy device was used. Such tool is able to provide information about the chemistry of the investigated sample by evaluating the energies associated to the released X-ray radiations when the material under exam is hit with high-energy electrons [18].

From this analysis it has been found that the anode active material is made of graphite, while the cathode is a blend of NMC and LMO chemistries. Instead, the separator is made of fibers of PP/PE materials, aligned in a direction perpendicular to the battery tabs.

Concerning the thicknesses of the involved layers, results are reported in Table 2.1. The tolerance of these measures is about 5 μ m and depends on the active material grain radius [5].

Component	Thickness (μm)	Component	Thickness (μm)	Component	Thickness (μm)
Anode	140	Cathode	170	Separator	20
Anode CC	10	Cathode CC	20	Pouch	190
Anode AM	65	Cathode AM	75		

Table 2.1 - Thicknesses of Single Layer Component Samples

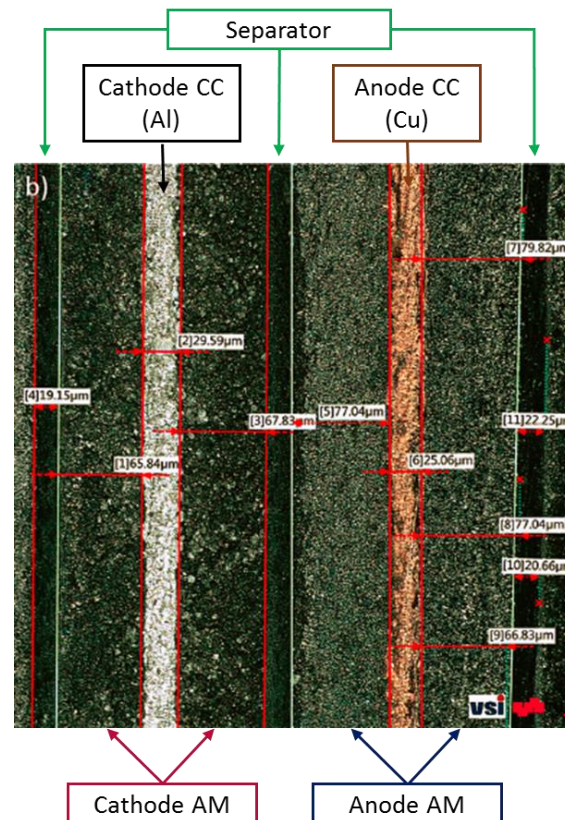


Figure 2.3 - Thickness measurements of the anode, the cathode and the separator [18]

2.1.3 Charging and discharging curves

Constant-current charging and discharging curves are useful to get information about the electrical behavior of the battery cell and on those features, which can be then exploited for the development of an equivalent electric circuit model. In particular, in order to guarantee a proper characterization, tests must be carried out in a wide range of electric currents, from nearly zero values until some hundreds of amperes.

These measurements are carried out making use of a battery tester. Such tool is assembled with a number of modules, which allow the charge and discharge of a cell and the

monitor of the output quantities of interest, as the sensed voltage, the current and the temperature.

Charging procedures are performed through the EA-PSI 9080-340 3U programmable DC power supply, able to provide DC output voltages between 0...80V, output current between 0...340A and output power between 0...10000W. The module allows a remote sensing of the load: in other words, the sensing input can be connected directly to the load. In this way, the power supply can adjust the output voltage automatically, so that the voltage drops along the power cables can be compensated and the accurate required voltage at the load is guaranteed. Test procedures to be applied at the output voltage or the output current can be configured either using the touch panel in front of the device or by remote control via a digital interface [19].

Technical Data	PSI 9080-340 3U
Rated voltage & range	0...80 V
- Ripple ⁽¹⁾	<320 mV _{PP} <25 mV _{RMS}
- Sensing compensation	~2 V
Insulation	
- Negative DC pole <-> PE	±400 V DC
- Positive DC pole <-> PE	±400 V DC
Rated current & range	0...340 A
- Ripple ⁽¹⁾	<160 mA _{RMS}
Rated power & range	0...10000 W
Efficiency	~93%
Programming resolution U	≤4 mV
Programming resolution I	≤14 mA
Weight ⁽²⁾	~24 kg
Ordering number EU model ⁽³⁾	06230357
Ordering number US model ⁽³⁾	06238357

Figure 2.4- EA-PSI 9080-340 3U technical data [19]

On the other hand, discharge processes are executed with the EA-EL 9080-340 B electronic DC load. It supports the four common regulation modes, which are constant voltage (CV), constant current (CC), constant power (CP) and constant resistance (CR). The available voltage range is 0...80V DC, while input currents can reach values up to 340A. The range for the load resistance is 0.023...7.5 Ω. This module offers also a battery test mode, suitable for testing constant current or constant resistance discharging on all kind of batteries [20].

Both the mentioned modules are provided with a graphic display, which allow reading the actual values of voltage, current and power. Furthermore, it is possible to set overvoltage

(OVP), overcurrent (OCP) and overpower (OPP) protection thresholds, above which the DC output is immediately shut off. There is also an over-temperature protection, which shuts off the DC output if the device overheats.

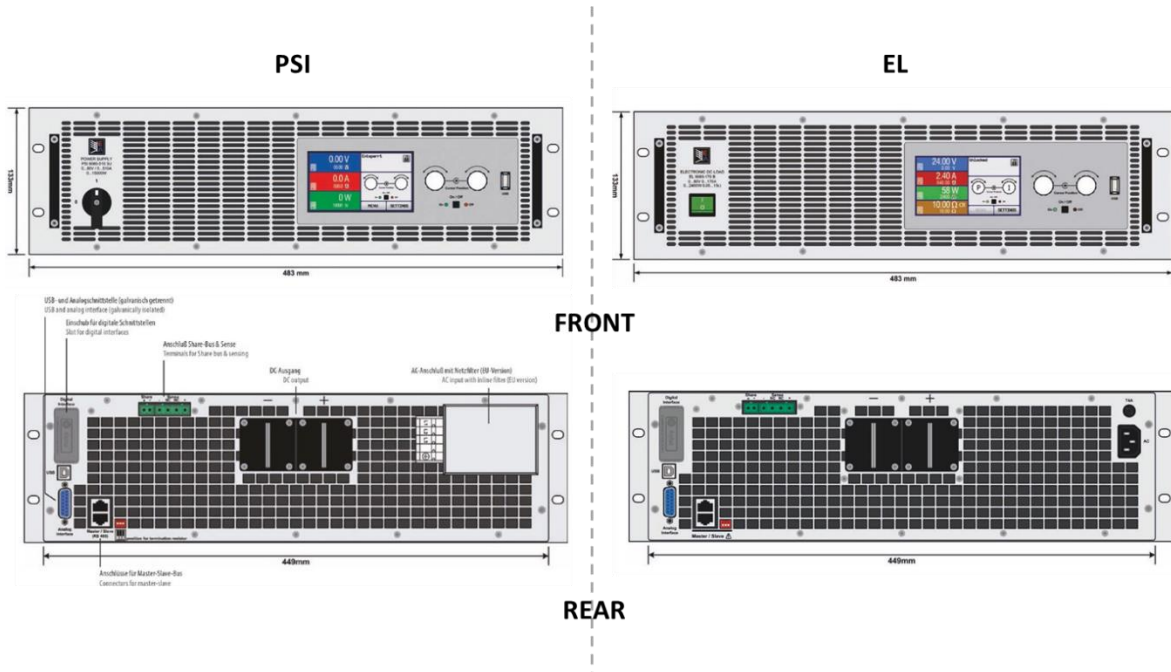


Figure 2.5 - Front (top) and rear (bottom) views of the Power supply unit (left) and the electronic load (right) [19] [20]

During the tests, the temperature on six points of the stack and on the two tabs has been monitored using K-type thermocouples. An additional thermocouple was employed to measure the ambient temperature.

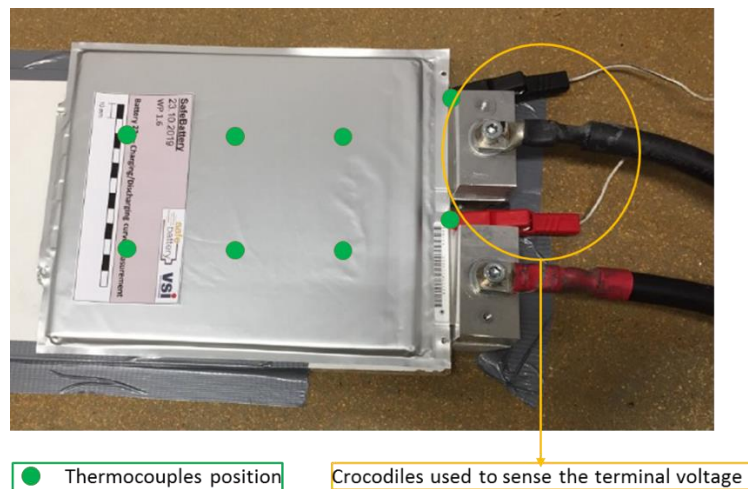


Figure 2.6 - Sensors positioning

The voltage at the terminals has been sensed by putting two crocodiles directly in contact with the anode and cathode tabs, so that the differential voltage between them can be evaluated.

Before applying a discharge procedure, the tested battery cell must be fully charged through the CCCV (constant current-constant voltage) method. As first step, the battery is charged at a fixed C-rate (usually 1C-rate, that, in case of the considered cell corresponds to 40A). The constant-current charge is enabled till the upper cut-off voltage limit is reached (4.2V). At this point, the battery cell continues to be charged in constant-voltage mode: as the name suggest, the voltage is kept constant to its maximum value of 4.2V, while the current decays exponentially till a certain C-rate, usually C/40 [8]. After a relaxation time of 10-15 min, the battery is ready to be discharged at the desired C-rate. The discharge is stopped when the lower cut-off voltage (2.5V) is reached. A similar way to proceed must be repeated for a charging tests.

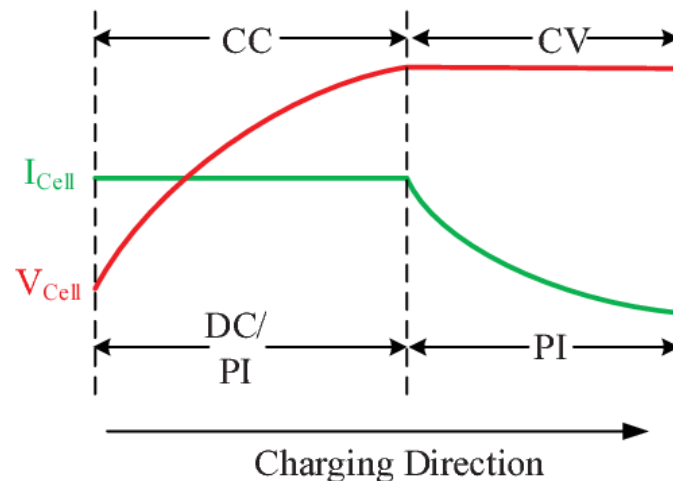


Figure 2.7 - CCCV charging method [21]

The acquisition frequency of the monitored signals (voltages, currents and temperatures) has been fixed at 2kHz. This value has been chosen to properly describe also the high frequency phenomena taking place inside the battery. From the study of the literature, the fastest dynamics have a characteristic frequency in the range of few kHz and are related to the ohmic resistance of the electrolyte and the electronic contacts [22].

The first set of measurements has been carried out without any control on the temperature. In other words, the temperature of the battery cell was free to evolve depending on the combined effect of the heat generated during the charge/discharge cycles and of the ambient temperature. Due to safety issues, measurements have been carried out in an open

environment, with ambient temperature ranging between -5°C and 5°C . In order limit high thermal excursions, the battery cell was put in a polystyrene box.

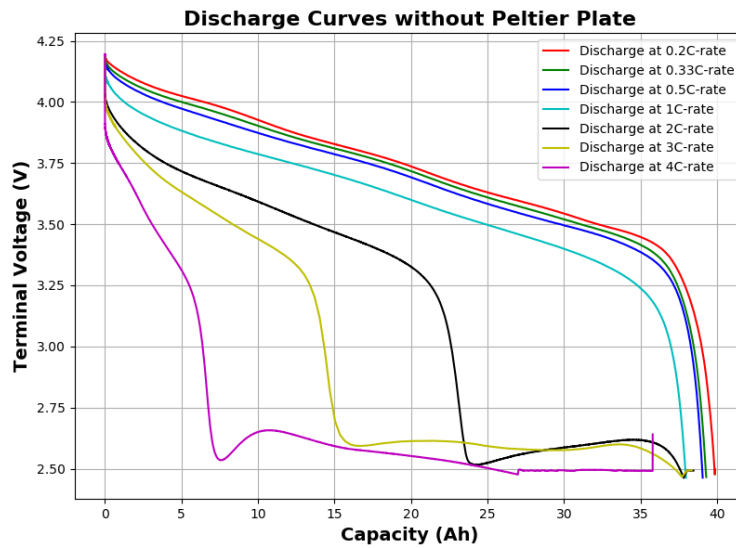


Figure 2.8 - Discharge curves at different C-rates

Under these settings, at high C-rates, corresponding to discharging currents in the range of [80A, 160A], a deep loss in the total capacity [Ah] of the cell occurred, besides a strange behaviour at the end of the discharge. Particularly, the latter seemed to be strictly related to the trend of the temperature measured on top of the cell stack, which showed a change in the slope around the same area.

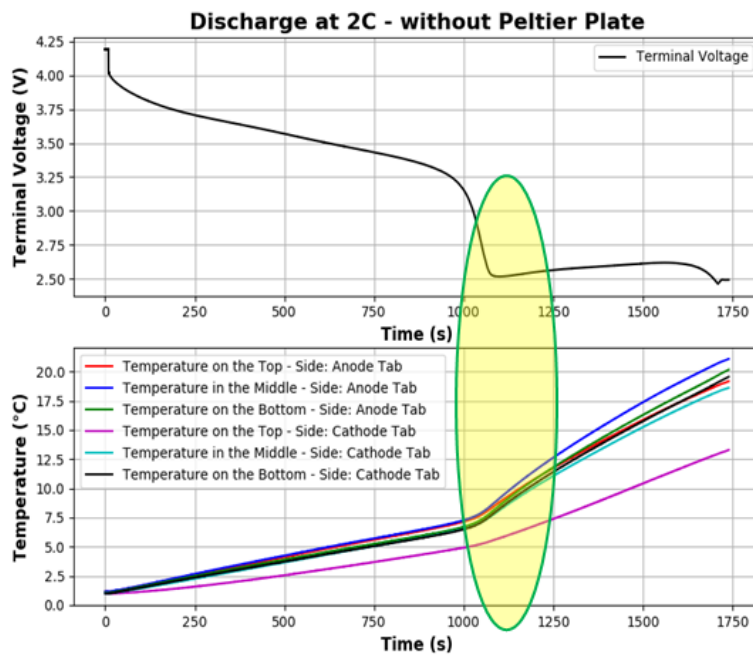


Figure 2.9 - Terminal voltage and temperature profile at 2C-rate

As consequence, to improve the quality of the measurements, discharge cycles were repeated, trying to keep the battery cell at a fixed temperature, around 20°C. In order to reach this purpose, a temperature-guarded plate, known as Peltier Plate, has been employed. This consists of an Aluminium plate, employed as a thermal mass and of a number of Peltier elements homogeneously distributed on it, used to regulate the Aluminium plate temperature [5]. By putting the battery directly on the Aluminium plate, it is possible to set the temperature of the contact surface to the wanted value. Obviously, since the cell has a thickness of 8mm, a gradient over it is established and consequently the temperature on the opposite side, where thermocouples are placed, is few degrees lower. In order to limit the effect of the ambient temperature, the whole system has been covered with polystyrene.

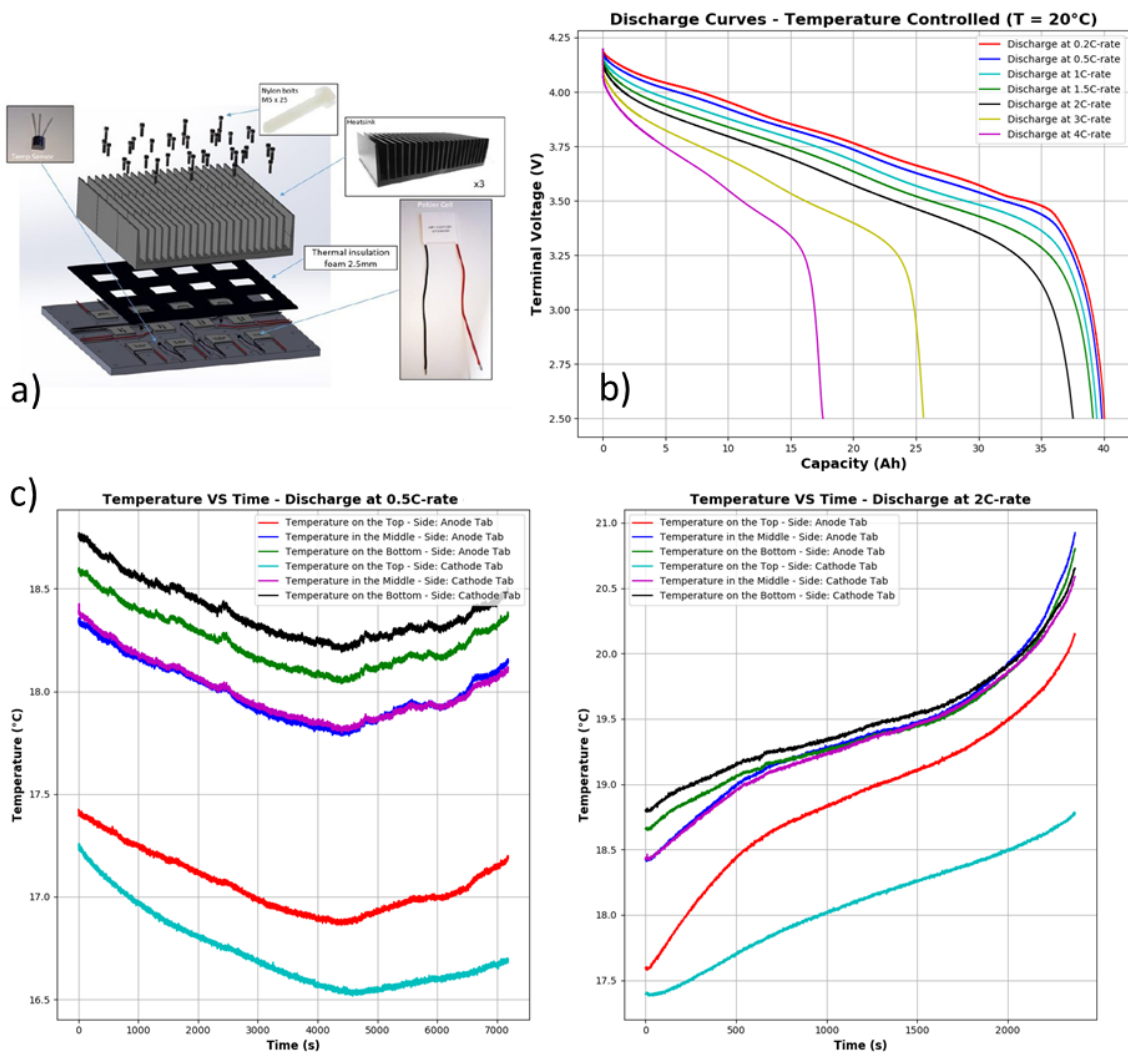


Figure 2.10 - Temperature controlled measurements: a) General assembly of a Peltier Plate [5]. b) Temperature controlled discharge curves. c) Temperature evolution at 0.5C (left) and 2C (right) discharge rate using Peltier Plate

Figure 2.10-b shows that no strange behaviour in the terminal voltage profile occur if the temperature is kept around 20°C. Higher total discharge capacities are reached even at high C-rates. Figure 2.10-c provides two examples of the temperature evolution on top of the cell-stack, when the Peltier Plate is used: at low discharge rates (20A), the temperature remains almost constant during the entire procedure. At higher currents (80A), there is an increase of only 4°C, against the 20°C obtained without Peltier plate at the same discharge current.

C-rate	Capacity	Min T*	Max T*	ΔT^*
0.2C	39.82 Ah	0.18°C	12.45°C	12.27°C
0.5C	39.26 Ah	4.87°C	7.16°C	2.29°C
1C	39 Ah	3.21°C	7.98°C	4.77°C
2C	~24.5 Ah	1.15°C	21.1°C	19.95°C
3C	~24 Ah	5.91°C	32.67°C	26.76°C
4C	~8 Ah	1.33°C	33.5°C	32.17°C

Without Peltier Plate – Ambient Temperature range [0,6] ° C

C-rate	Capacity	Min T*	Max T*	ΔT^*
0.2C	40.05 Ah	17.61°C	18.18°C	0.57°C
0.5C	39.86 Ah	17.78°C	18.36°C	0.58°C
1C	39.45 Ah	17.31°C	19.42°C	2.11°C
2C	37.54 Ah	17.63°C	21.66°C	4.03°C
3C	25.6 Ah	18.49°C	24.78°C	6.29°C
4C	17.5 Ah	18.06°C	25.57°C	7.51°C

With Peltier Plate – Temperature ~20° C

Figure 2.11 - Comparison between total discharge capacities and temperature increase without (left) and with (right) Peltier Plate

2.1.4 Thermal characterization: thermal conductivities evaluation

For a proper simulation of the investigated battery cell from a thermal point of view, a description in terms of thermal conductivity and specific heat of the composing layers is also needed. Properties of the current collectors are supposed to be well known, since they are simply made by copper and aluminum. Instead, the thermal characterization of the active material (anode, cathode and separator) requires a deeper analysis. In this work, data coming from previous studies [5] have been used and are here briefly illustrated.

As first, the thermal conductivity of the overall cell was measured in the three spatial directions, by making use of Peltier cooling modules (Figure 2.10-a) and heater mats. In particular, as described in [5], the used equipment has been designed to force the temperature gradient along the direction of the thermal conductivity measurement, while the thermal insulation has been guaranteed in the other two directions. During the tests, the heat flux and the temperature at the two opposite sides of the battery cell (along the considered direction) have been monitored through a set of heat flux sensors. Once the steady state condition were reached, the thermal conductivity in the i -th direction has been computed as:

$$\sigma_{\text{thermal}} = \frac{\text{Surface Heat Flux} \left(\frac{W}{m^2} \right) \cdot \text{Thickness (m)}}{\Delta \text{Temperature (K)}} \quad (2.1)$$

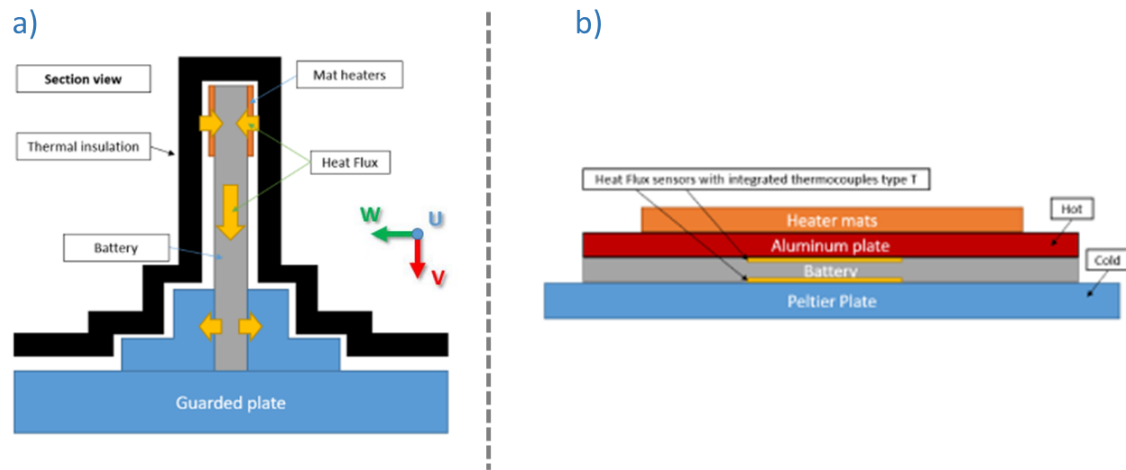


Figure 2.12 - Description of the test settings: a) Longitudinal thermal conductivity measurements. b) Transversal thermal conductivity measurement

Table 2.2 lists the computed thermal conductivities of the tested battery cell in the three directions. In particular, the thermal conductivity along the parallel directions “u” and “v” is almost the same, while the one in the “w” direction is about 35 times lower. This means that, on a thermal point of view, the cell presents an orthotropic behaviour.

Direction	Thermal Conductivity (W/mK)
Transversal (w)	0.77
Longitudinal (u)	25.74
Longitudinal (v)	25.55

Table 2.2 - Transversal and Longitudinal thermal conductivities of the cell (final values)

For 3D numerical modelling purposes, it can be useful to compute the thermal conductivity of the active material, knowing the thermal conductivity of the overall cell and the ones of the aluminum and copper foils (from literature). Such objective can be reached by setting up an equivalent electric problem. For a sake of simplicity, the layers of the same type were grouped into a single equivalent layer with a suitable thickness.

Considering the transversal direction, the overall thermal resistance of the cell (and consequently its thermal conductivity) is supposed to be obtained from the series connection of

the thermal resistances of each single layer. On the other way around, along the longitudinal directions, the equivalent thermal resistance is given by the parallel of the single-type-layer resistances.

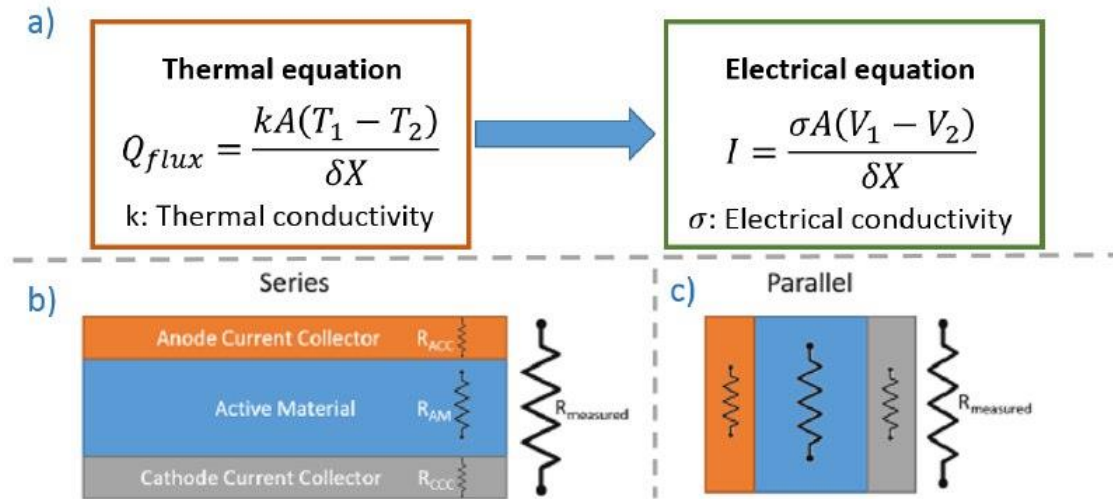


Figure 2.13 - Electrical analogy: a) Equations. b) Series configuration (transversal direction). c) Parallel configuration (longitudinal directions)

Through such analogy, it has been possible to compute the thermal conductance of the active material and finally its thermal conductivity, by exploiting the geometrical description of the layers in terms of thickness. Results coming from the solution of the problem in the three spatial directions were comparable, indicating that the active material thermal conductivity shows an isotropic behavior.

Component	Material	Thermal Conductivity	
		Transversal	Longitudinal
Anode CC	Copper	400 (literature)	
Active Material	Graphite	1.2 (computed)	1.2 (computed)
Anode	PP/PE		
Separator	NMC		
Cathode			
Cathode CC	Aluminum	240 (literature)	

Table 2.3 – Thermal conductivity values of the internal battery materials

2.2 Equivalent electric circuit modelling

Equivalent electric circuit models are aimed at describing the electrical aspects of a battery cell in terms of voltage response and heat generated when different loads are applied. This kind of empiric models provides a behavioural description of the battery, since the employed circuit elements simply capture the dynamic of the internal electrochemical processes, but they do not give any information about the construction of the cell [8].

The modelling through an equivalent circuit offers a trade-off between physical interpretability and computational complexity in the determination of the lumped parameters values (i.e. values of resistors, capacitors and voltage sources). Thus, they represent a valid alternative to the physics-based models, which instead involve a huge number of parameters [22].

As first step, a unique equivalent electric circuit model characterizing the behaviour of whole battery cell will be derived. Then, for the implementation of the more complex electro-thermal model, the lumped parameters values will be suitably scaled, so that each element coming from the FEM discretization can be also described electrically by an equivalent electric circuit.

2.2.1 Equivalent electric circuit models in literature: an overview

Researchers have developed different Li-ion battery equivalent-circuit models in order to meet the demands for simulative technologies [6]. No matter of their arrangement, the electric components that make up the circuit are almost the same. Particularly, as the most fundamental observed behaviour of a battery cell is that it can deliver a voltage at its terminals, at least one voltage source must be present in the network. Such component models the voltage provided by the cell when it is in open circuit condition, so when it is unloaded and in a complete equilibrium state. Depending on the level of charge of the battery, which can be quantified through the State of Charge (SoC) state-variable, the delivered open circuit voltage is different. Thus, most of the models consider a SoC-controlled voltage generator, denoted as $OCV(SoC)$ [8].

On the other hand, the main electrochemical processes happening inside the battery, as the diffusion, are modelled through an impedance. This is generally called polarization impedance and tries to explain the mismatch existing between the open circuit voltage and the actual terminal voltage provided by the battery, when current flows inside the cell. Usually, the

polarization impedance is modelled through resistive components, especially when constant charging and discharging conditions should be depicted. On the other side, if a proper description of the transients has to be guaranteed, elements like capacitors and inductors must be also included in the network. Like in the case of the open circuit voltage, the values assumed by the polarization impedance are not constant but they vary in function of the state of charge.

2.2.2 Weilin Luo's equivalent electric circuit model

Constant-current charging and discharging curves, measured at different C-rate, can be used in order to set-up the electric circuit model, behaviourally equivalent to the tested battery cell and to find a dependency of its main lumped parameters (open circuit voltage and impedances) on quantities like electric current and state of charge.

Considering a generic equivalent electric circuit model made of n resistors R and m RC elements, at each time instant, the voltage at the terminals is provided by solving the Kirchhoff Voltage and Current law equations.

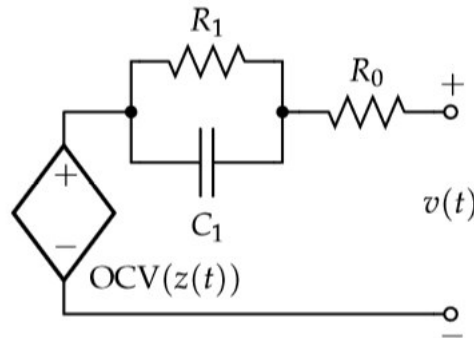


Figure 2.14 - Example of an equivalent electric circuit model with R-RC elements

$$v(t) = \text{OCV}(\text{SoC}(t)) - I(t) \sum_{i=1}^n R_i^{\text{series}} - \sum_{j=1}^m I_{R_j}(t) R_j^{\text{RC element}} \quad (2.2)$$

$$I_{R_j}(t) + I_{C_j}(t) = I(t) \quad \forall \text{ node } 1..m \quad (2.3)$$

However, if the cell is discharged (or equivalently charged) with a constant current load, as first approximation, the capacitances in the network can be considered in open circuit state [23]. As consequence, the terminal voltage is simply given by:

$$v(t) = OCV(\text{SoC}(t)) - I(t) \sum_{i=1}^{n+m} R_i(\text{SoC}(t)) \quad (2.4)$$

Which is the same voltage that would be obtained considering a pure resistive equivalent electric circuit, as the one depicted in Figure 2.16-a.

In the Equation (2.4), $v(t)$, $OCV(\text{SoC}(t))$ and $I(t)$ are known terms. In particular, the electric current $I(t)$ is the input imposed on the system, so its value is set by the user. The terminal voltage $v(t)$, is the provided output and it can be directly measured at the tabs of the cell. On the other hand, information about the dependency of the open circuit voltage on the state of charge can be gained by considering charging and discharging curves at low C-rates. Indeed, the open-circuit voltage is a static function of the state of charge, while all the other aspects of a cell's performance can be considered dynamic in some way. So, when charging and discharging at a slow rate ($C/40$ for example), the excitation of the dynamic parts is minimized and the cell can be considered in a quasi-equilibrium state [8].

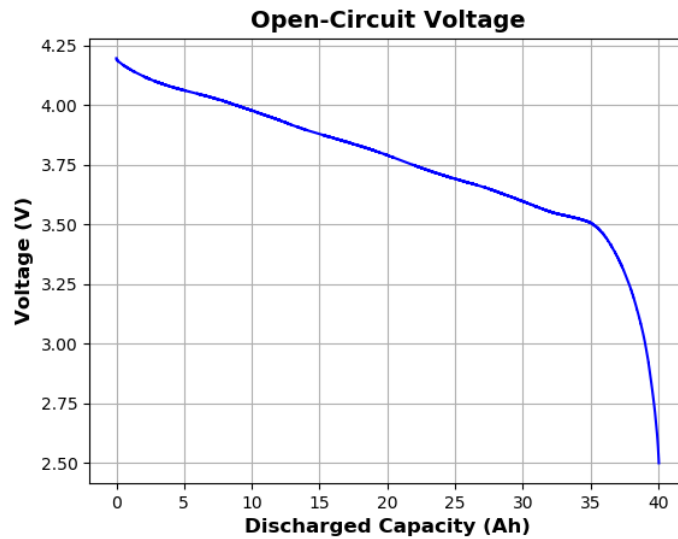


Figure 2.15 - Open Circuit Voltage in function of the Discharged Capacity (Ah)

In Figure 2.15 it is reported the relationship between open circuit voltage and discharged capacity expressed in [Ah]. Such dependency can be easily expressed in terms of State of Charge (SoC), which is defined in Equation (2.5):

$$\text{SoC} = 1 - \frac{\text{Discharged Capacity}(t)}{\text{Rated Capacity}} \quad (2.5)$$

Where the rated capacity is equal to 41Ah.

Thus, Equation (2.4) can be inverted and used to compute the total internal resistance of the battery cell:

$$R_{\text{tot}}(\text{SoC}(t)) = \frac{v(t) - \text{OCV}(\text{SoC}(t))}{I(t)} \quad (2.6)$$

In order to be able to investigate properly its dependency on the state of charge, the total resistance can be seen as the sum of different contributions, which can be associated to different source of impedance in a battery.

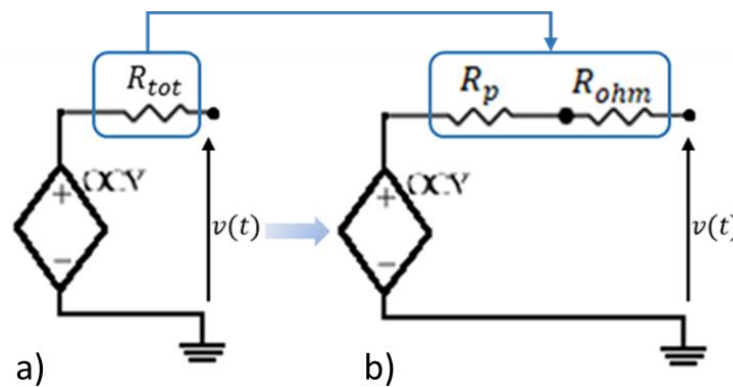


Figure 2.16 - Split of the internal total resistance

The first contribution, denoted as R_{ohm} , is associated to the ohmic resistance of the current collectors. Its value can be considered independent on the state of charge, since it is mainly related to the physical properties of the constituent materials, as the electrical conductivity, and to the geometry. The presence of an ohmic resistance causes an immediate voltage decline when a current pulse is applied [24]. On the other side, the polarization resistance R_p depicts the impedance related to the electrochemical processes inside the cell, as the charge transfer and the diffusion. This contribution is not constant, but it is State-of-Charge dependent. In particular an exponential increase of R_p is supposed as long as the state of charge goes to zero [14] [23]. This behaviour can be attributed to the high rate consumption of the reactants at the end of a discharge cycle [23].

2.2.3 Lumped parameters evaluation

The first step for the characterization of the adopted equivalent electric circuit model consists in estimating the Ohmic resistance R_{ohm} and studying the dependency of the polarization resistance R_p as function of the State of Charge SoC . In this first stage, the dependency of the lumped parameters (R_{ohm} and R_p) on the electric current has been neglected and the analysis for a fixed discharge rate has been performed. In particular, data collected during the discharge at 2C-rate have been employed.

Ohmic Resistance

As the presence of the ohmic resistance causes an immediate voltage drop when the current pulse is applied, its value can be evaluated by considering the potential difference between the equilibrium voltage OCV and the measured terminal voltage $v(t)$ after the first time instant.

$$R_{ohm} = \frac{OCV(t = 0) - v(t = \Delta t)}{I(t)} \approx 0.7m\Omega \quad (2.7)$$

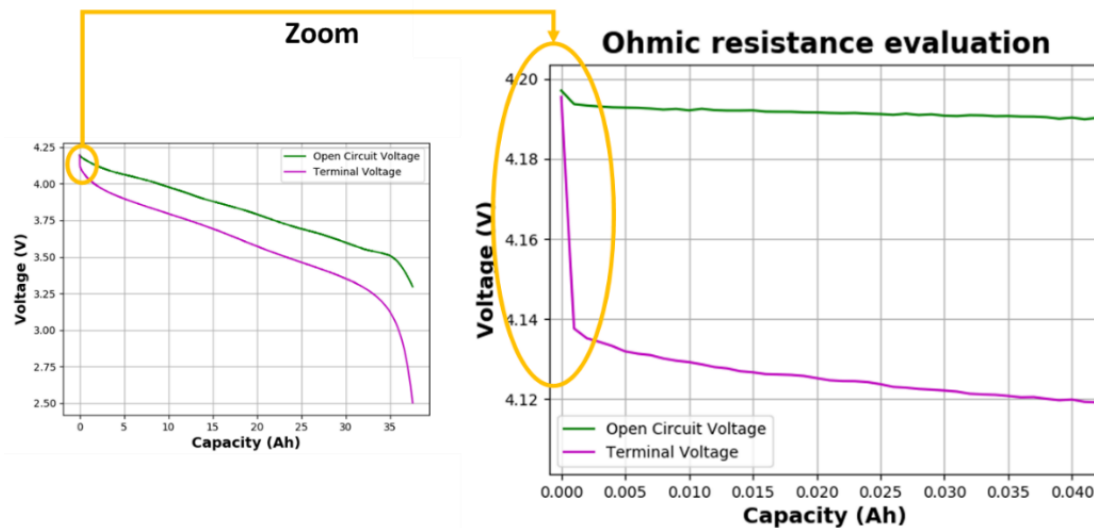


Figure 2.17 - Ohmic resistance evaluation

With this approach, the estimated value for R_{ohm} is $0.7m\Omega$.

Polarization Resistance

On the other hand, the polarization resistance $R_p(\text{SoC}(t))$ can be studied considering the equation (2.6), which computes the total internal resistance for each level of the state of charge and subtracting the ohmic contribution, R_{ohm} .

$$R_p(\text{SoC}(t)) = \frac{\text{OCV}(\text{SoC}(t)) - v(\text{SoC}(t))}{I(t)} - R_{ohm} \quad (2.8)$$

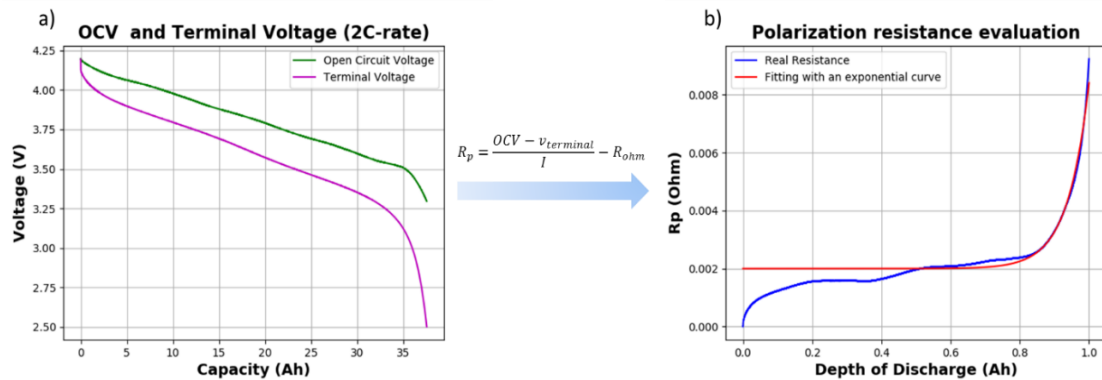


Figure 2.18 - Polarization Resistance evaluation

The trend of the evaluated polarization resistance as function of the state of charge $R_p(\text{SoC}(t))$, shows the expected exponential behaviour supposed in the literature [14] [23]. For a sake of simplicity in the further 3D-modelling, the obtained curve (blue curve in 2.18 –b) has been fitted with an exponential curve in the form [23]:

$$R_p(\text{SoC}(t)) = a_1 + a_2 e^{a_3(1-\text{SoC}(t))} \quad (2.9)$$

The regression of $[a_1, a_2, a_3]$ parameters has been performed using the *scipy.optimize* module in Python, which makes use of the nonlinear least squares algorithm.

```
#Fitting with an exponential curve
#Function that computes residuals for the ls optimization
def fun(x,soc,y):
    d = 1-soc
    return (x[0]+x[1]*np.exp(x[2]*d))-y

#Initial estimate
x0 = np.array([0,0,0])

#Running of the algorithm
res_lsq = least_squares(fun, x0, loss = 'soft_l1', f_scale = 0.001, args=(soc, Rp))

#Vector of parameters [a1, a2, a3]
a = res_lsq.x
```

Figure 2.19 - Regression of $[a_1, a_2, a_3]$ parameters

The regressed values are reported in Table 2.4:

a_1	a_2	a_3
2e-3	5.87e-10	16.2

Table 2.4 - Estimated parameters values

2.2.4 Dependency of the lumped parameters on the electric current

Besides the relationship with the state of charge, the influence of electric current on the lumped parameters must be also investigated. Such analysis can be carried out by comparing among each other measurements at different discharging currents.

Plotting together curves referring to different C-rates, it is well evident that as long as the entity of the electric current load increases, the discharged capacity significantly reduces. This behaviour should be related in some way to the trend of the internal resistance and used in order to model its dependency on the current. In particular, for the same reasons explained in Section 2.2.2, the ohmic resistance can be considered invariant with respect to the electric current, which may have only secondary effects on such parameter. Indeed, the physical quantities characterizing the materials, as the electrical conductivities, may be influenced on the temperature increase that occur especially at high C-rates. However, these side effects will be not taken into account in the modelling.

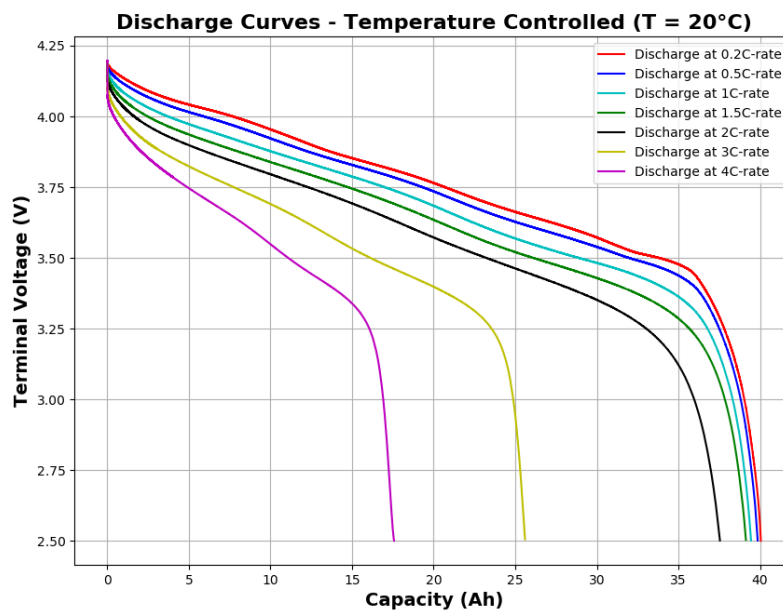


Figure 2.20 - Discharging curves at different C-rates

Consequently, in order to understand in which way the effect of the electric current on the discharge curves can be related to the polarization resistance, for each C-rate, the values of $R_p(\text{SoC}(t))$ have been computed using the Equation (2.8). Results have been plotted in the same plane as function of the discharged capacity (Figure 2.21).

The comparison among the R_p curves clearly show that their trend at different C-rates is always the same. What is changing is that as long as the discharge current increases, the curves shrink on the x-axis. In other words, the exponential branch occurs at smaller values of discharged capacity.

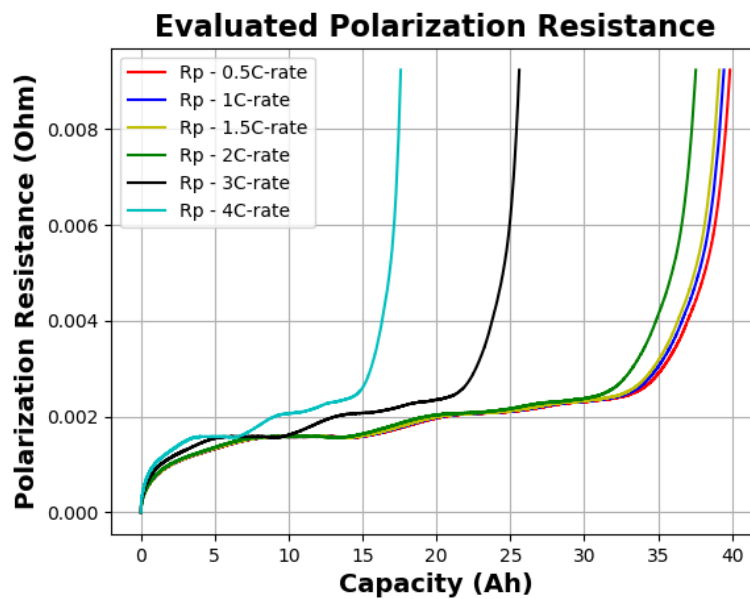


Figure 2.21 - Polarization Resistance at different C-rates

The examined behaviour can be modelled by introducing a new quantity, which will be identified as **Relative State of Charge, SoC_i** . The adjective “relative” is employed to distinguish this new variable from the concept of State of Charge used until this moment and described by the equation (2.5), which, from now on, will be denoted as Absolute State of Charge. The definition of the Relative State of Charge has been taken from the NTGPTable model provided by Battery Design Studio Software [25]:

$$\text{SoC}_i = 1 - (1 - \text{SoC}) \frac{Q}{C_{\text{Ah},I}} \quad (2.10)$$

In other words, in the Relative State of Charge definition, the actual discharged capacity at the time instant t , defined as:

$$C_{\text{discharged}}[\text{Ah}] = \int_0^t I dt \tag{2.11}$$

is penalised of a factor proportional to the ratio between the rated capacity of the battery cell (Q) and the total discharged capacity at the electric-current I ($C_{Ah,I}$). This ratio is indicated with η :

$$\eta = \frac{Q}{C_{Ah,I}} \tag{2.12}$$

In that way, the relationship providing $R_p(\text{SoC}(t))$ and depicted in the equation (2.9) is always the same, in terms of shape and values of the parameters $[a_1, a_2, a_3]$. However, in order to obtain the fitting of the curves at every C-rate, the equation must be entered with the Relative State of Charge, instead of the Absolute one.

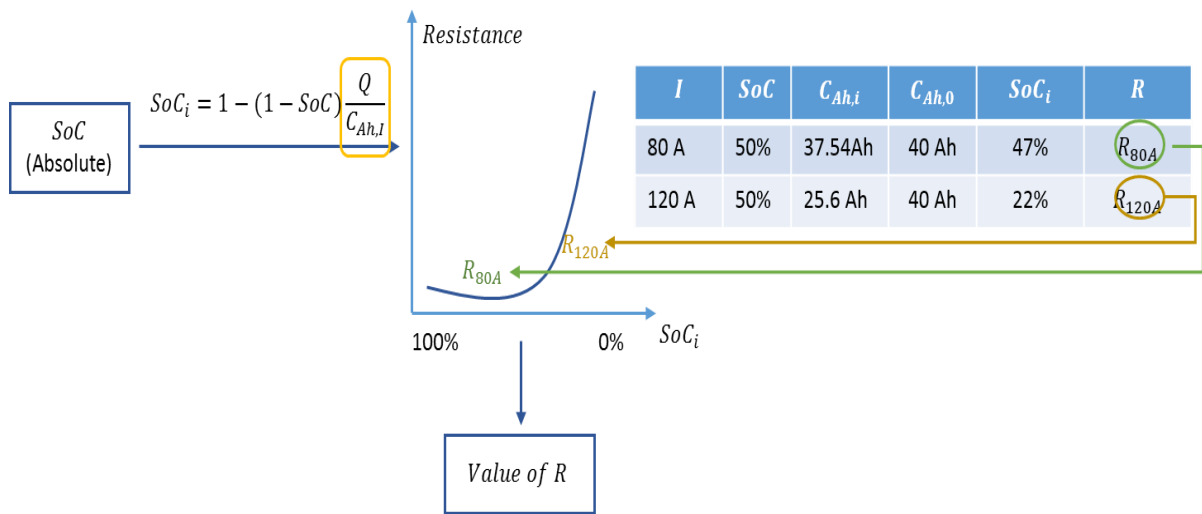


Figure 2.22 – Example of computation of the polarization resistance value at different C-rate

This modelling requires the knowledge of the η parameter at each C-rate. Nevertheless, measurements have been carried out only for a certain number of load electric currents. So, a possible mathematical formulation providing the value of η as function of the actual discharge current has been searched, by plotting its known values coming from measurements in function

of the electric current and then by interpolating them with a cubic function. Also in this case the regression has been performed using the *scipy.optimize* Python module:

$$\eta(I) = (3.13E - 7)I^3 + 1 \quad (2.13)$$

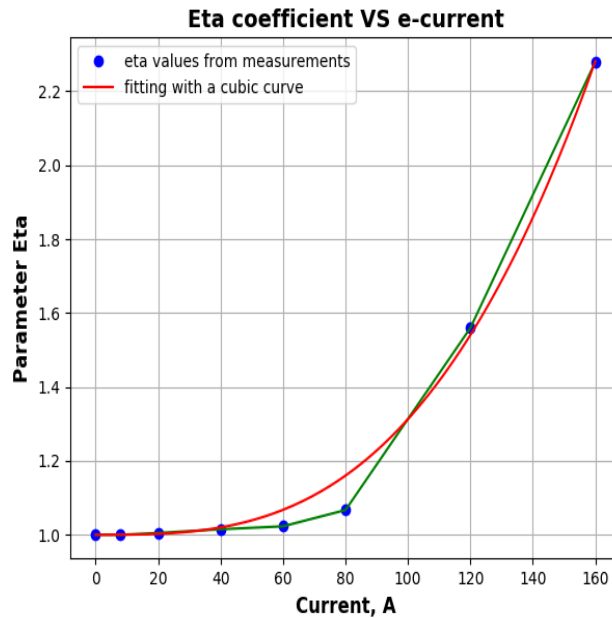


Figure 2.23 - η parameter as function of electric current

Obviously, being it a cubic curve, the value of η would infinitely increase with the current. Consequently, the corresponding value of maximum discharged capacity would become smaller and smaller, reaching zero-value at infinity. However, from a physical point of view, having a maximum discharged capacity equal to zero is meaningless. For this reason, the cubic curve is saturated to a maximum value η_{max} , corresponding to a discharged capacity equal to $C_{Ah,I}^{lim}$.

2.2.5 First validation of the model

In order to test the goodness of the lumped parameters modelling (R_o and R_p) in terms of dependency on state of charge and electric current, a comparison between simulated and measured discharged curves has been performed.

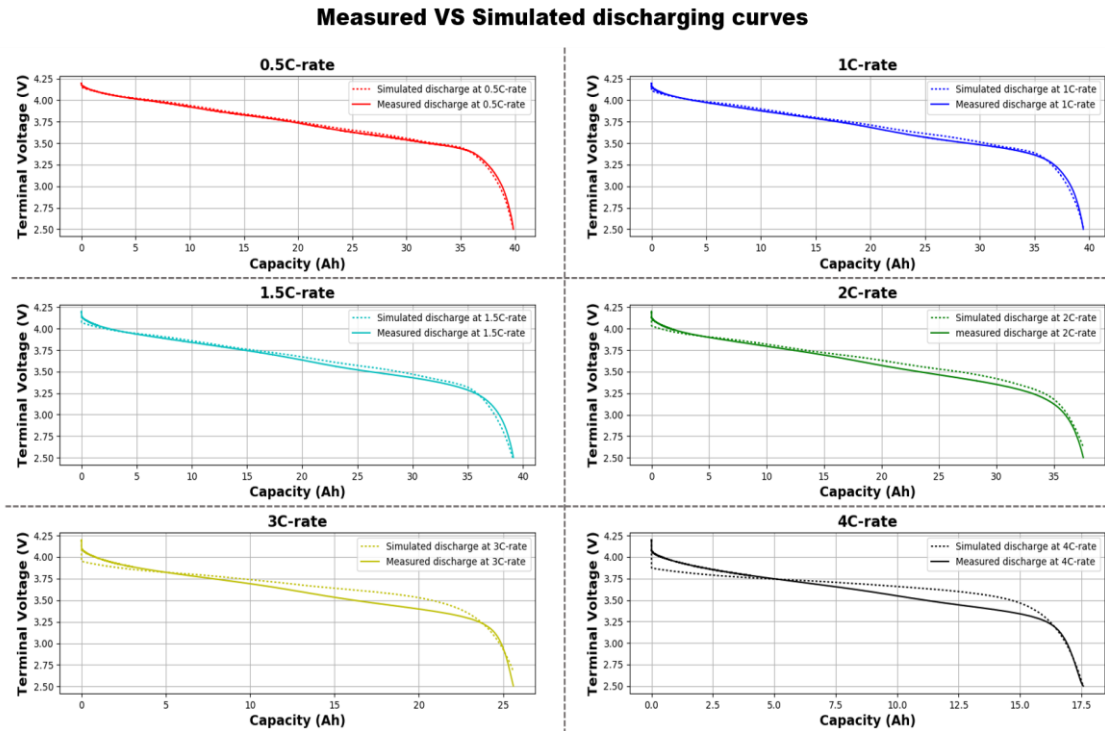


Figure 2.24 - Comparison between measured and simulated discharge curves at different C-rates

Generally speaking, the simulated curves follow quite well the measured ones at every C-rate. However, in the first stages of the discharge, a mismatch can be noticed, which becomes more evident with the increasing of the electric current load.

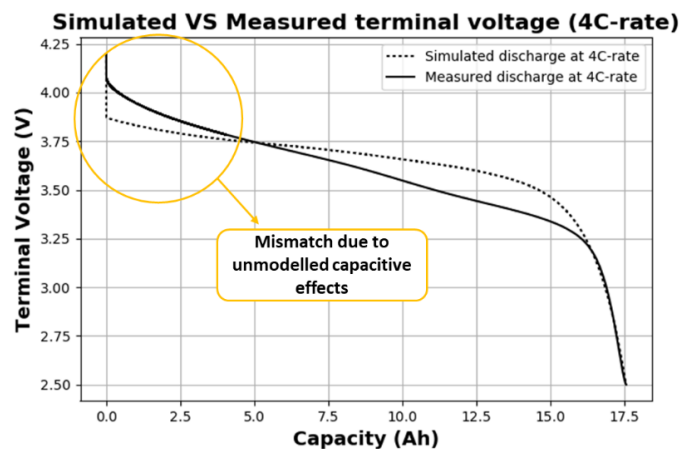


Figure 2.25 - Mismatch between simulated and measured terminal voltages at high C-rates

Such discrepancy between measured and simulated terminal voltages in the initial part of the curves can be attributed to the capacitive effects of the battery cell, mainly related to the presence of the electrical double layer at the interfaces between electrodes and electrolyte [9]. When the load electric current is applied, there is a transient, which makes the assumption of capacitances in open circuit state not true. Only when the transient extinguishes, the simplified modelling described in section 2.2.2 can be adopted.

Information about the overall impedance of the battery cell and, in turns, a better description of its capacitive effects, can be got from the Electrochemical Impedance Spectroscopy.

2.2.6 EIS measurements and upgrade of the model

The Electrochemical Impedance Spectroscopy (EIS) is one of the approaches used to characterize the energy storage devices as Lithium-ion batteries. It allows to collect data in a wide-frequency range and consequently to describe the internal electrochemical processes, identified by different characteristic frequencies (or equivalently, by different time constants) [14].

The EIS test is performed by perturbing the battery cell with a sinusoidal voltage and measuring the corresponding output current. Thus, knowing the amplitude of voltage and current signals and the shift angle between them, the internal cell-impedance can be completely determined in magnitude and phase [26]. The same procedure is repeated at different frequencies and state of charge.

It is clear that a small perturbing signal (in the order of few tens of mV) must be applied in input in order to keep the system near to the equilibrium. Indeed, in order to get in output the same frequencies given as input, the condition of Linear Time Invariant system must be guaranteed [22]. It derives that the Electrochemical Impedance Spectroscopy is not suitable to study the dependency of the cell internal impedance on the electric current, since when the cell is discharged at high C-rates, it is brought far away from the equilibrium condition. This is the reason why information coming from charging and discharging curves must be also considered in order to completely describe the impedance of the cell.

From previous studies, it has been found that a fifth-order R-RC electric circuit is able to guarantee a good fitting of the found internal-impedance Bode diagrams. The regression of the eleven parameters describing the circuit has been done using the *scipy.optimize* Python module.

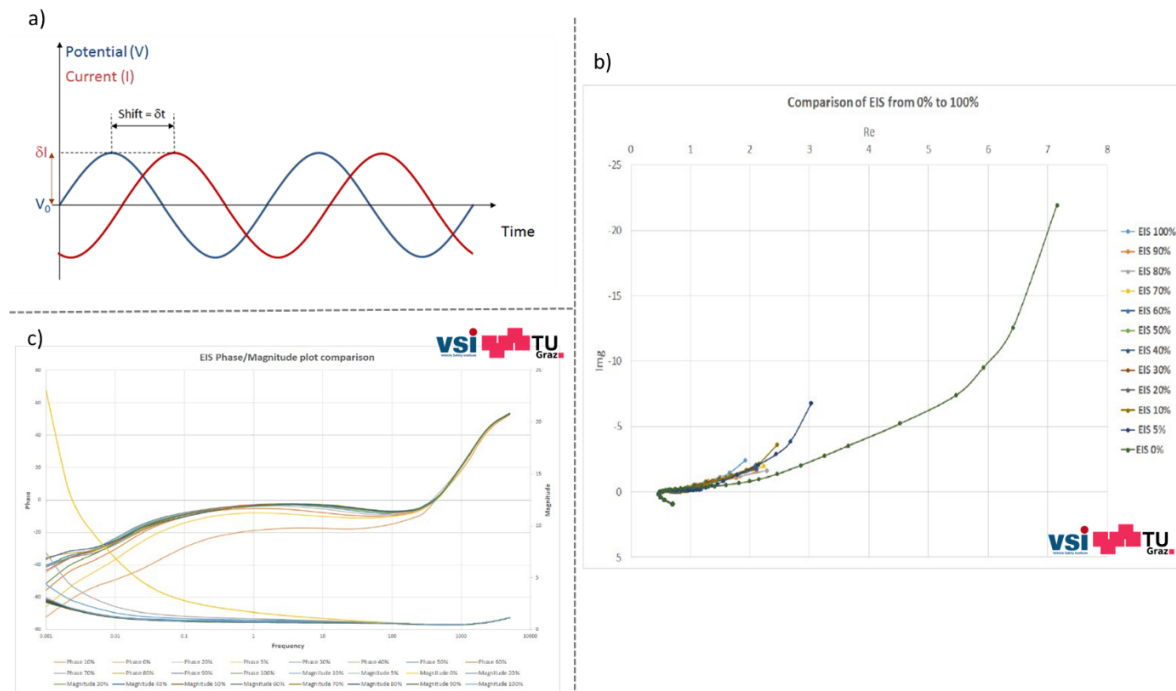


Figure 2.26 – EIS measurements: a) schematic representation of the potential excitation and current response in the measurement setup (from literature); b) Resulting cell internal impedance at different SoC: Nyquist plot (b) and Bode diagram (c) [27]

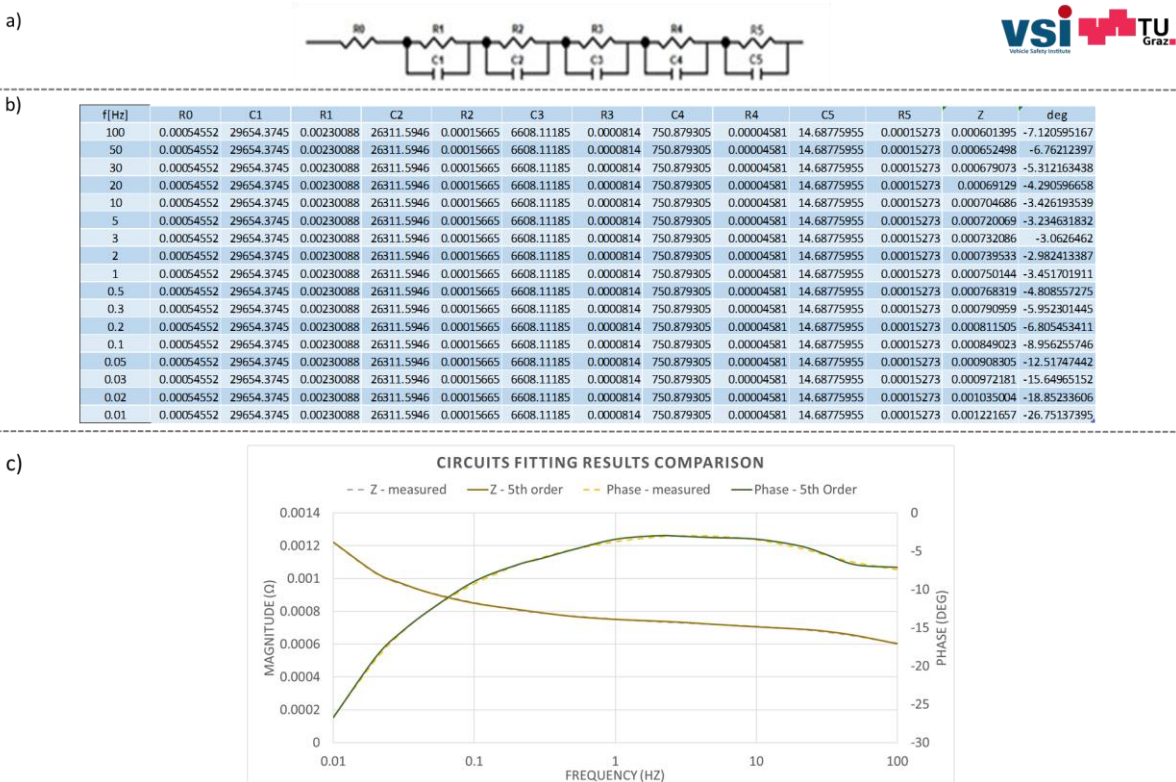


Figure 2.27 - Parameters extraction from EIS measurements: a) equivalent electric circuit model; b) Regressed parameters values at 100% SoC; c) Fitting of the Bode Diagrams with a 5th-order equivalent circuit

Results shown in Figure 2.27 refers to the fitting carried out at 100% State of Charge, in a frequency range spacing from 10mHz to 100Hz. The same procedure must be repeated at each State of Charge level for which measurements have been collected. This analysis allows to derive the same conclusions made studying the charging and discharging curves, about the trend of the resistances as function of the State of Charge. In particular the ohmic series resistance, here denoted as R_0 , remains constant, while the five resistances belonging to the RC elements (whose sum was previously denoted as polarization resistance) show an exponential behaviour when the State of Charge decreases.

From Figure 2.28 and values reported in Table 2.5, it is clear that the main contribution to the overall internal resistance is provided by the first RC parallel, where R_1 is spacing in a range of $[10^{-3} \div 10^{-2}] \Omega$. The order of magnitude of the associated time constant τ_1 is some tens of seconds (about 60s). It derives that the transient on this RC component requires some hundreds of seconds to extinguish, so it must be taken into account in the modelling. Instead, the dynamics related to the remaining RC elements are faster, since the corresponding time constants are at least one order of magnitude lower than the τ_1 value. As consequence, in first approximation, the assumption of capacitances in open circuit state when a constant current load is applied on the battery cell, can be considered true also in the first stages of the discharge.

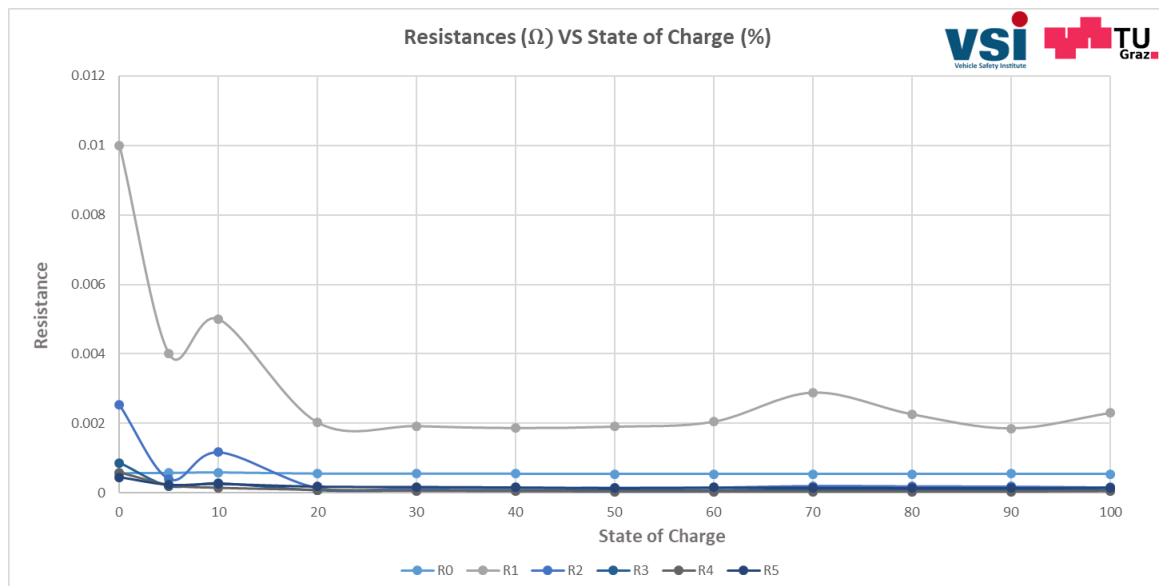


Figure 2.28 - SoC dependency of the 5th-order equivalent electric circuit resistances

RC element	R Parameter	Order of Magnitude [Ω]	τ Parameter	Order of Magnitude [s]
First RC	R_1	$10^{-3} \div 10^{-2}$	τ_1	$10 \div 10^2$
Second RC	R_2	$10^{-4} \div 10^{-3}$	τ_2	$1 \div 10$
Third RC	R_3	$10^{-5} \div 10^{-4}$	τ_3	$10^{-1} \div 1$
Fourth RC	R_4	$10^{-5} \div 10^{-4}$	τ_4	$10^{-2} \div 10^{-1}$
Fifth RC	R_5	10^{-4}	τ_5	$10^{-3} \div 10^{-2}$

Table 2.5 - Order of magnitude of the regressed parameters

For all the presented reasons, the previously considered 1D-equivalent electric circuit, depicted in Figure 2.16 (b), has been modified as shown in Figure 2.29:

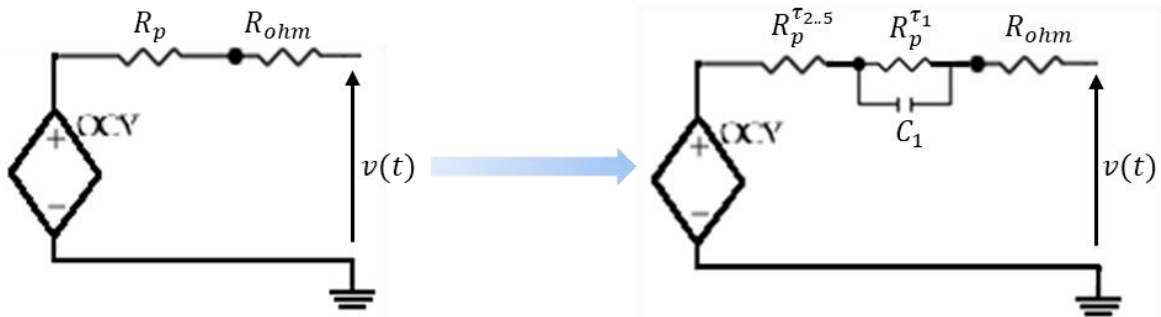


Figure 2.29 - Updated 1D-equivalent electric circuit model

Since the resistance R_1 introduced for the fitting of the EIS is comparable in terms of shape and minimum and maximum values to the polarization resistance R_p of the pure resistive equivalent circuit, the corresponding resistance $R_p^{\tau_1}$ in the updated model has been modelled using the Equation (2.9) with the same values of the coefficients $[a_1, a_2, a_3]$, provided in Table 2.2. The value of the capacitance C_1 instead, can be computed at each State of Charge, considering that the time constant of the first RC element is $\tau_1 = 60$ s (result coming from EIS). Concerning the parameter $R_p^{\tau_{2..5}}$, it models the sum of those resistances belonging to the RC elements with the fastest dynamics, for which the assumption of capacitances in open circuit state can be always done. Also such parameter should be State of Charge dependent. However, since its overall value is at least one order of magnitude lower than the values of $R_p^{\tau_1}$, it is supposed to be constant with the State of Charge, as the ohmic resistance R_{ohm} . Thus, in the

updated model, the sum of R_{ohm} and $R_p^{\tau_{2..5}}$ must be near to the constant value assigned to the SoC-invariant resistance of the old pure resistive model (Equation (2.7)).

Old model (pure resistive)	Updated model	
R_{ohm}	R_{ohm}	$R_p^{\tau_{2..5}}$
0.7 m Ω	0.54 m Ω	0.15 m Ω

Table 2.6 - SoC-invariant parameter values: old model VS new model

For the new model, the following set of differential equations must be solved [8] in order to get the terminal voltage $v(t)$:

$$v(t) = OCV(\text{SoC}(t)) - I(t)(R_{ohm} + R_p^{\tau_{2..5}}) - I_{R_p^{\tau_1}}(t)R_p^{\tau_1}(\text{SoC}(t)) \quad (2.14)$$

$$I(t) = I_{R_p^{\tau_1}}(t) + I_{C_1}(t) = I_{R_p^{\tau_1}}(t) + \tau_1 \frac{dI_{R_p^{\tau_1}}(t)}{dt} \quad (2.15)$$

The discrete-time solution of the Equation (2.15) can be written as:

$$I_{R_p^{\tau_1}}[k+1] = \exp\left(-\frac{\Delta t}{\tau_1}\right) I_{R_p^{\tau_1}}[k] + (1 - \exp\left(-\frac{\Delta t}{\tau_1}\right)) I[k] \quad (2.16)$$

Correspondingly, the terminal voltage at the time instant $[k]$ can be computed as:

$$v[k] = OCV(\text{SoC}[k]) - I[k](R_{ohm} + R_p^{\tau_{2..5}}) - I_{R_p^{\tau_1}}[k]R_p^{\tau_1}(\text{SoC}[k]) \quad (2.17)$$

For a sake of completeness, also the discrete-time form of the Equation (2.5) for the computation of the Absolute State of Charge is reported (a similar equation can be also written for the Relative State of Charge):

$$\text{SoC}[k+1] = \text{SoC}[k] - \frac{\Delta t}{Q} I[k] \quad (2.18)$$

2.2.7 Validation of the updated model: discharging curves fitting and energy check

As already done for the pure resistive equivalent electric circuit, a first validation of the new 1D proposed model has been performed by comparing the simulated discharge curve at different C-rates with the measured ones.

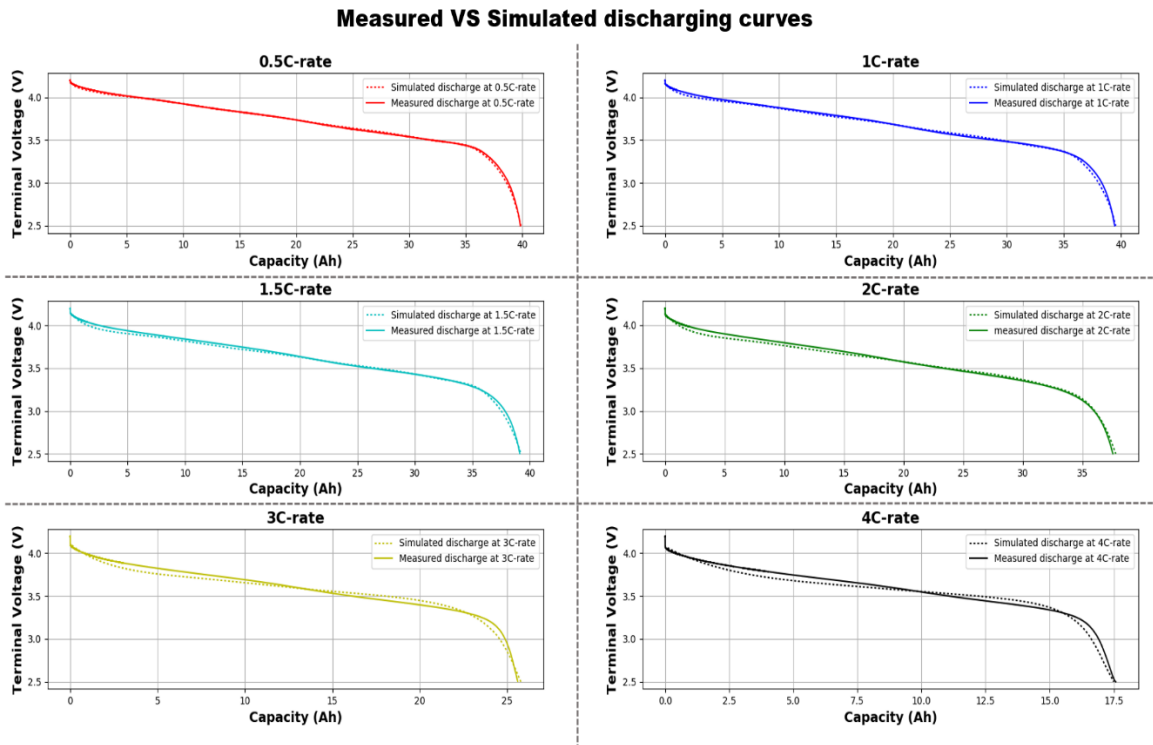


Figure 2.30 - Comparison between measured and simulated discharge curves at different C-rates (new model)

It is well evident that with the introduction of the capacitive effects, the mismatch between the curves in the first stage of discharge has been successfully compensated.

Moreover, as further validation step, the obtained model has been employed in order to make a prediction of the total heat generated and of the maximum temperature that can be reached in adiabatic conditions when a constant-resistance load is applied. Besides the Equations (2.9), (2.10), (2.16), (2.17) and (2.18) used in order to solve the electrical problem, the following discrete-time equations have been also implemented, to get information about the final maximum temperature:

- Heat power produced by Joule effects on the resistance R_i :

$$P_{R_i} [k] = I_{R_i}^2 [k] R_i [k] \quad (2.19)$$

- Heat generated on the resistance R_i :

$$E_{R_i}[k + 1] = E_{R_i}[k] + P_{R_i}[k]\Delta t \tag{2.20}$$

- Resulting temperature distribution (in adiabatic conditions):

$$T[k + 1] = T[k] + \frac{\sum P_{R_i}[k]\Delta t}{c_p m} \tag{2.21}$$

Where $c_p m$ represents the thermal mass of the battery cell in [J/K].

The computation has been done considering a load resistance $R_{load} = 1m\Omega$. The predicted maximum temperature in adiabatic conditions is about 750°C. This result is in agreement with data coming from the tests. Small differences between the simulated maximum temperature and the real one, can be justified considering that the heat generated by the exothermic reactions is not modelled by the equivalent electric circuit.

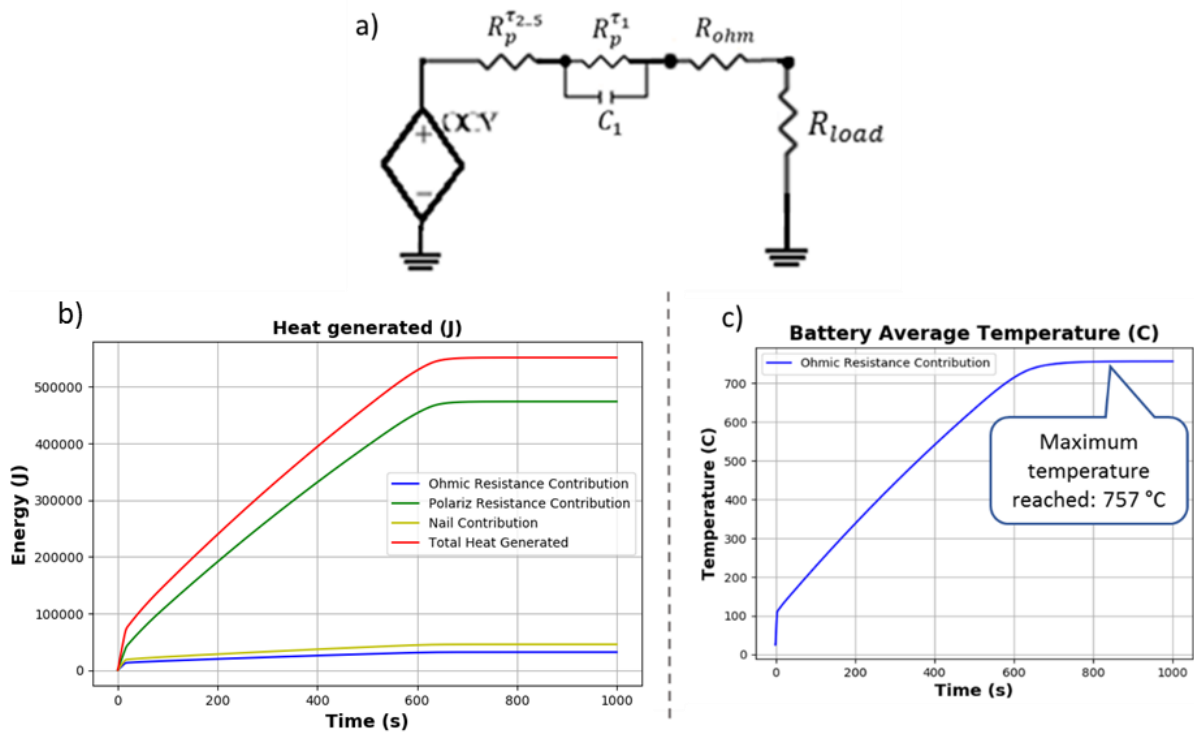


Figure 2.31 - 1D Simulation: (a) Equivalent electric circuit with constant load resistance; Total Heat Generated (b); Battery Average Temperature (c)

CHAPTER 3

3. FEM Model Development

3.1 Reasons

As already shown in Chapter 2, a 1D-equivalent electric circuit model is able to predict the voltage response of the battery cell, besides the overall heat generated and the maximum reached average temperature, when a load is attached. However, this kind of modelling is not suitable when three-dimensional problems must be treated, as the study of the temperature distribution over the whole cell. Indeed, in some load cases, especially when mechanical abuses like nail penetration occurs, high non-uniformities in the heat generated and in the temperature field may arise and information about the average behaviour may be not enough to guarantee a proper description [28] [29]. For this reason, a numerical three-dimensional electro-thermal coupled model has been developed into Siemens STAR-CCM+ software environment.

3.2 Software description

Siemens STAR-CCM+ is a Computational Aided Engineering (CAE) solution aimed at solving multidisciplinary problems involving flow (of fluids or solids), heat transfer and stress, within a single integrated user interface [30].

Into Siemens STAR-CCM+ simulation environment it is possible to import and create geometries, generate mesh, solve the governing equations and analyse the results. The simulation capabilities of the software can be further extended by customizing the environment with user libraries written in a compiled language such as C, C++ or Fortran.

3.2.1 General Simulation Process

For a better understanding of the workflow followed when a simulation in Siemens STAR-CCM+ is performed, it is worth introducing the different categories of employed objects. Mainly, there are three broad categories that can be depicted as follows:

- **Geometry – level objects**: they describe the spatial construction of the tested design. The main geometry objects are geometry parts, part surfaces, part curves and part contacts.
- **Region – level objects**: they are aimed at supporting the physics, initial conditions, boundary conditions and other sources applied to the material under test. The main region-level objects are regions, boundaries and interfaces.

- Physics – model objects: they are defined within physics continua. A physics continuum represents a material, which can be multi-component or multiphase, and the physics models that act on that material [30].

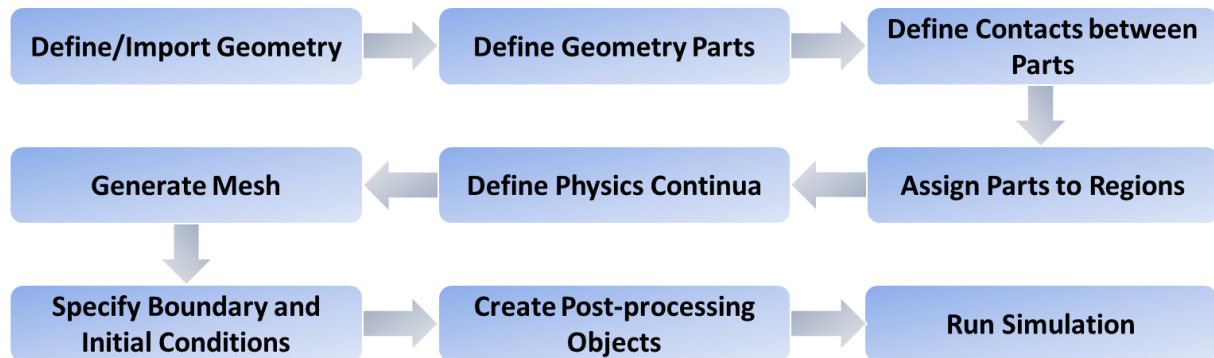


Figure 3.1 - Siemens STAR-CCM+: General Workflow

When a new simulation is started, the geometry of the object to be tested must be defined. In Siemens STAR-CCM+ environment it is possible either to import geometries from CAD and PLM systems or to modify and create CAD geometries directly, thanks to built-in capabilities.

Once the geometric data have been acquired in the 3D-CAD Models sub-node, they can be used to populate the Parts sub-node. A geometry part is a collection of surfaces and curves that the user wishes to address as one object. They provide an efficient way of organizing geometry data in preparation of meshing. It is worth highlighting that geometry parts, part surfaces, part curves and part contacts, all have unique indices that can be exploited in user libraries and field functions.

An important step to be performed before defining the regions, is the declaration of contacts between parts. Contacts are always reciprocal and can be converted into interfaces automatically when generating a new region during region assignment. Interfaces play a crucial role when the solution must be transferred between regions in a simulation.

Parts must be assigned to regions before generating mesh. Regions are volume domains in space that are completely surrounded by boundaries. Differently from interfaces, which join one region to another, boundaries are not shared between regions. The region definition is an important step in the simulation set-up because, while geometry parts are used only to define faces, edges and vertices that make up the surfaces of the model, the simulation domain on

which mesh is generated and for which physics is solved is defined using regions, boundaries and interfaces.

There may be multiple regions in a simulation. Each region can be characterized by assigning it to different physics continuum. A physics continuum can be specified under the Continua manager node. It contains a selection of physics models, such as a chosen flow solver, material models, steady or transient time model and so on. When models are selected and boundary conditions are specified, a system of equations is constructed, which is solved by numerical algorithms, also known as solvers. Different models can use the same solver and sometimes models need more than one solver. Depending on the kind of solver, either a Finite Volume Method or a Finite Element Method can be used. For the first one, Siemens STAR-CCM+ computes values at the cell centres, while for the second one it computes values at element nodes or edges. The finite volume implementation requires less memory, but it is not suitable for cases with spatial variation of the dependent variables.

Siemens STAR-CCM+ solvers find solutions to physics equations at the locations defined by the mesh. When a meshing operation is performed, a discretized representation of the involved geometric domain is obtained. The surface and volume mesh can be either generated automatically or by using a directed meshing. Depending on the used solver, the smallest closed volume obtained from the mesh is either called cell (in case of Finite Volume Method) or element (in case of Finite Element Method).

Wherever possible, Siemens STAR-CCM+ aims at generating a conformal mesh between parts. This mesh encompasses separate geometry parts without interrupting the continuity of the mesh between contacting parts. In a conformal mesh, the perimeter of the cell faces that are on the surface of one part, match up exactly with the coincident cell faces on a contacting part.

Besides the physics continuum specification, a setting of the boundary conditions and values is also needed. The types and conditions set as boundaries inform models how to deal with a boundary (or region or interface). While boundary values specify actual numerical input. Initial conditions should be also specified, in order to provide initial field data for the simulation. For steady-state simulations, the converged solution should be independent on the initial field. However the path to convergence and hence the computational effort required to reach convergence, is affected. Generally, initial conditions are specified as constants, but field functions, user codes and tables can be also introduced.

Before running the simulation, it is worth creating post-processing objects in order to be able to better analyse the results. All simulation data are stored in field functions. Field functions provide access to mesh data, geometry data, data computed by solvers, and to any data that are derived from solver data. Siemens STAR-CCM+ provides reports, scenes and plots as possible categories of post-processing objects. They allow to monitor the solution on a chosen part (regions, boundary surfaces...) while the simulation is running. Finally, the solution can be run, after a proper setting of the time-step and the stopping criteria.

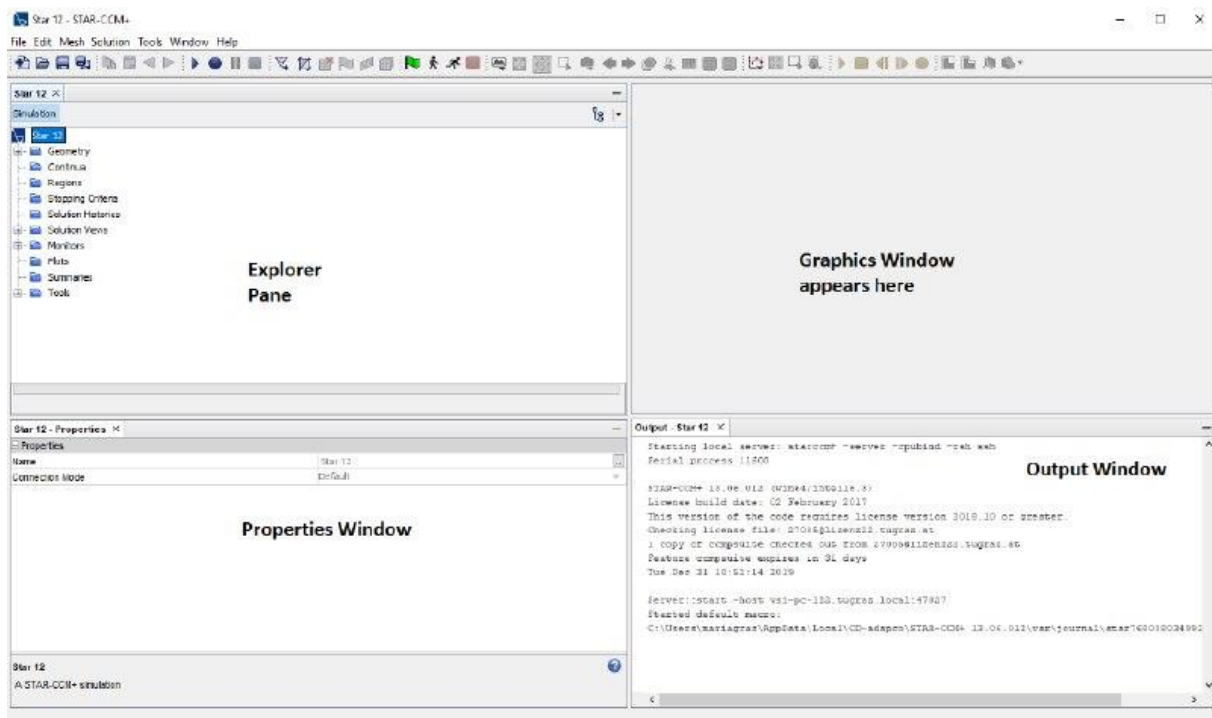


Figure 3.2 - Siemens STAR-CCM+ client workspace

3.3 Custom model development

This section documents the development of an electro-thermal 3D model for the tested Lithium-ion battery cell, which must be able to predict, besides the voltage response, the entity of the heat generated and the consequent temperature distribution when a load is applied. The modelling has been performed following a step-by-step procedure, gradually moving from an elementary block of active material to the complete cell made of n-pairs of positive and negative electrodes. This represents a typical methodology adopted in simulation engineering. For each modelling step, the goodness of the model has been tested making a comparison with voltage

and temperature results coming from measurements. The final model must be able to provide a faithful description of the cell behaviour also in abuse conditions, as the case of the nail penetration test.

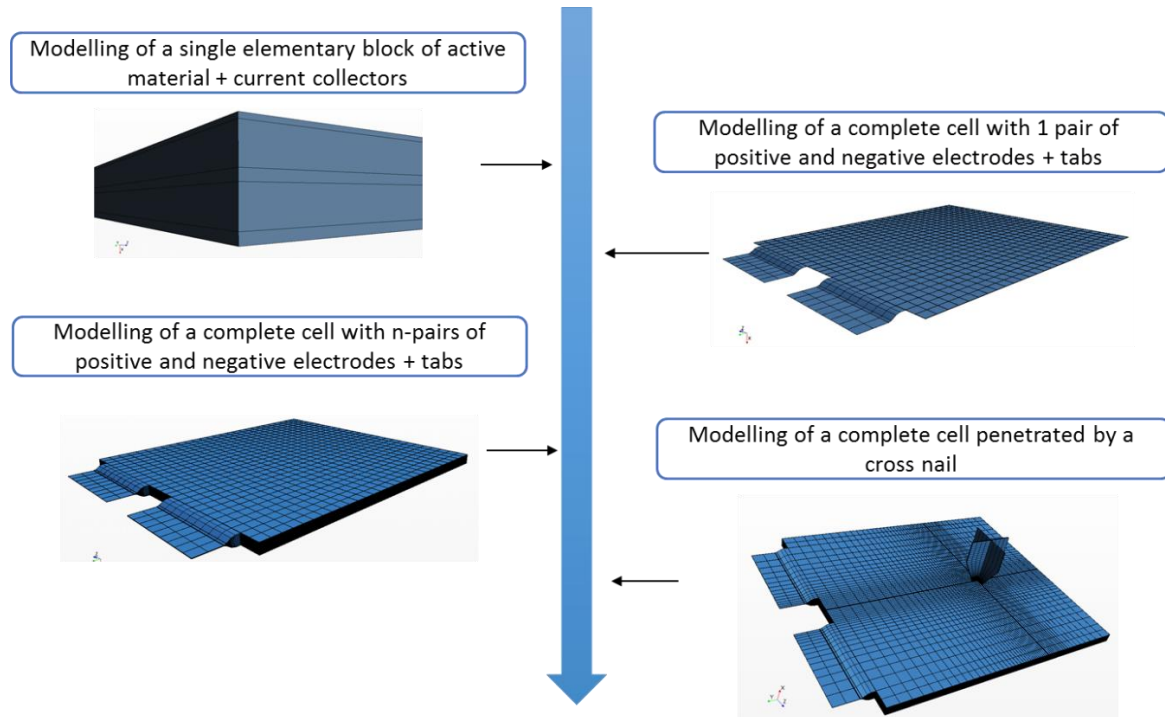


Figure 3.3 - FEM modelling: main steps

3.3.1 Geometry and mesh description

The geometry and the mesh of the tested battery cell have been realized in third-parties software and imported into Siemens STAR-CCM+ as CAE models (.inp files). In particular, the geometry has been realised in Solidworks environment through a user-tool developed in a previous work, which is able to return a faithful geometrical description of a cell once a set of parameters (as the number of electrodes, the thickness of the layers, the spacing between tabs and so on) is specified. A good modelling of the cell constitutive components is a crucial point for the evaluation of some variables, such as the ohmic resistance of the current collectors or the thermal mass of each layer.

The stack is made of 41 pairs of positive and negative electrodes. The active material is split into three main sub-layers, which are the cathode active material, the anode active material and the separator. The anode active material is in contact with another kind of sub-layer representing the copper foil, used as current collector. On the cathode side, instead, there is an

aluminium foil. As a whole, there are 21 sub-layers representing the anode current collectors and 21 sub-layers describing the cathode current collectors. The dimensions of the stack on the main section plane are $0.22m \times 0.20m$. A more detailed geometrical description of each kind of layer, in terms of thickness and volume is provided in Table 3.1.

Layer	Thickness [μm]	Volume [mm^3]
Anode Current Collector	10	9686.83
Cathode Current Collector	20	19372.95
Anode Active Material	70	126280.00
Cathode Active Material	70	129360.00
Separator	20	36960.00

Table 3.1 - Geometrical characterization of the constitutive layers

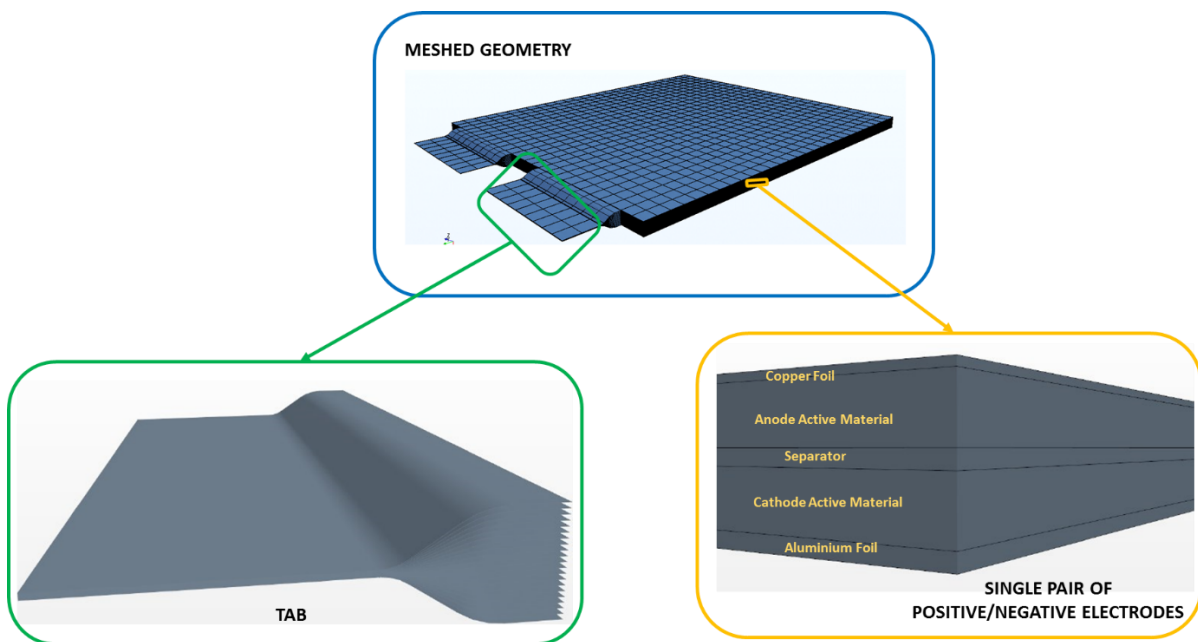


Figure 3.4 - Detailed geometry of the battery cell

The mesh has been performed into Abaqus environment. An Hexahedral element has been used, which is suitable for electro-thermal analysis.

3.3.2 Employed physics models

Due to the high inhomogeneity of the materials that constitute the stack, different physics continua need to be introduced in order to properly describe the physical properties of each kind of layer, as their electrical and thermal conductivity, the density and the specific heat. These values are listed for each introduced region, in Table 3.2. The reason why the Anode Active Material and the Cathode Active Material have been split in two more sub-regions will be clear when the modelling of the complete cell will be described.

It is worth highlighting that the characterization of the current collectors have been done taking information from the literature, since they are made of materials with known properties, as the copper and the aluminium. An exception has been made for the electrical conductivity: indeed, the nominal values provided by literature (5.96E7 S/m for the copper and 3.78E7 S/m for the aluminium), have been reduced of a factor 4 in order to take into account impurities of the material and the presence of the additional resistance introduced by the tabs welding. For the active material layers and the separator, instead, because of their heterogeneous chemical composition, the physical values have been derived from measurements taken on the overall cell and described in Section 2.1. In some cases, parameters as the electrical conductivity of Anode and Cathode Active Material, have been defined through user-defined field functions (for example UserSigma_An_Neg) instead of constant values. In this way the dependency on some quantities, like the State of Charge, can be taken into account.

Region	Solid	Density [kg/m³]	σ_{electric} [S/m]	σ_{thermal} [W/m-K]	Specific Heat [J/Kg-K]
Anode CC	Cu	8940	1.49E7	398	386
Cathode CC	Al	2702	9.45E6	237	903
Anode AM N	-	2100	UserSigma_An_Neg	1.2	1131
Anode AM P	-	2100	UserSigma_An_Pos	1.2	1131
Cathode AM N	-	2100	UserSigma_Cat_Neg	1.2	1131
Cathode AM P	-	2100	UserSigma_Cat_Pos	1.2	1131
Separator	-	2100	-	1.2	1131

Table 3.2 - materials physical properties

Concerning the models to be activated, a list and a brief description of the introduced equations is provided in the following. It is worth highlighting that the models reported in Table

3.3 refers to the current collectors and active material layers. For the separator, instead, the electrical solvers (and so the Electromagnetism and the Electrodynamic Potential models) are not enabled, since it does not contribute directly to the electro-chemical reactions and the heat generation.

<i>Group Box</i>	<i>Model</i>
Space	Three-Dimensional
Time	Implicit Unsteady
Material	Solid
Optional Models	Electromagnetism Electrodynamic Potential Ohmic Heating
Energy	Segregated Solid Energy Gradients (Selected automatically)
Equation of State	Constant Density

Table 3.3 -Selected models for anode/cathode active material and current collectors

Electromagnetism – Electrodynamic Potential Model

The fundamental equations that describe electromagnetic phenomena are the Maxwell equations, which define the electromagnetic fields induced by electric charges and currents.

$$\frac{\partial \mathbf{B}}{\partial t} + \nabla \times \mathbf{E} = 0 \quad (3.1)$$

$$\frac{\partial \mathbf{D}}{\partial t} - \nabla \times \mathbf{H} = -\mathbf{J} \quad (3.2)$$

$$\nabla \cdot \mathbf{D} = \rho \quad (3.3)$$

$$\nabla \cdot \mathbf{B} = 0 \quad (3.4)$$

Where

- ρ : electric charge density
- \mathbf{J} : electric current density
- \mathbf{E} : electric field
- \mathbf{D} : electric flux density

- H : magnetic field
- B : magnetic flux density

Maxwell's equations are used to describe a wide range of phenomena. In most of the applications, as the one treated in this modelling, the equations can be reduced to a simpler form, while retaining accuracy. Maxwell's equations imply the conservation of electric charge, which is also known as the continuity equation:

$$\nabla \cdot \mathbf{J} + \frac{\partial \rho}{\partial t} = 0 \quad (3.5)$$

Since in conducting materials the electric current density is incompressible, the Equation (3.5) reduces to:

$$\nabla \cdot \mathbf{J} = 0 \quad (3.6)$$

Moreover, a relationship between the electric current density \mathbf{J} and the electric field \mathbf{E} exists and it is provided by the generalized Ohm's law:

$$\mathbf{J} = \sigma \mathbf{E} \quad (3.7)$$

Where σ is the electrical conductivity.

Introducing the electric scalar potential ϕ and the magnetic vector potential \mathbf{A} , defined as:

$$\mathbf{E} = -\nabla\phi - \frac{\partial \mathbf{A}}{\partial t} \quad (3.8)$$

$$\mathbf{B} = \nabla \times \mathbf{A} \quad (3.9)$$

The generalized Ohm's law can be rewritten as:

$$\mathbf{J} = -\sigma \nabla\phi - \sigma \frac{\partial \mathbf{A}}{\partial t} + \mathbf{J}_{\text{ex}} \quad (3.10)$$

Where \mathbf{J}_{ex} accounts for external source of electric current density.

Inserting Equation (3.10) in the simplified continuity Equation (3.6), the following relationship is obtained:

$$-\nabla \cdot (\sigma \nabla \phi) = \nabla \cdot \left(\sigma \frac{\partial \mathbf{A}}{\partial t} \right) + \nabla \cdot \mathbf{J}_{\text{ex}} \quad (3.11)$$

Such equation is mutually coupled with a second equation, here reported for a sake of completeness:

$$\nabla \times \frac{1}{\mu} \nabla \times \mathbf{A} + \sigma \frac{\partial \mathbf{A}}{\partial t} = -\sigma \nabla \phi + \mathbf{J}_{\text{ex}} \quad (3.12)$$

By solving together these two equations, it is possible to determine the unknown fields \mathbf{A} and ϕ . However, in Siemens STAR-CCM+, two separate solvers compute \mathbf{A} and ϕ . Thus, it is also possible to solve either equation singularly to compute one of the potentials in a decoupled manner.

In particular, when the **Electrodynamic Potential Model** is selected, the solution is computed using:

$$-\oint_A \sigma \nabla \phi \cdot d\mathbf{a} - \oint_A \sigma \frac{\partial \mathbf{A}}{\partial t} \cdot d\mathbf{a} = -\oint_A \sigma \rho_\epsilon \cdot d\mathbf{a} + \int_V S_\phi dV \quad (3.13)$$

That is obtained by integrating Equation (3.11) over the cell domain. Siemens STAR-CCM+ discretizes and solves such equation using the **Finite Volume Method**. It is worth highlighting that the second term on the left-hand side, involving the magnetic vector potential is not included in the equation when the Magnetic Vector Potential Model is not selected. Instead, the quantities on the right-hand side, provide user-defined source terms that account for unresolved physics and that are implicitly included in the term $\nabla \cdot \mathbf{J}_{\text{ex}}$ in the Equation (3.11). The involved quantities are:

- S_ϕ : transfer current density
- ρ_ϵ : electromotive force density

It is possible to specify these values through the Physic Conditions Manager sub-node under the region nodes [30].

Ohmic Heating

The Ohmic Heating model solves for the heat that is generated in a conducting material due to the flow of electric current. When using the model, Siemens STAR-CCM+ computes the energy dissipation in an electrically conducting material, by exploiting the Joule Law:

$$Q = \mathbf{J} \cdot \mathbf{E} \quad (3.14)$$

Where:

- Q : heat source per unit volume $\left[\frac{W}{m^3}\right]$
- J : electric current density $\left[\frac{A}{m^2}\right]$
- E : electric potential $\left[\frac{V}{m}\right]$

Such term is added as source contribution in the energy equation:

$$\frac{d}{dt} \int_V \rho C_p T dV + \oint_A \rho C_p T \mathbf{v}_s \cdot d\mathbf{a} = - \oint_A \dot{\mathbf{q}} \cdot d\mathbf{a} + \int_V S_u dV \quad (3.15)$$

Where:

- ρ : solid density
- C_p : specific heat
- T : temperature
- $\dot{\mathbf{q}}$: heat flux vector
- \mathbf{v}_s : solid convective velocity (of for rotating bodies)
- S_u : user-defined volumetric heat source within the solid

If the **Segregated Solid Energy model** is selected, Siemens STAR-CCM+ solves the energy equation using the **Finite volume method** [30].

3.3.3 Discretization strategy: equivalent circuit splitting

The electro-thermal coupled finite element model implemented in Siemens STAR-CCM+, should be a three-dimensional extension of the 1D-equivalent electric circuit, able to predict the behaviour of the cell in terms of voltage response, heat generated and temperature distribution also locally. Based on this consideration, it is possible to elaborate a strategy for the modelling. In particular, the whole battery cell is equivalent to the parallel of 41 simpler

cells made of only one pair of positive and negative electrodes. From now on, such simple cell will be called single-layer cell. In turns, within each single-layer cell, every small element coming from the mesh of current collectors, active materials and separators substrates, can be seen as part of smallest elementary cells working in parallel. This means that, if the 1D-equivalent electric circuit described in Section 2.2 can be associated to the complete battery cell, a one-to-one correspondence could be created between each elementary cell and an equivalent electric circuit having the same complexity of the original one, but parameters value properly scaled.

As shown in Figure 3.5, the topology of the equivalent electric circuit to be implemented through the elementary cell coming from the mesh discretization, is not exactly the same of the one deeply analysed in the previous chapter. Indeed, a rearrangement is needed in order to deal with some issues related to the modelling into STAR-CCM+. The first one regards the inability of introducing directly capacitances when the electrodynamic model is selected. Indeed, as shown in Equations (3.7 – 3.13), the impedance must be modelled through a proper characterization of the electrical conductivity, which could be easily expressed in terms of resistance values. This means that some kind of mathematical artifice must be thought in order to model the transient during which the drop voltage on the polarization resistance $R_p^{\tau_1}$ slowly increases until a steady state value is reached. The modelling of this aspect, which assures a good fitting of the measured constant-current discharge curves, as explained in Section 2.2.7, becomes of fundamental importance in the first seconds of simulation of the nail penetration test. Indeed, according to the literature [12], in the first stages of the penetration, the internal short circuit is ohmically controlled, which means that the contribution of the polarization resistance $R_p^{\tau_1}$ must be negligible. Then, as long as the diffusion of the lithium-ions in the electrolyte and electrodes proceeds, the polarization resistance increases and the resulting electric current is lowered. If this transient is neglected, considering a steady state value of the polarization resistance since the beginning of the test, the peak that the electric current reaches would be underestimated. As consequence, the following model for $R_p^{\tau_1}$ has been proposed and implemented:

$$R_p^{\tau_1}[k+1] = \exp\left(-\frac{\Delta t}{\tau_1}\right) R_p^{\tau_1}[k] + \left(1 - \exp\left(-\frac{\Delta t}{\tau_1}\right)\right) R_{p,steady}^{\tau_1}[k] \quad (3.16)$$

Where $R_{p,steady}^{\tau_1}[k]$ is given by Equation (2.9).

The second matter, instead, is related to the split of the active material in its constitutive components, which are the cathode, the anode and the separator. This requires that the contributions of $R_p^{\tau_{2.5}}$ and $R_p^{\tau_1}$ must be divided in some way between the anode and the cathode active material regions. For sake of simplicity, they have been equivalently split between the two regions. In a similar way, the overall ohmic resistance R_{ohm} should be separated between the two different kind of current collectors. As consequence of this new rearrangement, the terminal voltage $v(t)$ measured at the ends of the circuit, is a differential voltage, since it has no reference to ground. This kind of representation is more near to the working principle of a real battery cell, which does not provide any current if a load is connected between one of the tabs and the ground. Instead, the electric current can flow and a drop voltage can be measured across the load if this one is connected between the two tabs. In Figure 3.5 (b) the final circuit used for simulation is depicted.

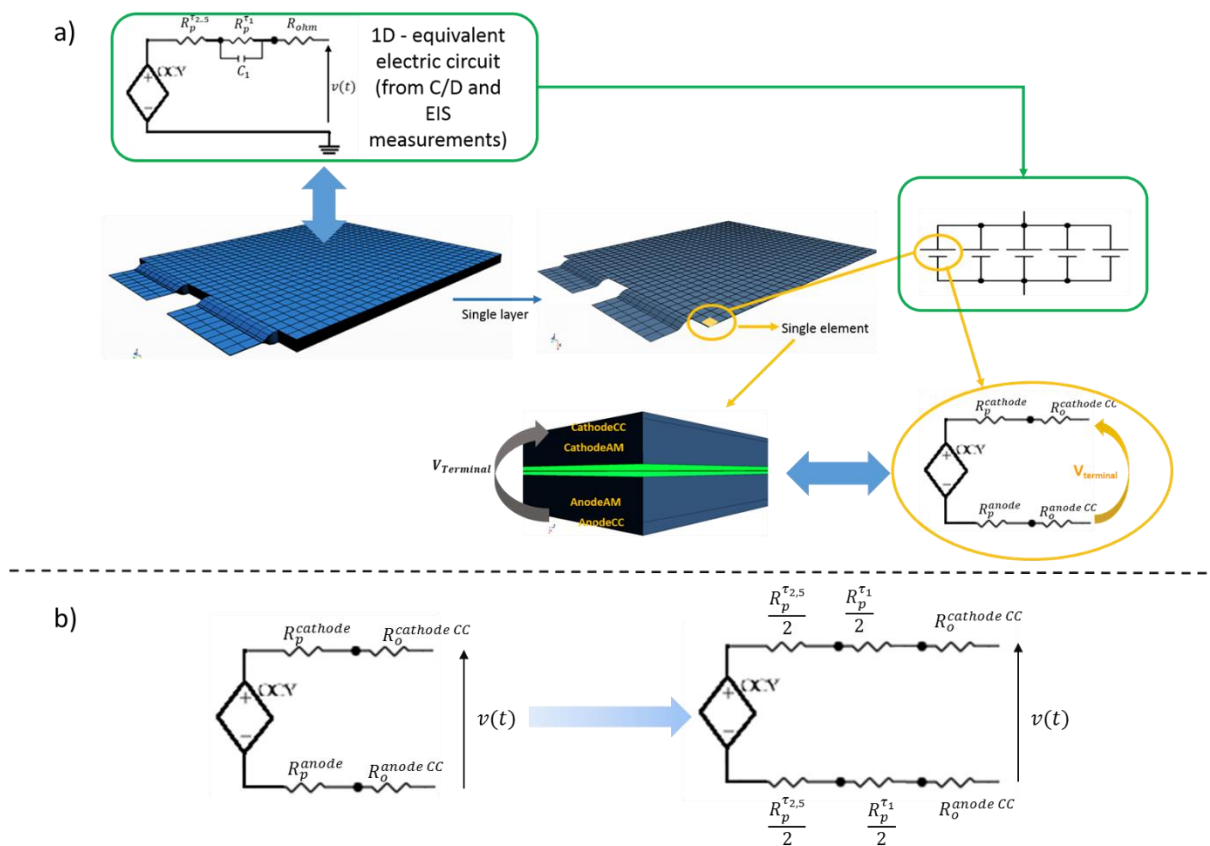


Figure 3.5 - Modelling Strategy (a) and modified 1D-equivalent circuit model (b)

3.3.4 Modelling of an elementary cell

The first step to be performed regards the electrical modelling of a single elementary block, made of simple hexahedral elements resulting from the mesh of the active material substrates and the current collectors. Boundary/interface conditions and physical properties of the constitutive materials must be specified so that the differential voltage measured between two points of the cathode and anode current collectors is equal to the terminal voltage $v(t)$.

Before proceeding with such assignment, interfaces between the different regions must be declared. In particular, the following contact-type interfaces need to be created:

- Anode Current Collector/Anode Active Material Interface
- Cathode Current Collector/Cathode Active Material Interface
- Separator/Anode Active Material Interface
- Separator/Cathode Active Material Interface

As no electric solvers are enabled for the separator, the creation of interfaces between it and the active material regions allows to impose on them voltage profiles as boundary/interface conditions. On the other hand, the interfaces definition between active materials and the corresponding current collector layer is needed for the transferring of the continuum quantities when the solution is computed.

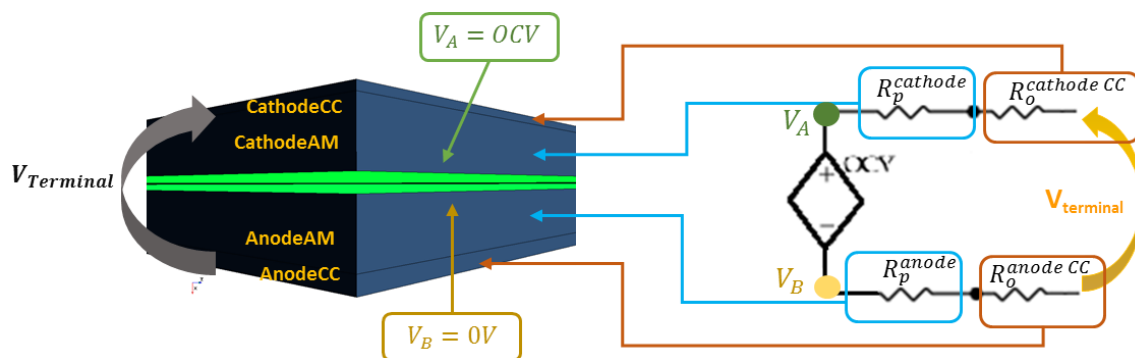


Figure 3.6 - Mapping of the equivalent electric circuit into a single elementary block

Figure 3.6 shows a possible way for the creation of a one-to-one correspondence between the one-dimensional equivalent electric circuit and the single elementary cell. Node A in the network, having a potential level equal to the open circuit voltage (imposed by the SoC-dependent generator), is implemented in the 3D model by specifying the same voltage profile

at the cathode/separator interface. A similar reasoning can be done for the Node B and the anode/separator interface.

On the other hand, the resistances of the equivalent circuit should be introduced in the cell by suitably modelling the electrical conductivity of the materials. The procedure is straightforward for the set-up of the ohmic resistance associated to the current collectors. Indeed its value is automatically defined by the geometrical parameters (as thickness and section area) and the electrical conductivities of the copper and aluminium, supposed constant. Their values are taken from the literature and indicated in Table 3.2.

More complex, instead, is the implementation of the polarization resistances, which can be associated to the anode and cathode active materials. As already explained in Section 2.2, its value is not constant, but it depends on the Relative State of Charge quantity. For this reason, based on the knowledge of such dependency and on the geometry, it is possible to express the electrical conductivity of these regions through a user defined function. Custom field functions can be set through **Tools → Field Function manager subnode** into STAR-CCM+.

- User definition of the electrical conductivity for the cathode active material:

$$\sigma_{\text{Cathode AM}}(\text{SoC}_r) = \frac{1}{R_p^{\text{Cathode}}(\text{SoC}_r)} \frac{I_{\text{AM}}^{\text{Cathode}}}{A_{\text{AM}}^{\text{Cathode}}} \quad (3.17)$$

- User definition of the electrical conductivity for the anode active material:

$$\sigma_{\text{Anode AM}}(\text{SoC}_r) = \frac{1}{R_p^{\text{Anode}}(\text{SoC}_r)} \frac{I_{\text{AM}}^{\text{Anode}}}{A_{\text{AM}}^{\text{Anode}}} \quad (3.18)$$

It is possible to introduce data regarding the open circuit voltage and the polarization resistance into the software by importing (.csv) file tables under the **Tools → Tables manager subnode**. The imported table should have, as first column, values of the independent variable (in this case the state of charge) and as second column, the values of the variable of interest. After that, the `interpolateTable` function can be used to interpolate data either in a linear way or through a spline.

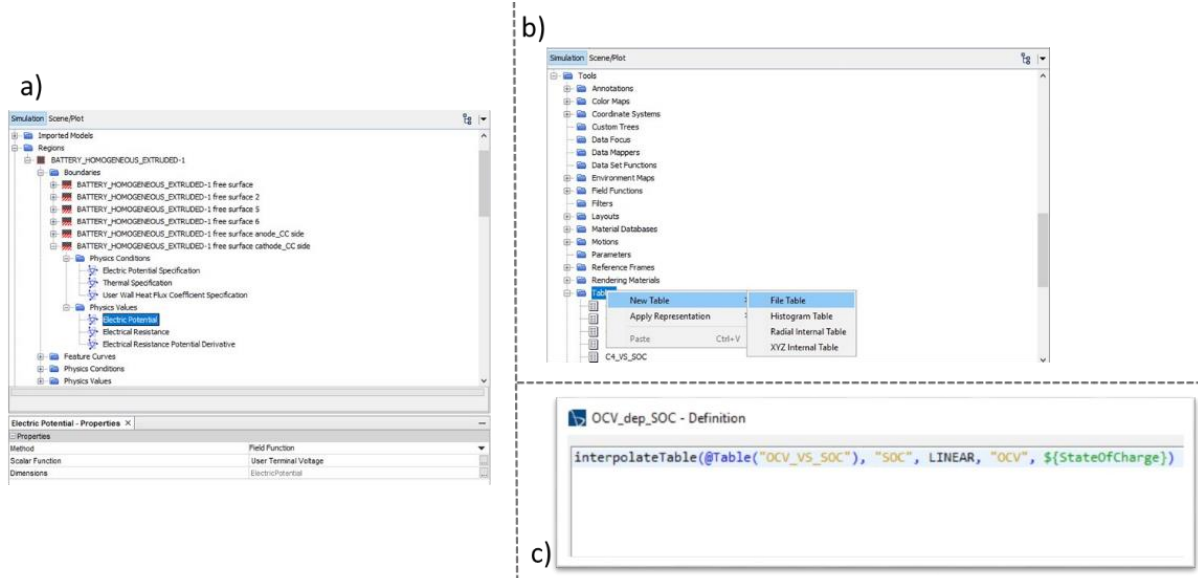


Figure 3.7 - STAR-CCM+ interface: a) Declaration of the Electric Potential boundary profile; b) Import of a file table; c) Introduction of a user function

For the models that are selected on the electrical side (Electromagnetism – Electrodynamic Potential), there is not a built-in function already available for the evaluation of the State of Charge. Thus, a user field function must be written in order to guarantee a proper computation of such state variable during the simulation and a consequent estimation of the dependent quantities, as the polarization resistance and the open circuit voltage. Equation (2.18), which computes the State of Charge in a discrete-time, has been taken as starting point for the implementation.

$$\text{SoC}[k + 1] = \text{SoC}[k] - \frac{\Delta t}{Q} I[k] \quad (3.19)$$

At each time step, the value of the electric current on the active material elementary block is read and the state of charge value is updated by subtracting the discharged capacity in the time interval Δt . Data related to the electric current are expressed in STAR-CCM+ in terms of electric current density vector field, $\mathbf{J} \left[\frac{A}{m^2} \right]$, so the equation for the state of charge must be written in terms of its components. From preliminary simulations, it has been noticed that, due to the geometry of the problem, the electric current density in the active material has one main component along the x direction, which is the one perpendicular to the main section of the pouch cell, while the components in the yz plane are negligible.

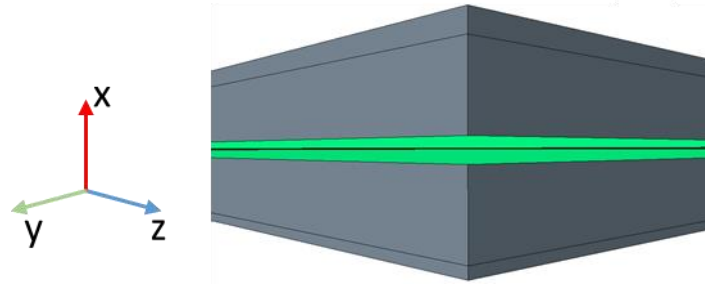


Figure 3.8 - Laboratory Reference System

As consequence, Equation (2.18) can be rewritten as:

$$\text{SoC}[k + 1] = \text{SoC}[k] - \frac{\Delta t}{Q} J_x[k] A_{AM}^{yz \text{ plane}} \quad (3.20)$$

For the computation of the state of charge at the next time step, $\text{SoC}[k + 1]$, the value at the current time step, $\text{SoC}[k]$, must be accessed. This means that a monitor in the **Monitors manager subnode** must be set-up to store the previously computed value and use it at the next iteration. In particular, a field sum monitor on the cathode and anode active material should be created with an update frequency of one time step and a sliding window equal to 1. With this setting, the current value of the state of charge, evaluated on the active material layers, is stored for the next time step and then discarded, since it is overwritten by the new value. However, monitors are automatically initialized to zero, while, if a complete discharge is simulated, the initial value of the state of charge should be 1. As consequence, in order to manage the issue, the state of charge can be computed through the following set of equations:

$$\text{SoC}[k] = 1 - \text{DoD}[k] \quad (3.21)$$

$$\text{DoD}[k + 1] = \text{DoD}[k] + \frac{\Delta t}{Q} J_x[k] A_{AM}^{yz \text{ plane}} \quad (3.22)$$

Where DoD is the Depth of Discharge.

A similar reasoning can be done for the Relative State of Charge, implemented through the Equations (3.23) and (3.24).

$$\text{SoC}_r[k] = 1 - \text{DoD}_r[k] \quad (3.23)$$

$$\text{DoD}_r[k + 1] = \text{DoD}_r[k] + \eta \frac{\Delta t}{Q} J_x[k] A_{AM}^{yz \text{ plane}} \quad (3.24)$$

Due to their complexity, these equations have not been implemented directly through the **Field Function Manager subnode**, but a user (.dll) library has been compiled and loaded in STAR-CCM+ through the **User Code Manager subnode**. In order to create a new library, (.c) files must be written for each field function that should be implemented. Besides them, a library registration function, named **uclib.c**, is needed in order to register each user function in the library, by providing its name and the needed arguments. The name registration is done with calls through `ucfunc`, while the argument registration is carried out by calling the `ucarg`. When the requested arguments are registered, the name of STAR-CCM+ variables must be inserted. They can be read by accessing to the **Field Function manager subnode** in the **Tools node**. Besides the `uclib.c` file, a header file, **uclib.h** has to be created in order to declare the types of variables that are used in C user functions. Once all the needed source files have been created, they are compiled using Microsoft Visual C++ 2019 compiler, so that the desired (.dll) file can be finally loaded into the Software.

3.3.5 Modelling of a single-layer cell

After the set-up of an elementary cell, as next step, the model has been extended to a complete single-layer cell, made of only one pair of positive and negative electrodes. A first validation has been carried out on such simplified cell, focusing in particular on its electrical behaviour, while neglecting its thermal aspects.

As already mentioned in Section 3.3.3, the characteristics of a single-layer cell are given solving the parallel among all the elementary cells that constitute the layer.

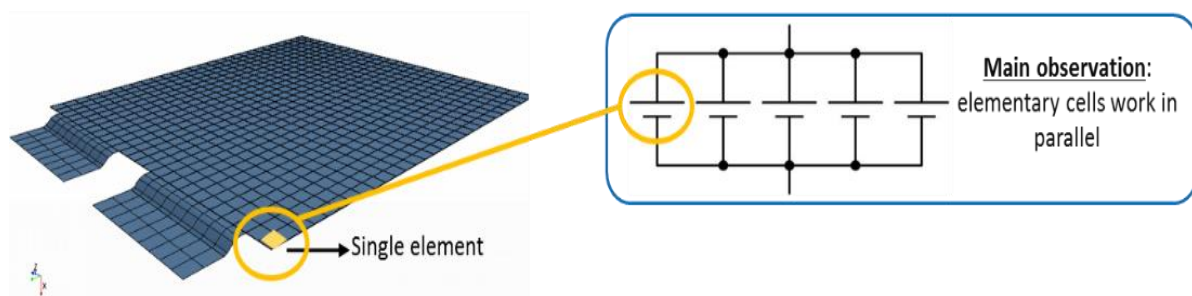


Figure 3.9 - Relationship between a single-layer cell and an elementary cell

Based on this assumption, a relationship linking the single-layer cell internal resistance with the resistance of an elementary cell can be written:

$$R_{\text{single layer}} = \frac{R_{\text{elementary cell}}}{N_{\text{cells}}} \quad (3.25)$$

The same can be done for the nominal capacities [Ah]:

$$Q_{\text{single layer}} = N_{\text{cells}} Q_{\text{elementary cell}} \quad (3.26)$$

Concerning instead the electric potential specifications (OCV and zero-voltage profiles) to be imposed at the interfaces between cathode/anode active material and separator, no modifications are needed, due to the parallel connections between elementary cells.

Furthermore, in order to extend the equations providing the state of charge and the equivalent electrical conductivity of the active material layers, relations between the geometrical parameters of the single-layer cell and an elementary cell should be also considered.

- Thickness:

$$l_{\text{AM}}^{\text{single layer}} = l_{\text{AM}}^{\text{elementary cell}} \quad (3.27)$$

- Section Area:

$$A_{\text{AM}}^{\text{single layer}} = N_{\text{cells}} A_{\text{AM}}^{\text{elementary cell}} \quad (3.28)$$

In particular, using the equations (3.26) and (3.28) into Equation (3.22), it is possible to show that the expression for the computation of the depth of discharge, and consequently the state of charge (both absolute and relative), remains the same. In other words, the definition of the state of charge does not depend on the number of elementary cells:

$$\begin{aligned} \text{DoD}_{\text{cell}}[k+1] &= \text{DoD}[k] + \frac{\Delta t}{Q_{\text{cell}}} J_x[k] A_{\text{AM}}^{\text{cell}} = \text{DoD}[k] + \frac{\Delta t}{\frac{Q_{\text{layer}}}{N_{\text{cells}}}} J_x[k] \frac{A_{\text{AM}}^{\text{layer}}}{N_{\text{cells}}} \\ &= \text{DoD}[k] + \frac{\Delta t}{Q_{\text{layer}}} J_x[k] A_{\text{AM}}^{\text{layer}} = \text{DoD}_{\text{layer}}[k+1] \end{aligned} \quad (3.29)$$

$$\text{SoC}_{\text{layer}}[k] = 1 - \text{DoD}_{\text{layer}}[k] \quad (3.30)$$

Exploiting Equations (3.25), (3.27) and (3.28) into Equations (3.17) and (3.18), a similar procedure can be repeated for the user defined electrical conductivities of the cathode and anode active materials:

$$\sigma_{A,C AM}^{cell} = \frac{1}{R_{p,cell}^{A,C}} \frac{l_{AM}^{cell}}{A_{AM}^{cell}} = \frac{1}{R_{p,layer}^{A,C} N_{cells}} \frac{l_{AM}^{Layer}}{\frac{A_{AM}^{layer}}{N_{cells}}} = \frac{1}{R_{p,layer}^{A,C}} \frac{l_{AM}^{layer}}{A_{AM}^{layer}} = \sigma_{A,C AM}^{layer} \quad (3.31)$$

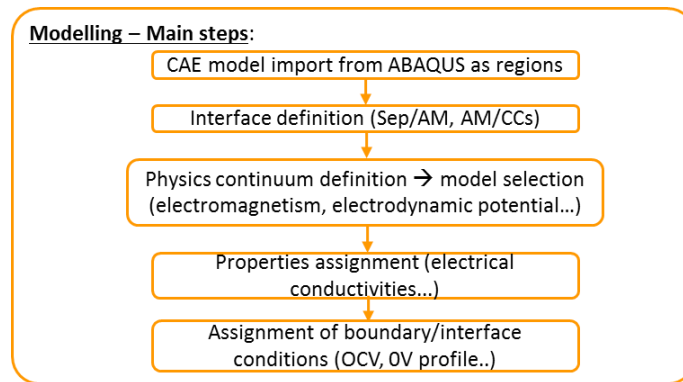


Figure 3.10 - Review of the main steps for the set up of a simulation

3.3.6 Electrical behaviour validation of a single-layer cell

In order to verify the goodness of the modelling carried out until this point, a first simulation has been set-up, with the purpose of analysing the electrical response of a single-layer cell when a constant current load is applied. For this purpose, the single-layer cell has been characterized with the values of internal resistance and total capacity of the complete battery cell, in order to get in output results comparable with voltage data coming from constant-electric-current discharging curves. In the real case, instead, one single layer contributes only for 1/41 to the overall capacity and resistance of the cell, as will be discussed in the next sections. A 0.5C-rate discharge has been simulated, by imposing a constant current profile at the end of the two tabs, as depicted in Figure 3.11.

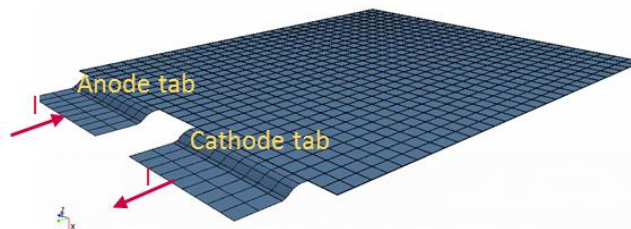


Figure 3.11 - Simulated procedure: 0.5C discharge ($I = 20A$)

The simulation has returned information about the electric current density distribution in the active material and in the current collectors, besides the time evolution of the terminal voltage at the tabs. The user-defined state of charge field function has been also monitored on the cathode and anode active material, in order to test the correctness of the implemented equations.

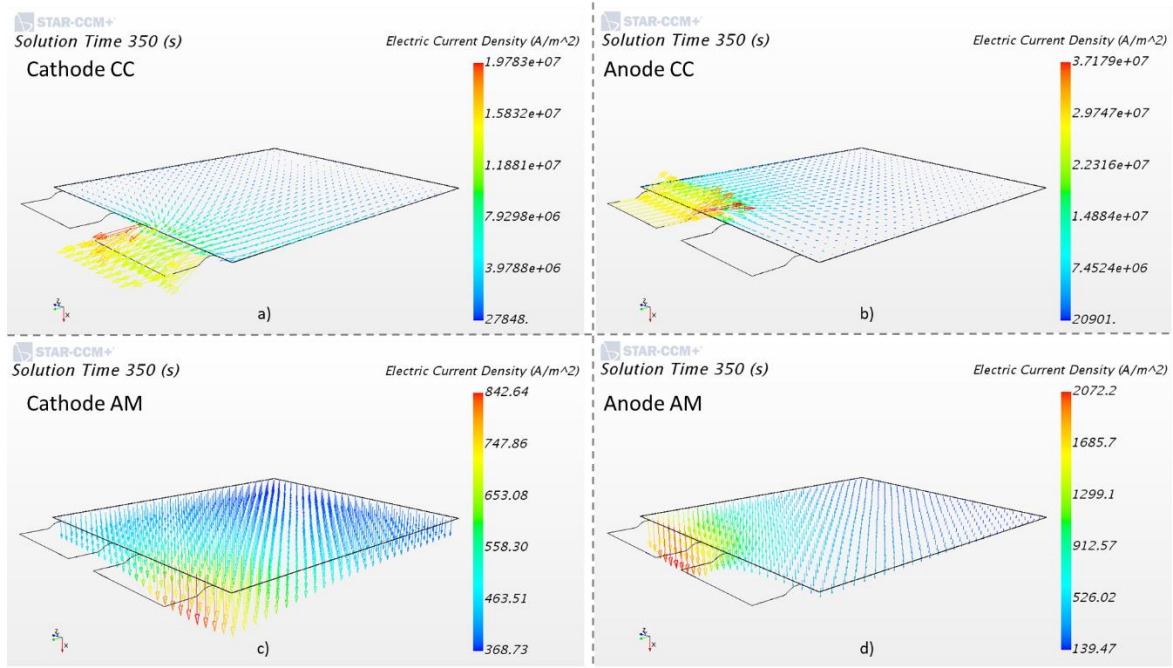


Figure 3.12 - Electric current density distribution in the (a) cathode current collector, (b) anode current collector, (c) cathode active material, (d) anode active material

From Figures 3.12-a and 3.12-b it is possible to observe that the electric current density vector field in the current collectors is parallel to the main section of the pouch cell. In other words, it has components only in the yz plane of the laboratory reference system (Figure 3.8). Higher densities are obtained near to the tabs, as expected. Instead, Figures 3.12-c and 3.12-d clearly show that within the active material, the electric current density vector field is mainly directed in the x-direction, transversally to the main section area. This behaviour validates the assumption made in Section 3.3.4 for the writing of the state of charge Equation (3.20). As further check, the integral of the electric current density over the anode/separator and cathode/separator interface surfaces has been computed, returning in both cases 20A, as expected.

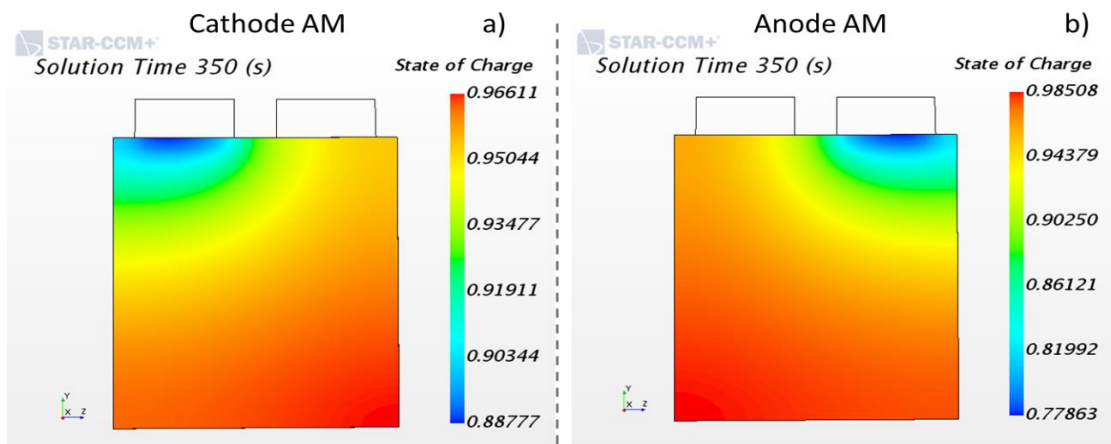


Figure 3.13 - State of Charge distribution over the (a) Cathode and (b) Anode active material

Figure 3.13 shows the state of charge evolution on the cathode (a) and anode (b) active material. It is well evident that its distribution is not uniform, but a gradient over the volume is present. In particular, it can be seen that lower values are obtained near to the tabs, meaning that in these points the cell discharges faster.

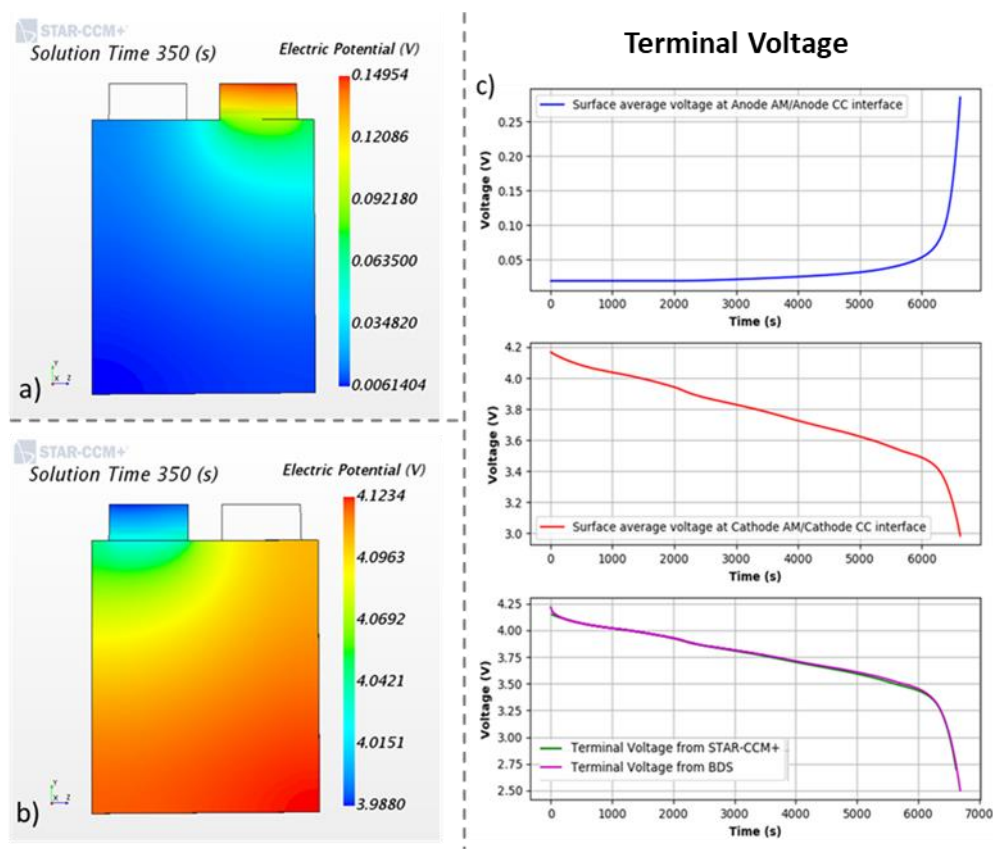


Figure 3.14 - Electric Potential in (a) Anode current collector, (b) Cathode current collector; (c) Terminal voltage simulation and comparison with measurements

Figures 3.14-a and 3.14-b provide information about the electric potential distribution respectively on the cathode and anode current collectors at one fixed time instant. Moreover, the time evolution of the voltage has been monitored over the time on one point of the anode and the cathode tabs (Figure 3.14-c, plots 1 and 2). The difference between the two curves provides the terminal voltage of the battery cell, $v(t)$, (Figure 3.14-c, plot 3), which is a differential voltage, as already explained in the previous sections. The obtained result (green curve) is comparable with the measurements (magenta curve).

As further check, the behaviour of the cell during the relaxation time (i.e. no electric current load applied) has been analysed. When the load current goes to zero, the drop voltage on the cell internal resistance becomes null and consequently there is a recover of the terminal voltage, which reaches the actual value of the open circuit voltage. At the same time, the state of charge must become uniform over the whole volume of active material. Results, shown in Figure 3.15 are in agreement with the expected behaviour.

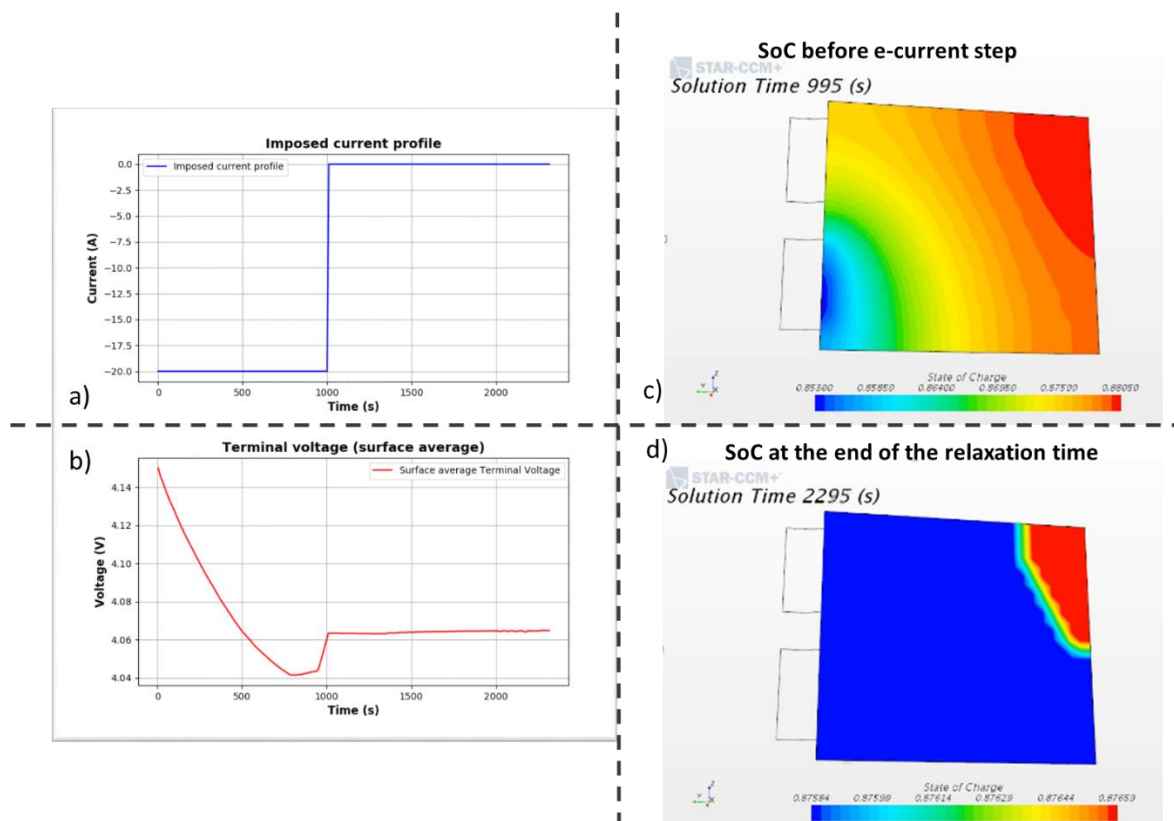


Figure 3.15 - Relaxation time simulation: a) imposed electric current step; b) terminal voltage recovering; c) State of charge before e-current step; d) State of charge at the end of the relaxation time

3.3.7 Modelling of the complete cell

After the validation of the single-layer cell for different load currents, the model has been extended to the complete cell, made of 41 pairs of positive and negative electrodes working in parallel. Following the approach described in Section 3.3.5, resistance and capacity of a single-layer cell have been linked with the ones of a real cell, whose values are known from the electrical characterization analysed in Chapter 2.

$$R_{\text{tot}} = \frac{R_{\text{single layer}}}{N_{\text{layers}}} \quad (3.32)$$

$$Q_{\text{tot}} = N_{\text{layers}} Q_{\text{single layer}} \quad (3.33)$$

The same has been done for the geometrical parameters:

- Thickness:

$$l_{\text{AM}}^{\text{tot}} = l_{\text{AM}}^{\text{single layer}} \quad (3.34)$$

- Section Area:

$$A_{\text{AM}}^{\text{tot}} = N_{\text{layers}} A_{\text{AM}}^{\text{single layer}} \quad (3.35)$$

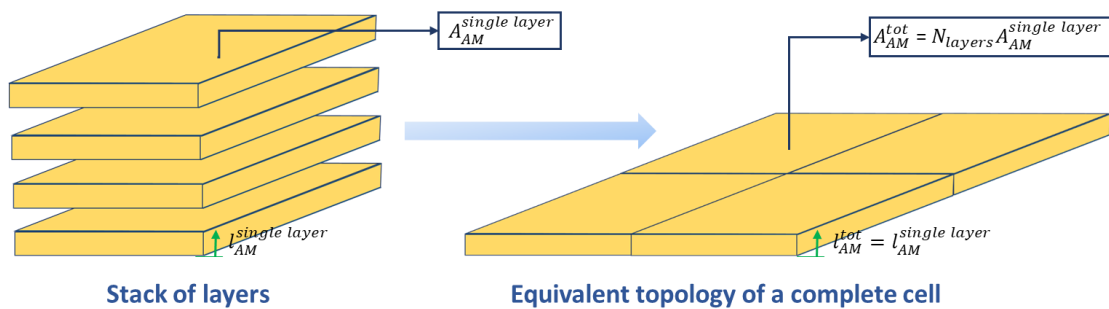


Figure 3.16 - Geometrical parameters of a complete cell

Finally, Equations (3.29), (3.30) and (3.31) have been readapted making use of the above equations.

$$\begin{aligned}
\text{DoD}_{\text{tot}}[k+1] &= \text{DoD}[k] + \frac{\Delta t}{Q_{\text{tot}}} J_x[k] A_{\text{AM}}^{\text{tot}} = \text{DoD}[k] + \frac{\Delta t}{Q_{\text{tot}}} J_x[k] A_{\text{AM}}^{\text{layer}} N_{\text{layers}} \\
&= \text{DoD}[k] + \frac{\Delta t}{\frac{Q_{\text{tot}}}{N_{\text{layers}}}} J_x[k] A_{\text{AM}}^{\text{layer}}
\end{aligned} \tag{3.36}$$

$$\text{SoC}_{\text{tot}}[k] = 1 - \text{DoD}_{\text{tot}}[k] \tag{3.37}$$

$$\sigma_{\text{A,C AM}}^{\text{tot}} = \frac{1}{R_{\text{p,tot}}^{\text{A,C}}} \frac{I_{\text{AM}}^{\text{tot}}}{A_{\text{AM}}^{\text{tot}}} = \frac{1}{R_{\text{p,tot}}^{\text{A,C}}} \frac{I_{\text{AM}}^{\text{tot}}}{A_{\text{AM}}^{\text{layer}} N_{\text{layers}}} = \frac{1}{N_{\text{layers}} R_{\text{p,tot}}^{\text{A,C}}} \frac{I_{\text{AM}}^{\text{tot}}}{A_{\text{AM}}^{\text{layer}}} \tag{3.38}$$

On the other hand, the imposition of the electrical specifications (Open Circuit Voltage and zero-voltage profiles) requires the definition of the interfaces between each couple of active material layer and separator. Since in this case a huge number of layers is involved, the procedure has been automated through the creation of Java Macros. In particular, interfaces can be manually created for a single-layer cell while the recording of the main steps is enabled. In this way, Siemens STAR-CCM+ translates the actions from the workspace into meaningful Java code. Then, the produced Java file can be edited in a text editor, by introducing simple for-loops, which cycle on all the layers of interest. Finally, the new obtained Java file can be run in order to create all the needed interfaces automatically.

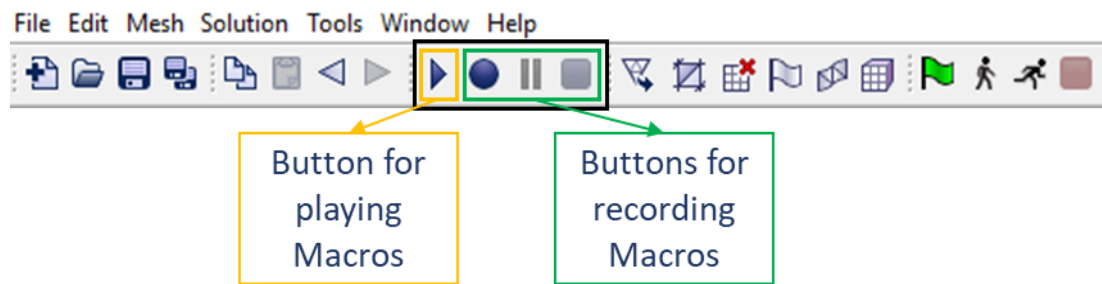


Figure 3.17 - Siemens STAR-CCM+ for macros recording and playing

Java macros have been also used in order to create contacts among tabs of the stacked single-layer cells. Indeed, when the geometry is imported, among them there is an empty space

that is not present in reality. This step is of crucial importance for the link of the single-pair-electrodes cells, which otherwise would behave as independent cells when loads are applied.

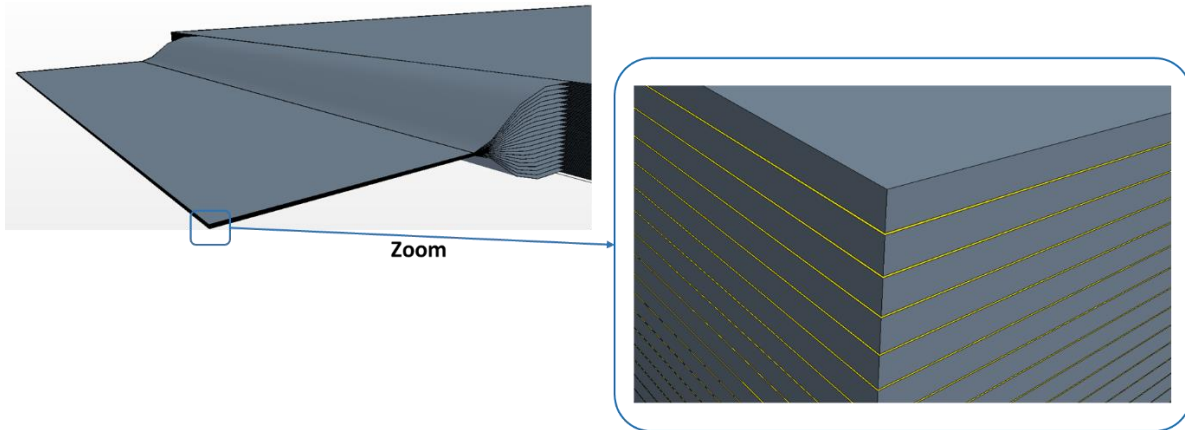


Figure 3.18 - Contacts creation among tabs: contact surface highlighted in yellow

Moreover, the way in which the layers are stacked, introduces another issue in the user-equations for the depth of discharge. Indeed, in the complete cell, each foil of current collector (either copper or aluminium), must be enclosed between two layers of active material belonging to the same species (respectively anode and cathode). As consequence, in each pair of layers around the same foil, the electric current density vector field has opposite direction.

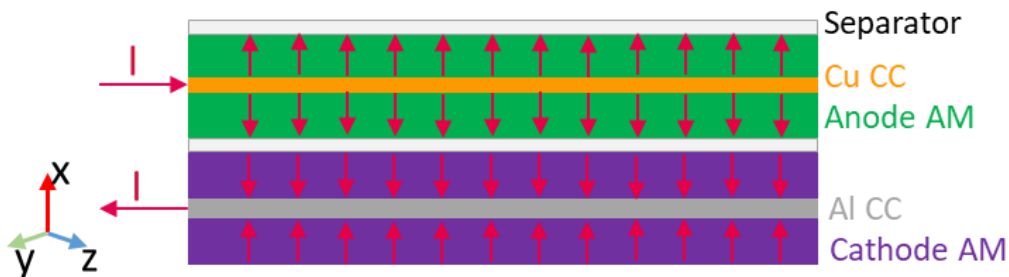


Figure 3.19 - Electric current density path in the active material (complete cell) during discharge

Referring to the laboratory reference system, with respect to which equations are written, in some substrates, the x-component of the electric current density, J_x , used for the definition of the depth of discharge, has negative sign. This means that, if Equation (3.36) is used, the computed depth of discharge would reduce over the time (as if the cell was charging), even if the cell is discharging. Thus, in order to solve the problem, both the cathode and anode regions

have been split in two more sub-regions. The active material layers belonging to the same sub-region, are characterized by the same direction of the electric current density with respect to the laboratory reference system. For the computation of the depth of discharge, two different equations have been associated to each kind of sub-regions, in order to obtain the correct behaviour of this variable as long as the discharge proceeds.

- J_x in the same direction of the x-axis:

$$\text{DoD}_{\text{tot}}[k + 1] = \text{DoD}[k] + \frac{\Delta t}{\frac{Q_{\text{tot}}}{N_{\text{layers}}}} J_x[k] A_{\text{AM}}^{\text{layer}} \quad (3.39)$$

- J_x in opposite direction of the x-axis:

$$\text{DoD}_{\text{tot}}[k + 1] = \text{DoD}[k] - \frac{\Delta t}{\frac{Q_{\text{tot}}}{N_{\text{layers}}}} J_x[k] A_{\text{AM}}^{\text{layer}} \quad (3.40)$$

3.3.8 Model validation: controlled temperature constant-e-current discharge

To validate the model, a simulation has been set up in order to test the electro-thermal behaviour of the battery cell when discharged with a constant electric current in controlled temperature conditions (20°C). In particular, a 4C-rate discharge (electric current equal to 160A) has been simulated and results have been compared with data coming from measurements discussed in Section 2.1.3. Electric current and thermal conditions at the boundaries have been imposed as shown in Figure 3.20:

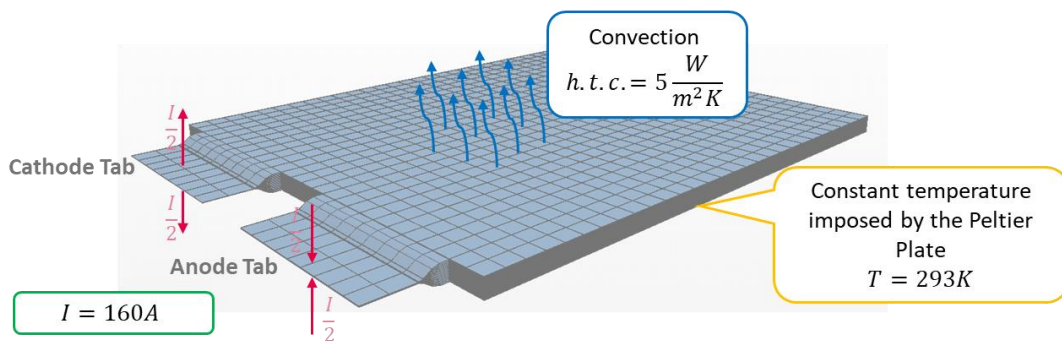


Figure 3.20 - Imposed thermal boundaries and current conditions

The solution has been monitored through scalar and vector scenes. Moreover, the temperature evolution over the time has been recorded in three points on the cell stack and

results have been compared with data measured from the thermocouples during the real test. Two more point probes have been introduced at the tabs in order to get information about the differential terminal voltage.

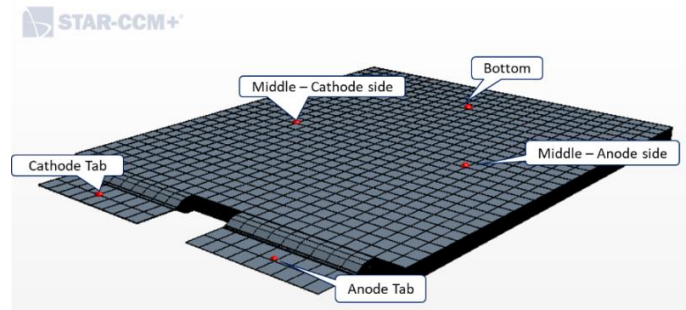


Figure 3.21 - Point probes position

Electric current density

Figure 3.22 shows the electric current density distribution on the cathode (a) and anode (b) current collectors. As expected, due to their geometry, higher densities are obtained near to the tabs roots. Moreover, as already noticed in case of the single-layer cell electrical simulation, the vector field is parallel to the yz plane of the laboratory reference system, while no relevant contributions are present in the transversal direction. The distribution remains almost unchanged over the time, since the input electric current applied at the tabs is kept constant.

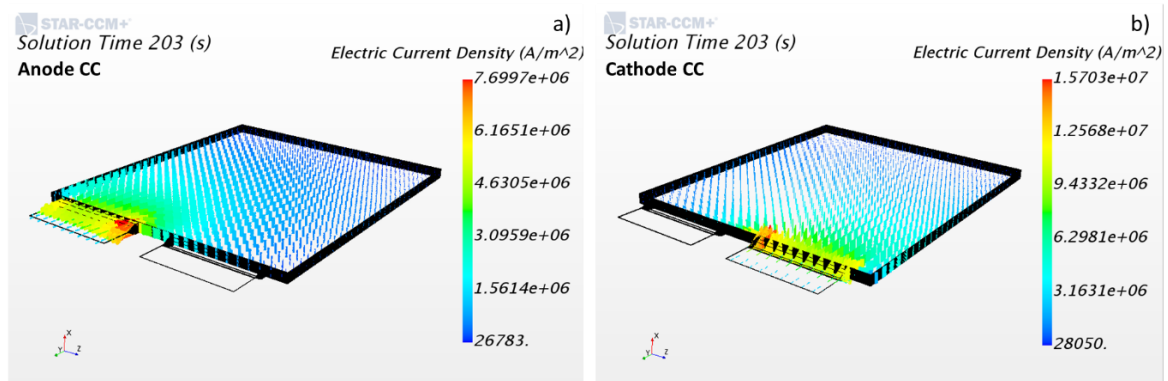


Figure 3.22 - Electric current distribution in the (a) cathode and (b) anode current collectors

State of Charge

Figure 3.23 shows the distribution of the absolute state of charge scalar function over the cathode active material at a fixed time instant. As already noticed in the single-layer cell case, the points near to the tabs discharge faster.

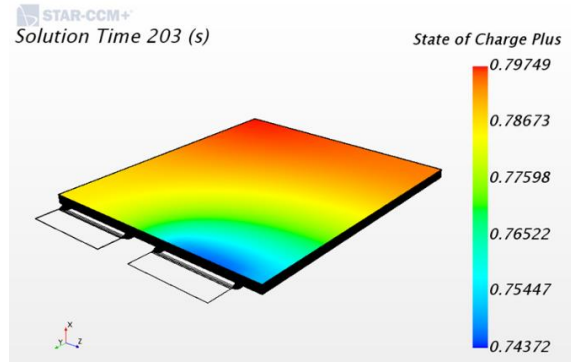


Figure 3.23 - Absolute state of charge distribution on the cathode active material at $t = 203$ s

Fixing the minimum and maximum values of the diplayer bar respectively to 0 and 1, it is possible to better analyze the time-variation of the absolute and relative state of charge. As expected, the relative state of charge decreases faster and it goes to zero at the end of the simulation (the simulation is stopped at 400s, when the terminal voltage reaches 2.5V). Instead, the absolute state of charge is still around 0.58 when the end condition is reached.

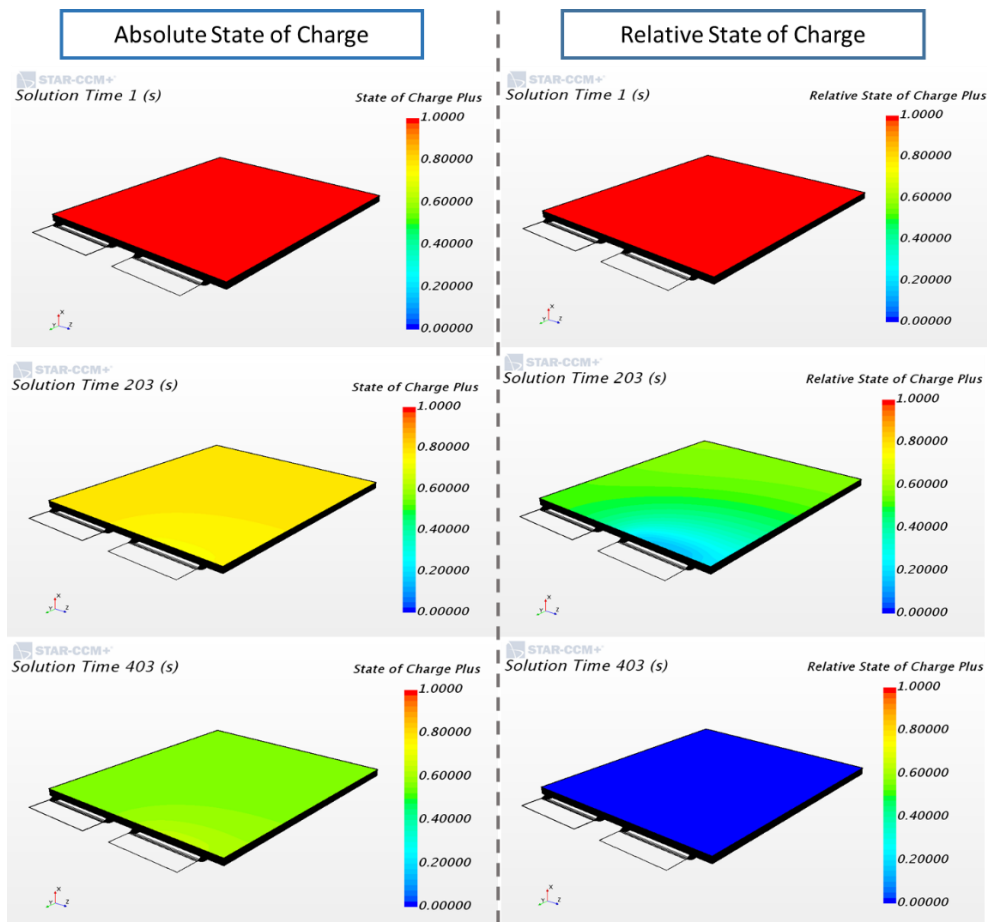


Figure 3.24 – Comparison between the time evolution of the absolute and relative state of charge

Electric potential

Figures 3.25-a and 3.25-b show the electric potential distribution over the anode and cathode current collectors at a fixed time instant. Through two point probes, the solution has been recorded at the anode and cathode tabs. The first two plots of Figure 3.25-c depict the obtained simulated voltage (referred to ground) in the two points. The terminal voltage has been evaluated as difference between the two and compared with the 4C-rate discharge curve coming from measurements. A good fitting is reached between measurements and simulations; thus the model can be considered validated from an electrical point of view.

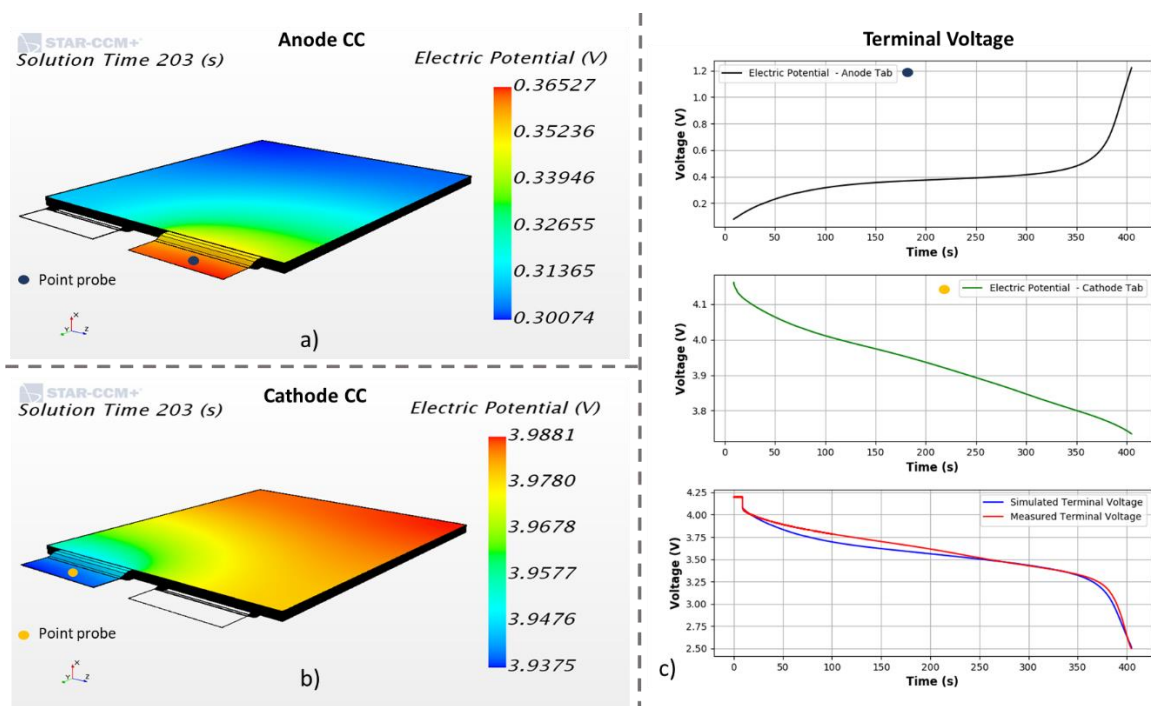


Figure 3.25 - Electric potential distribution in the (a) anode and (b) cathode current collectors; (c) Simulated terminal voltage

Temperature

Figure 3.26 shows the evolution of the temperature scalar field considering four different time instants from the beginning until the end of the simulation. Only a view of the upper part of the battery cell is reported, since the underside, in contact with the Peltier Plate, has a fixed imposed temperature profile. As confirmed from the measurements, higher temperatures are reached on the side of the cathode tab.

Making use of three point-probes, temperature has been monitored in three different points (shown in Figure 3.21) and compared with data collected during the real test. Results, reported in Figure 3.27, clearly show that the trend of the simulated and measured curves is the same. The existing difference of a couple of degrees may depend on the fact that in simulation the external pouch is not modelled. Indeed, its presence would reduce the measured temperature on the external surface.

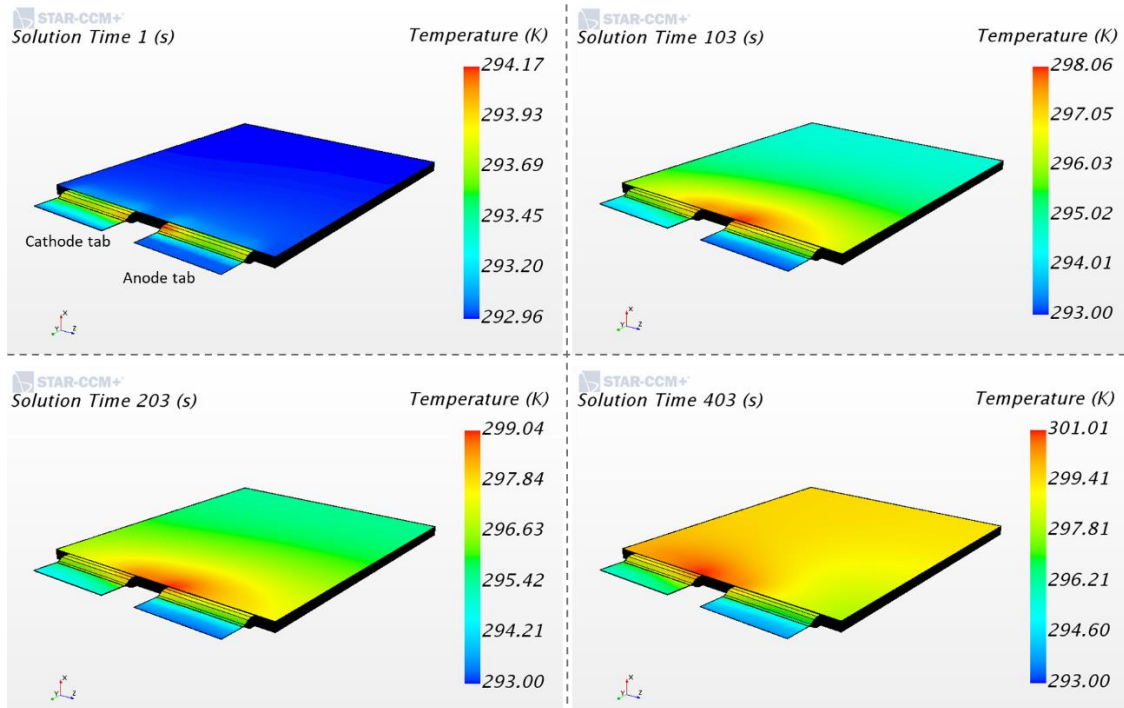


Figure 3.26 - Temperature distribution

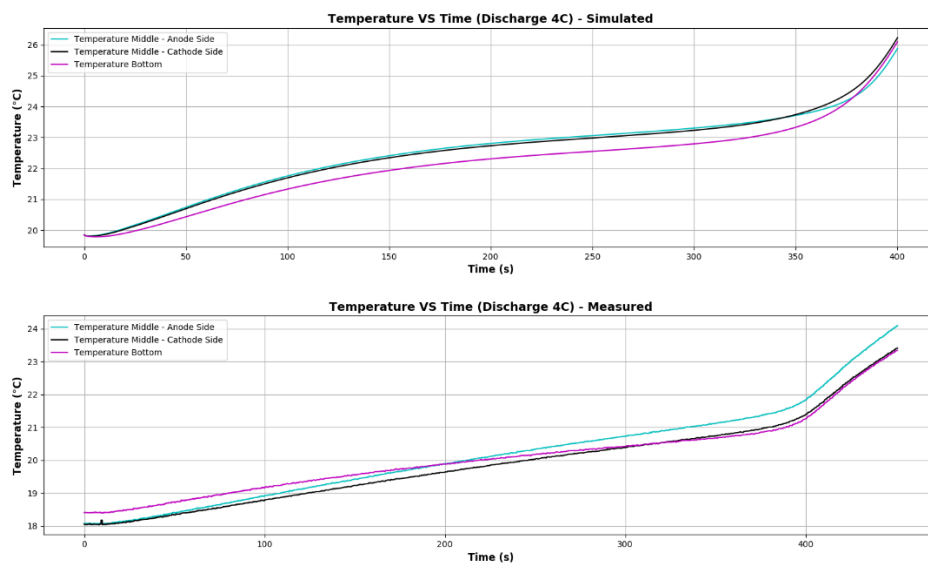


Figure 3.27 - Simulated VS Measured temperatures

CHAPTER 4

4. Nail Penetration Test

4.1 Regulations and Motivations

Safety requirements that electric vehicles must respect while in use and after a crash event are introduced in the Global Technical Regulation on Electric Vehicle Safety (ECE/TRANS/180/Add.20). As far as the thermal propagation is concerned, the Statement 23A.1 declares as follows:

“In order to ensure the overall safety of vehicles equipped with a REESS containing flammable electrolyte, the vehicle occupants should not be exposed to hazardous environment resulting from a thermal propagation (which is triggered by a single cell thermal runaway due to an internal short circuit).”

In order to test the thermal propagation, the regulation prescribes three different initiation methods able to trigger the thermal runaway of a single cell, which are the heating, the nail penetration and the overcharge. Then, the thermal runaway can be detected if at least two of the following conditions occur [4]:

- The measured voltage of the initiation cell drops.
- The measured temperature exceeds the maximum operating temperature defined by the manufacturer.
- $\frac{dT}{dt} \geq 1^{\circ}\frac{C}{s}$.

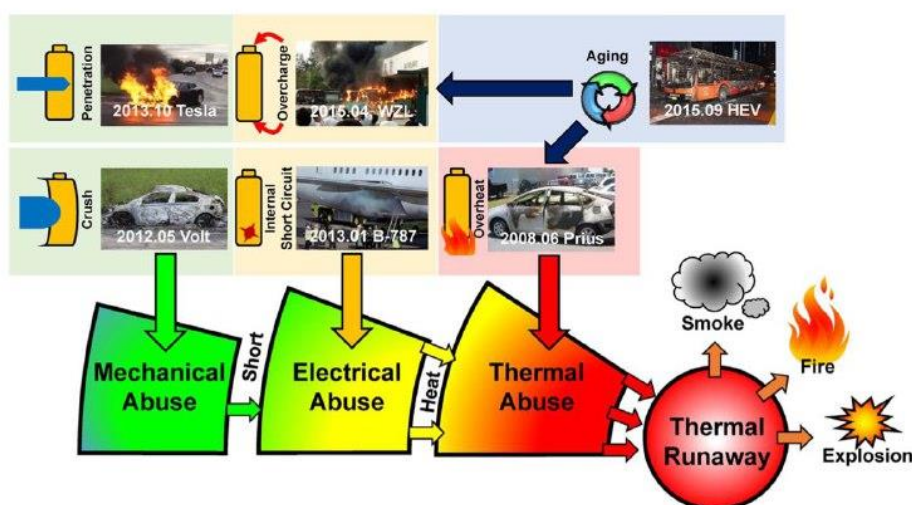


Figure 4.1 - Accidents related with lithium-ion battery failure, and correlated abuse conditions [1]

When nail penetration is chosen as initiation method, mechanical destruction of the internal layers and electrical internal short circuit occur simultaneously, resulting in a severe abuse condition. Indeed, during the penetration, high-level current flows through the cell, causing heat generation according to the Joule's law. Consequently, the temperature of the cell rises by absorbing the heat generated by the short circuit, until the cell is fully discharged. If, at the end of the short-circuit-induced discharge the temperature is below the critical value provided by the manufacturer, no further thermal runaway will be triggered [31].

However, even if the nail penetration test has the potential to be an extremely useful risk assessment method, it presents a low level of reproducibility and predictability, due to the difficulty of controlling the key parameters, as the shorting resistance. Moreover, the experimental observations during the tests provide little insight into the fundamental mechanism, such as the heating mode and the electro-thermal coupling [28] [29]. These issues justify the reason why a simulation model should be developed: indeed, this tool could provide a way to easily investigate the impact that different parameters may have on the test results.

4.2 Nail penetration tests description

In order to validate the goodness of the realised FEM electro-thermal model in predicting the cell behaviour also in abuse conditions, as nail penetration, a comparison with data coming from real measurements should be done. In the following a description of the performed nail penetration tests is provided, giving an insight on the used shape of the nail, on the test settings and on the main obtained results in terms of the measured terminal voltage and the temperature distribution over the battery-cell.

4.2.1 Used nail

The nail employed during tests is made of stainless steel and is characterized by a cross section. The adopted shape represents an innovative alternative to the common full-volume cylindrical nails for two main reasons. First, the contact resistance between nail and internal layers is reduced. This is an important point for the predictability and reproducibility of the test, since the contact resistance usually represents an unknown parameter. Second, the sharpness of its edges allows a proper cutting of the layers and especially of the separator, which otherwise could simply bend without breaking and overlap to the nail and the current collectors, creating an insulating barrier which prevents from the short circuit.

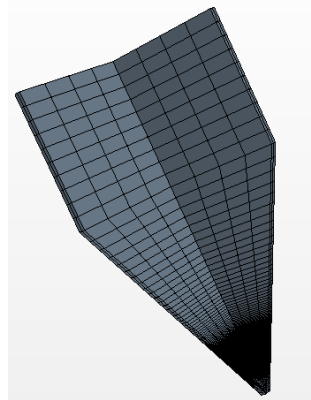


Figure 4.2 - Used cross-section nail

Table 4.1 describes the main features of the used nail in terms of geometry and employed material, which are in agreement with the prescriptions provided by the Technical Regulation (UN GTR No.20). Moreover, the penetration speed is also reported.

	Used Nail	Regulation (UN GTR)
Material	Steel	Steel
Thickness	1 mm	No prescriptions
Maximum Diameter	40 mm	$\geq 3\text{mm}$
Tip Angle	30°	[20° ÷ 60°]
Speed	1 mm/s	[0.1 ÷ 10] mm/s

Table 4.1 - Main features of the used nail

Nail Material Properties	
Density	8055 kg/m ³
Electrical Conductivity	1400000 S/m
Thermal Conductivity	480 J/kgK
Specific Heat	15.1 W/mK

Table 4.2 - Nail material properties

4.2.2 Test settings

The tests have been carried out making use of a hydraulic press, needed for controlling the movement of the nail. The battery cell has been positioned on a wood plate, employed to protect the press surface during the test. On top of the cell, a steel plate has been fixed through screws, in order to simulate the same pressure conditions acting on a cell when it is inserted in

a complete module. The presence of these two plates must be taken into account during the modelling, since, from a thermal point of view, the first one acts as an insulator, while the second one represents a thermal mass. On the steel plate, a cross section hole has been created to allow the entrance of the nail, besides smaller circular holes, useful for the positioning of the thermocouples.

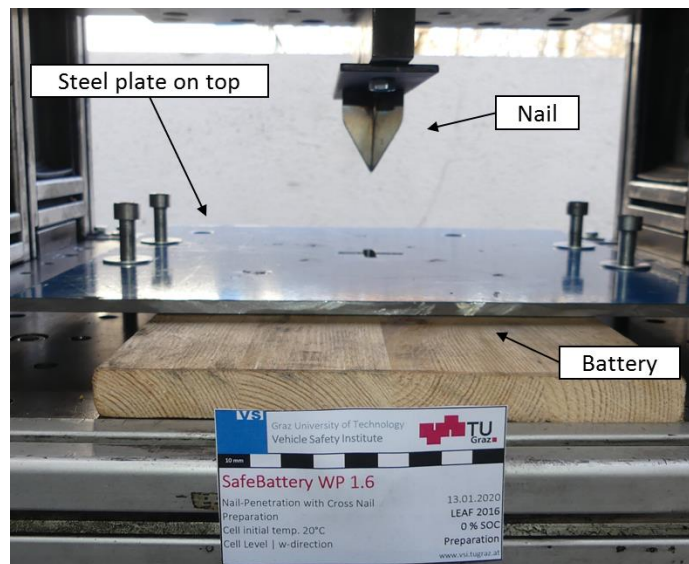


Figure 4.3 - Positioning of the battery cell in the hydraulic press

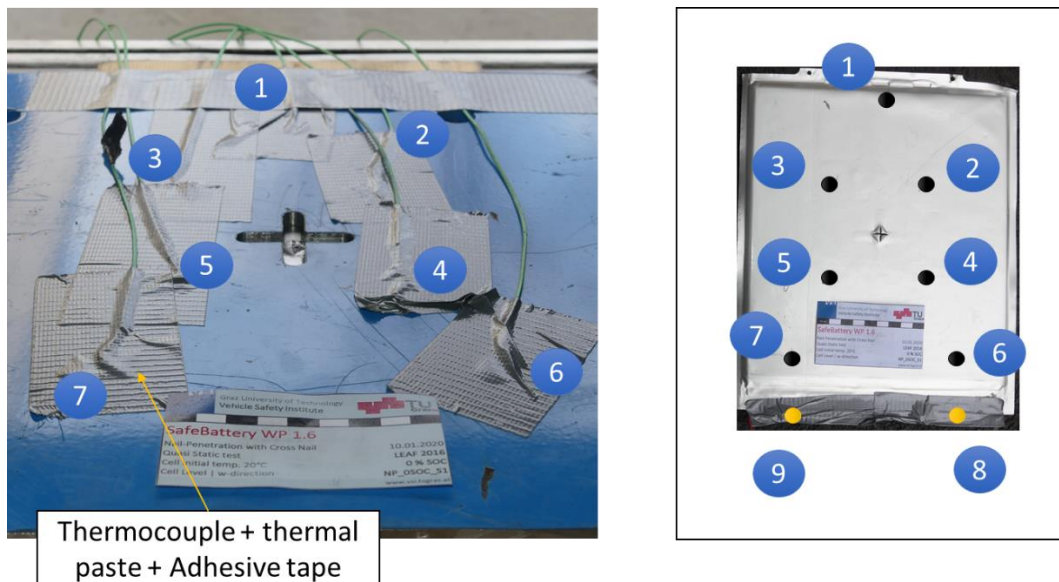


Figure 4.4 - Thermocouples positioning

Nine thermocouples have been positioned on the cell stack and on the tabs, as depicted Figure 4.4. They have been fixed making use of a thermal paste, which allows to improve the thermal contact especially on the pouch. One more thermocouple has been used to monitor the environment temperature. No thermocouples were put directly on the cross-section hole, near to the penetration area, since the measure would be affected from the higher temperature of the vented gas. At the tabs, the terminal voltage has been also measured.

The nail penetration test has been conducted on cells with different level of state of charge. In particular, 0%, 30%, 75% and 100% SoC were considered. For each state of charge level, the test has been carried out on five different samples, in order to analyse its repeatability.

The optimal speed of the nail was chosen by performing some preliminary tests at 0% SoC. It was observed that, at higher speed, the nail was not able to properly cut the layers and consequently worse electrical contacts were established. On the other hand, according to the literature, low nail-speeds are responsible for higher electric-current development and higher temperature rise [29]. For this reason, a speed of 1mm/s has been chosen. In this way, the cell is completely penetrated in 8 seconds (very small transient). After that, the nail has been left inside for 10 minutes and then pulled out.

4.2.3 Test results

In the following, results on tests carried out on cells at 100% state of charge level are briefly resumed. These data are used for the validation of the FEM electro-thermal model.

Terminal Voltage

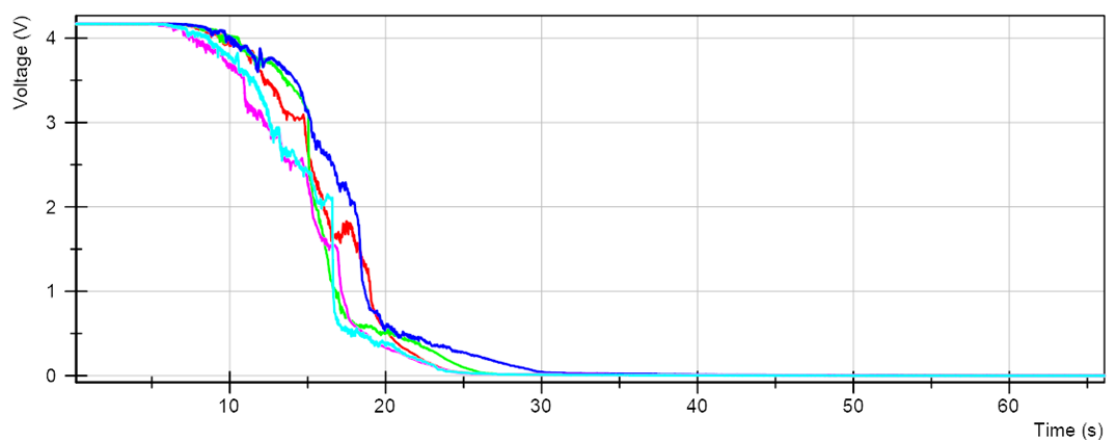


Figure 4.5 - Measured terminal voltage at the tabs

Figure 4.5 shows the trend of the terminal voltage at the cell tabs for the five samples at 100% SoC. This means that in the first time instants, when the nail is not in contact with the battery, the measured terminal voltage is equal to 4.2V. At the time $t = 14\text{s}$, the nail has completely penetrated the cell. Then a deep discharge until zero voltage occurs in almost 15s. As the five curves, corresponding to the five different samples have a comparable behaviour in time, a good repeatability of the test is assured.

Temperature

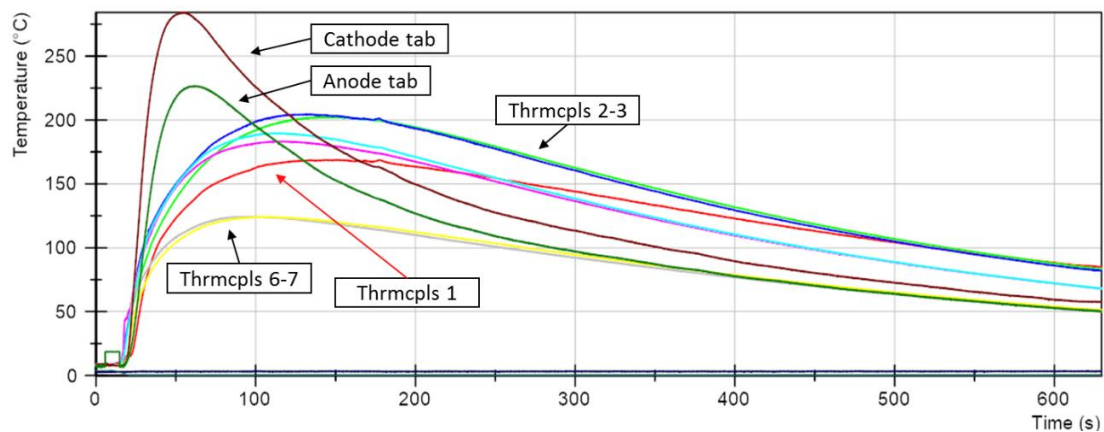


Figure 4.6 - Measured temperatures (100% state of charge)

Figure 4.6 shows the temperature evolution over the time in seven different points of the cell stack and on the tabs, monitored using thermocouples (Figure 4.4), for a single sample at 100% state of charge. On the cell stack, higher temperatures are registered by thermocouples 2, 3, 4 and 5, which surrounds the area where penetration occurs. The highest peaks are obtained at the tabs, where temperatures reach values of 250-300°C. As already noticed in the nominal discharge conditions, the cathode tab becomes warmer than the anode tab.

Table 4.1 shows an overview of the maximum temperatures measured by the nine thermocouples put on the battery cell, for the five samples at 100% state of charge. In some cases thermocouples failure has been detected, due to the fire and the smoke developed during the tests. In these cases, results have been reconstructed considering data registered by adjacent thermocouples.

100% SOC	Sample 1	Sample 2	Sample 3	Sample 4	Sample 5
T1	168	149	105	125	122
T2-5	≈190	≈208	220	235	227
T6-7	124	126	156	180	172
T8	284	265	253	317	285
T9	226	239	222	270	255

Table 4.3 - Maximum temperatures (in °C) observed for each test at 100% SoC

4.3 Electro-thermal modelling of a nail-penetrated battery cell

Starting from the FEM electro-thermal model deeply described in Chapter 3, a simulation of the nail penetration test has been set-up. Along with the cell, the modelling of the nail and the employed steel plate put upside the battery is also required. The mesh has been refined in the area of the cell stack where the hole provoked by the nail is present, as high gradients are expected. Moreover, contact interfaces must be defined between the nail and the layers of the cell, besides new boundary thermal conditions.

4.3.1 Meshing of the components

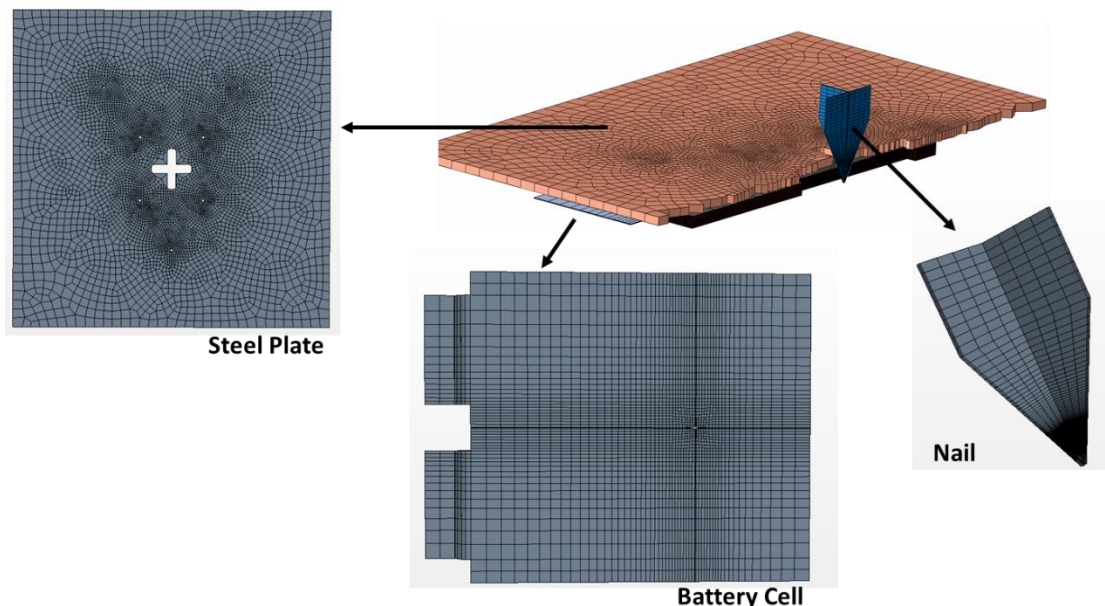


Figure 4.7 - Hexahedral mesh of the modelled components

Figure 4.7 gives a resuming of the modelled geometries and their meshing, carried out using hexahedral elements. Concerning the steel plate, a coarse mesh can be employed, since the introduction of this component is only needed for the simulation of a thermal mass, while electric solvers are not involved. Instead, a more refined mesh is required for the nail and the battery cell.

For a matter of accuracy and convergence of the solution, a conformal mesh, and so a perfect matching between the cell-faces of coincident parts, must be guaranteed. This is the reason why, the surface of the nail, which is in contact with the battery, has been meshed in order to have a perfect correspondence with the internal layers of the cell, as shown in Figure 4.8.

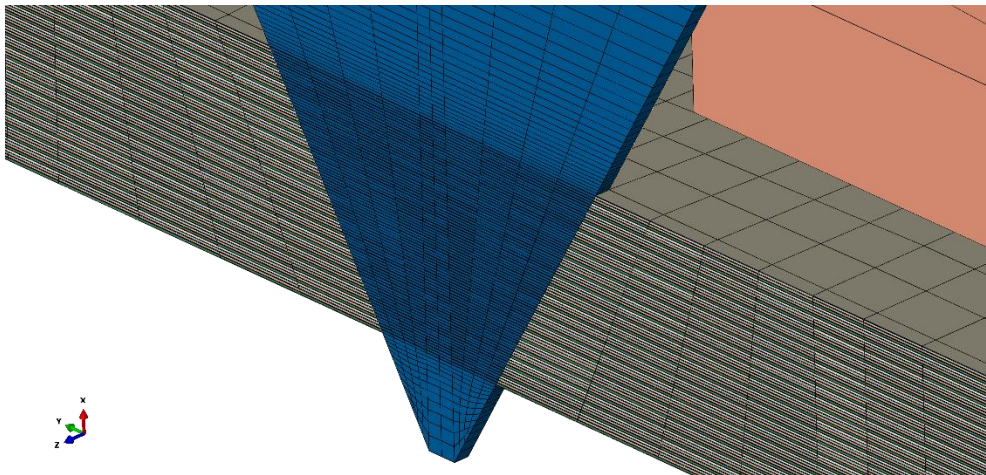


Figure 4.8 - Conformal mesh between battery cell and nail

4.3.2 *Contacts definition and boundary conditions*

When the nail is introduced, a definition of the contacts between nail and penetrated internal layers is required. For a sake of simplicity, contact interfaces have been created only between nail and current collectors. This hypothesis is supported by the literature [32], which assumes that in wet conditions with battery electrolyte, the nail/metal current collector has the smallest contact resistance. On the contrary, the nail/active material has the highest contact resistance, which is about three order of magnitude larger. Thus, as these resistances can be thought to be arranged in parallel, the e-currents at the nail/active material interface can be considered negligible. For this reason, the creation of the contact interface between nail and

active material can be avoided, which corresponds to assign an infinite value of contact resistance.

Furthermore, a contact interface between the top surface of the battery cell and the steel plate must be declared. In order to simulate the presence of the pouch, a contact thermal resistance [$\text{m}^2\text{K}/\text{W}$] has been assigned to the interface. In particular, considering that the thermal conductivity of the pouch, $\sigma_{thermal}$ is not exactly known but it can be supposed to be included in the range $[1,5] \frac{\text{W}}{\text{mK}}$, and that the thickness of the pouch is equal to 0.2 mm , the corresponding thermal resistance, computed as

$$R_{\text{thermal}} \left[\frac{\text{m}^2\text{K}}{\text{W}} \right] = \frac{l}{\sigma_{\text{thermal}}} \quad (4.1)$$

must fall in the range $[0.4 \cdot 10^{-4}, 2 \cdot 10^{-4}] \frac{\text{m}^2\text{K}}{\text{W}}$. In the final simulation a value of thermal resistance equal to $2 \cdot 10^{-4} \frac{\text{m}^2\text{K}}{\text{W}}$ has been imposed.

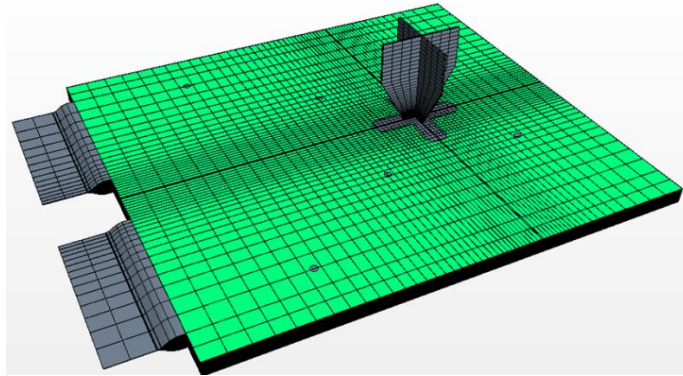


Figure 4.9 - Contact surface (highlighted in green) between battery cell and steel plate

Finally, boundary thermal conditions have been set-up. As, during the test a blower been used for protection purposes against smoke and fire, convective effects must be modelled. According to the literature, in case of forced convection in presence of air, gases and dry vapours, the heat transfer coefficient varies in the range $[10,1000] \frac{\text{W}}{\text{m}^2\text{K}}$. In the simulation, a value of $100 \frac{\text{W}}{\text{m}^2\text{K}}$ has been chosen. The imposed ambient temperature has been taken from measurements coming from the tests and fixed at 3°C . On the other hand, the bottom surface of the battery cell in contact with the wood, has been considered adiabatic.

CHAPTER 5

5. Simulation Results

In this Chapter the main results obtained from the simulation of the nail penetration test are discussed, making a comparison with information coming from the real measurements. Simulations consider a battery cell that is fully charged (100% SoC) when the penetration occurs.

5.1 Electric current

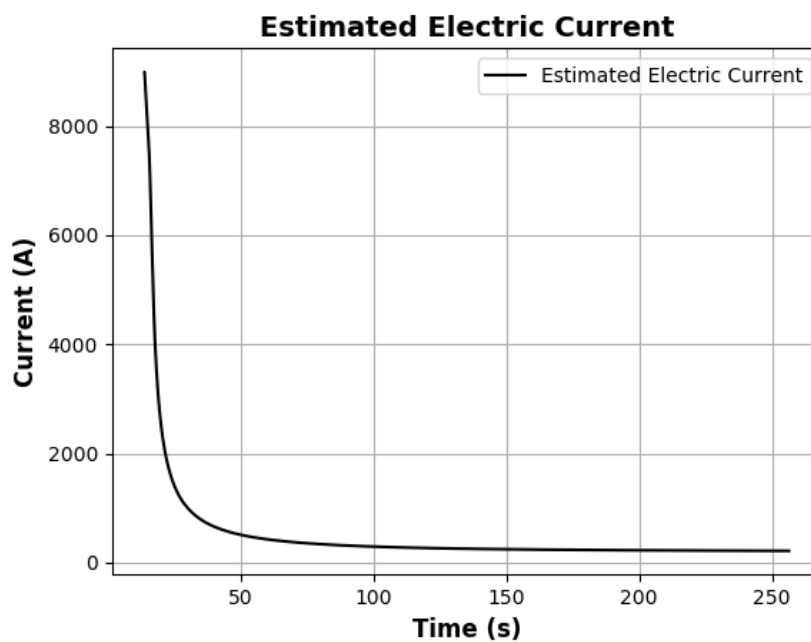


Figure 5.1 - Estimation of the electric current through the nail

In Figure 5.1 it is plotted the estimated total electric current on the battery-cell during the nail penetration process. In this case, it is not possible to make a direct comparison with the real discharge e-current supplied by the cell during the abuse, since there is no way to measure it when the real test is performed. However, the trend obtained in simulation is in agreement with what is supposed in literature [28] [29]. At the beginning, the internal short circuit is ohmically controlled, since the polarization resistance, mainly related to the electrochemical processes inside the cell and characterized by slower dynamics, is nearly zero. As long as the contribution of this resistance becomes more important, the internal short circuit is mitigated and the total electric current reduces. Besides the entity of the time constant τ_1 , governing the transient of

the internal polarization resistance (Equation 3.16), its trend and, consequently, the speed of decrease of the electric current is also dependent on the value chosen as upper bound of the η coefficient, used in the definition of the Relative State of Charge (Section 2.2.4). A value of $\eta_{max} = 8$, corresponding to $C_{Ah,l}^{lim} = 5Ah$, has been set up, which, in turns, allows to obtain a good fitting of the terminal voltage curve measured at the tabs as will be explained in Section 5.2.

Figure 5.2 shows the evolution of the polarization resistance during the time. The plot refers to an average made on the whole active material volume.

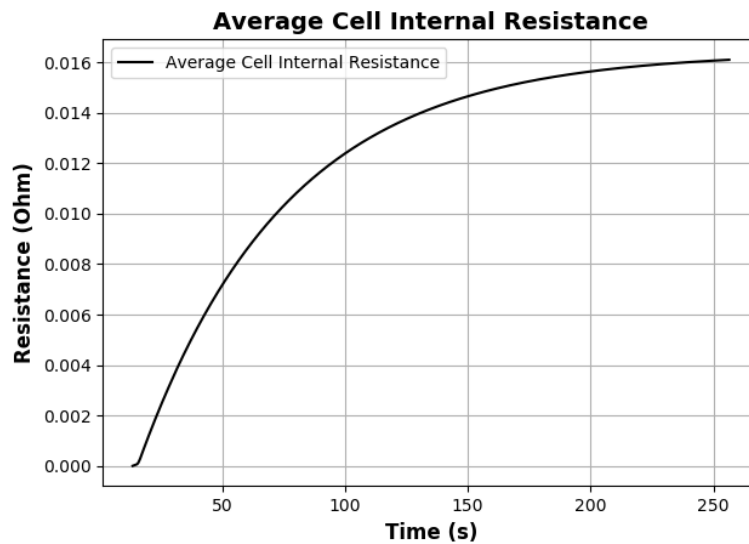


Figure 5.2 - Polarization Resistance (average)

Figure 5.3 shows how the electric current density is distributed in the current collectors when nail penetration occurs. At each time instant, the highest densities are obtained at the nail/current collectors interface. Indeed, this area corresponds to the point where the load is applied and consequently, similarly to the nominal case in which a load is attached to the tabs, the cell works in order to sustain the electric current at its ends. The distribution in time remains almost unchanged. Vector magnitude overall decreases as long as the internal resistance of the cell increases and the electric current through the nail is reduced.

As no external load is considered, no electric current exits the tabs. This does not mean that the electric current density in the tabs is equal to zero. Indeed, due to the conical nail shape, the shorting is more severe on the top layers (due to the bigger section of the nail and the consequent lower shorting resistance), resulting in a deeper voltage drop. Consequently, a potential

difference exists between the top and bottom layers, as shown in Figure 5.4 (Cathode current collectors), which causes a flow of current from the bottom to the top, closing on the tabs. For this reason, the electric current density in the tabs is not zero, (as instead happens for constant section nails), but a “butterfly” distribution can be observed, as depicted in Figure 5.3-c.

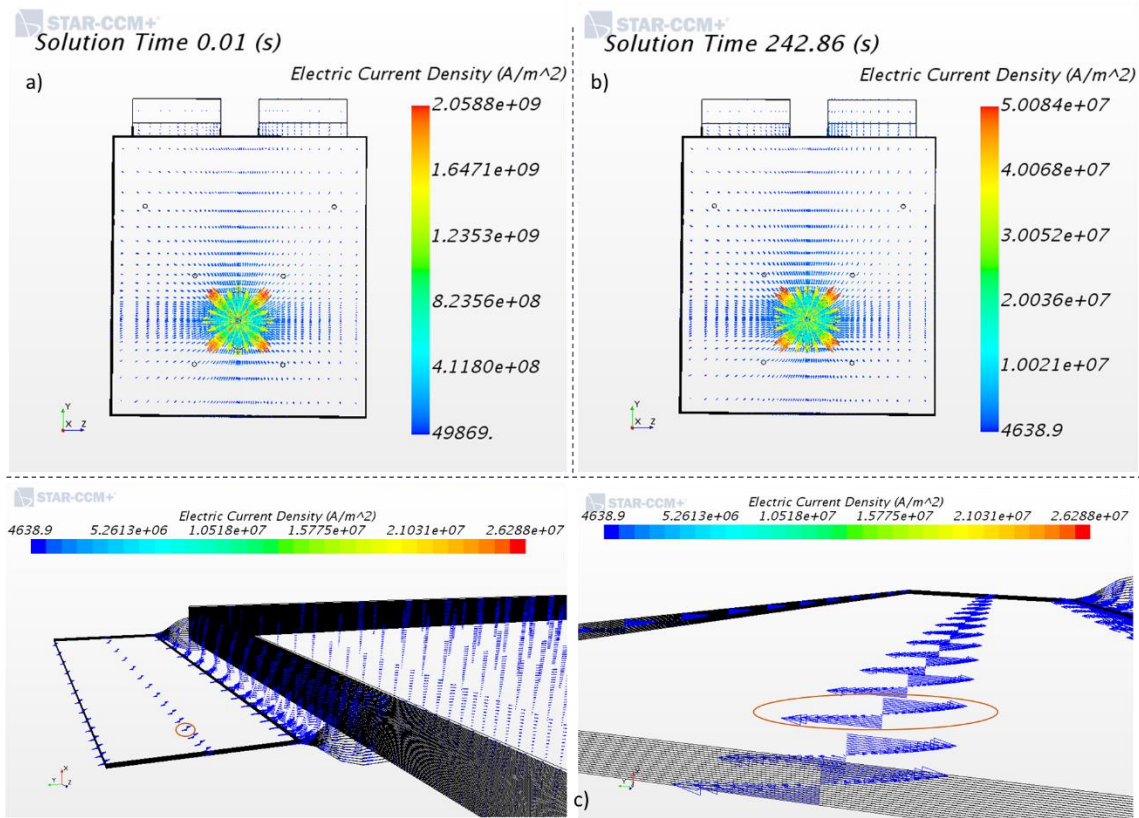


Figure 5.3 - Electric current density in the current collectors at the (a) beginning and (b) after 76s from the complete penetration of the cell. (c) Electric current density distribution at the tabs

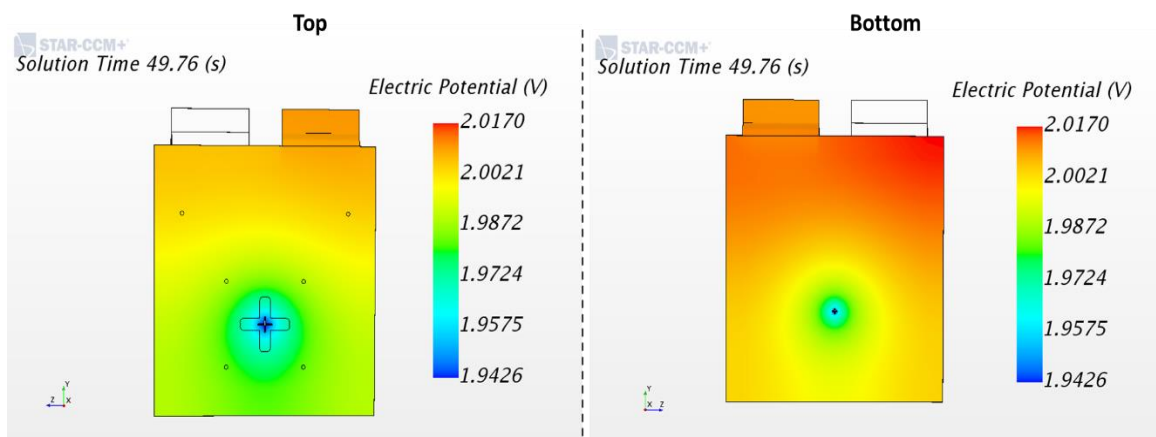


Figure 5.4 - Electric Potential Distribution on the Cathode Current Collectors

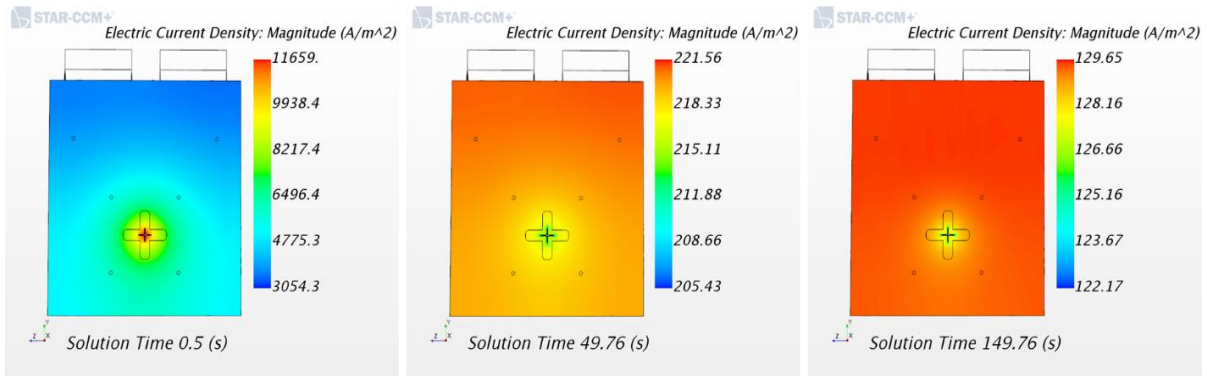


Figure 5.5 - Electric current density magnitude on the active material

Figures 5.5 reports the magnitude of the electric current density on the active material respectively in three different time instants. At the beginning of the abuse, the electric current is sustained by the elements near to the nail, which are discharging faster. Indeed, in the first seconds of simulation, the electric current density near to the tabs is almost one order of magnitude lower than the one around the nail. Then, as long as the discharge proceeds, the electric current density distribution becomes more uniform on the overall volume of active material.

Figure 5.6 shows the State of Charge distribution in the active material at a fixed time instant ($t = 150$ s). Around the nail, a faster reduction occurs due to the higher electric current densities involved. Moreover, it is possible to notice that the top layers are characterized by higher depths of discharge than the bottom ones. This result is in line with Figure 5.4 and confirms that, on the top layers, the severity of the short circuit is bigger due to the smaller values of the shorting resistance involved.

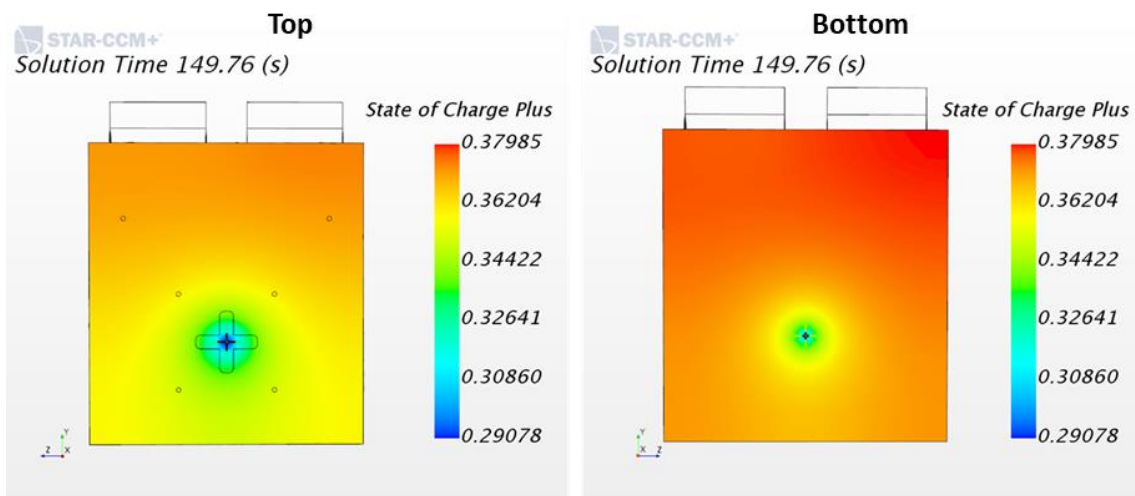


Figure 5.6 – State of charge on the active material

5.2 Electric Potential

In Figure 5.7 it is reported the trend of the simulated terminal voltage (green curve), evaluated as difference between the electric potentials at the tabs. The obtained curve completely falls in the stripe, built considering results coming from the five samples at 100% SoC. The simulated curve has been translated on the time axis of 14 s, which is the time employed by the nail to go down and stop. Indeed, the simulation does not consider this transient, but it is started with the nail stopped in its final position and all the layers already penetrated. In this time interval, it is expected that the contact resistance between nail and internal layers is not constant. In particular, it should decrease with the increase of the number of penetrated layers, as they can be considered arranged in parallel. Consequently, the terminal voltage reduces slowly starting from 4.2V. When the nail is stopped, a perfect electric contact is supposed between nail and current collectors, while no contact is considered between nail and electrodes. From this point on, the deep discharge begins, as depicted also by the simulated curve.

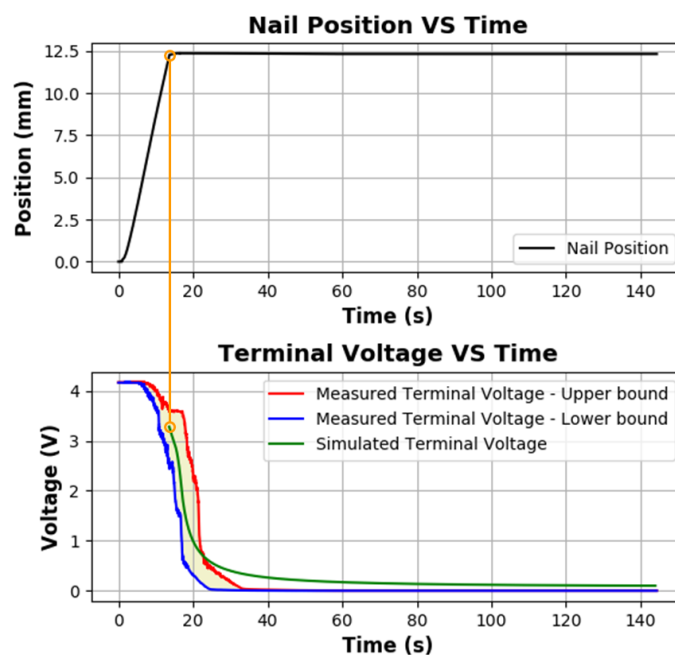


Figure 5.7 - Comparison between simulated and measured terminal voltage

Figure 5.8 provides an overview of the electric potential distribution over the anode and cathode current collectors and its evolution over the time. In both cases there is a gradient from the nail-hole to the tabs. In particular, the electric potential reduces moving from the nail to the tabs in the anode current collectors. The opposite happens in the cathode current collectors.

This is in agreement with the path of the electric current, considering that it enters the nail at the nail/cathode-current-collector interface and exists at the nail/anode-current-collector interface. It is worth highlighting that at each time instant, the potential difference between the corresponding points of the current-collectors near to the nail is almost zero due to the short circuit, as expected.

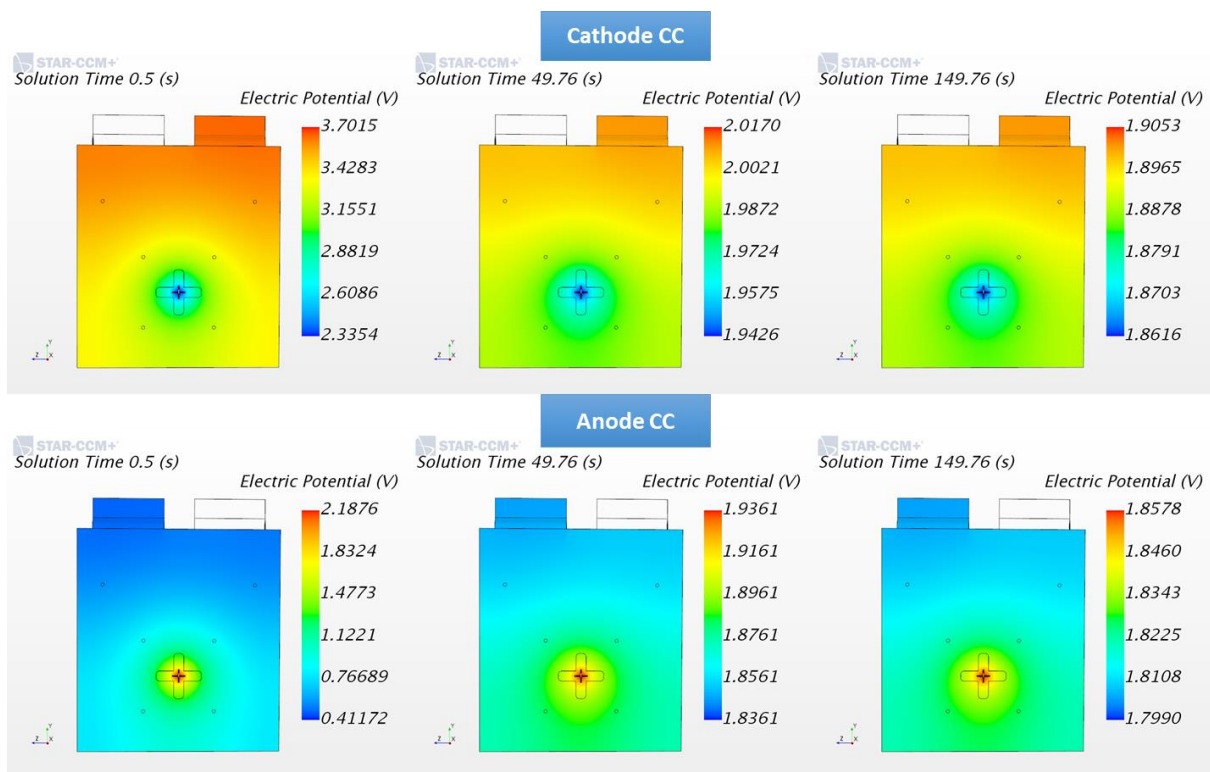


Figure 5.8 - Electric potential distribution in the current collectors

5.3 Temperature

Figures 5.9 and 5.10 give an insight on the distribution of the temperature on the top and bottom sides of the battery cell at different time instants. It is evident that higher temperatures are reached on the bottom part of the cell, which is in contact with the wood. On the other hand, on the upper part, lower temperatures are reached, due to the presence of the steel plate, which acts as thermal mass, and the effect of the convection forced by the blower.

At the beginning of the abuse the temperature fast increases around the nail, reaching values of hundreds of degrees (1500K are reached locally), while it is kept lower on the rest of the cell volume. A direct comparison with measurements is not possible, since no thermocouples could be installed too near to the nail. However, the immediate local temperature rise seems to be

confirmed by the presence of some sparkles during the first seconds of the real test, which may be related to the melting of the aluminium current collector foils (melting temperature of 933.47 K). As long as the simulation proceeds, the maximum temperature reached locally near to the nail reduces, while a global heating of the overall cell occurs. The temperature gradient, detected moving from the nail to the tabs, gradually reduces, until the temperature becomes almost uniform on the overall cell. Such behaviour can be understood considering the impact that the internal resistance has on the heating of the cell. At the beginning of the discharge, the internal resistance is simply given by the ohmic resistance of the current collectors, while the polarization resistance (with bigger time constant) is almost zero. In this scenario, the nail resistance can be considered bigger than the cell resistance and consequently the main contribution to the heat generation will be given by the localized ohmic heating from the nail. Instead, as long as the internal resistance of the whole cell increases on the whole cell, its contribution in the heat generation rises and a global heating is obtained [28].

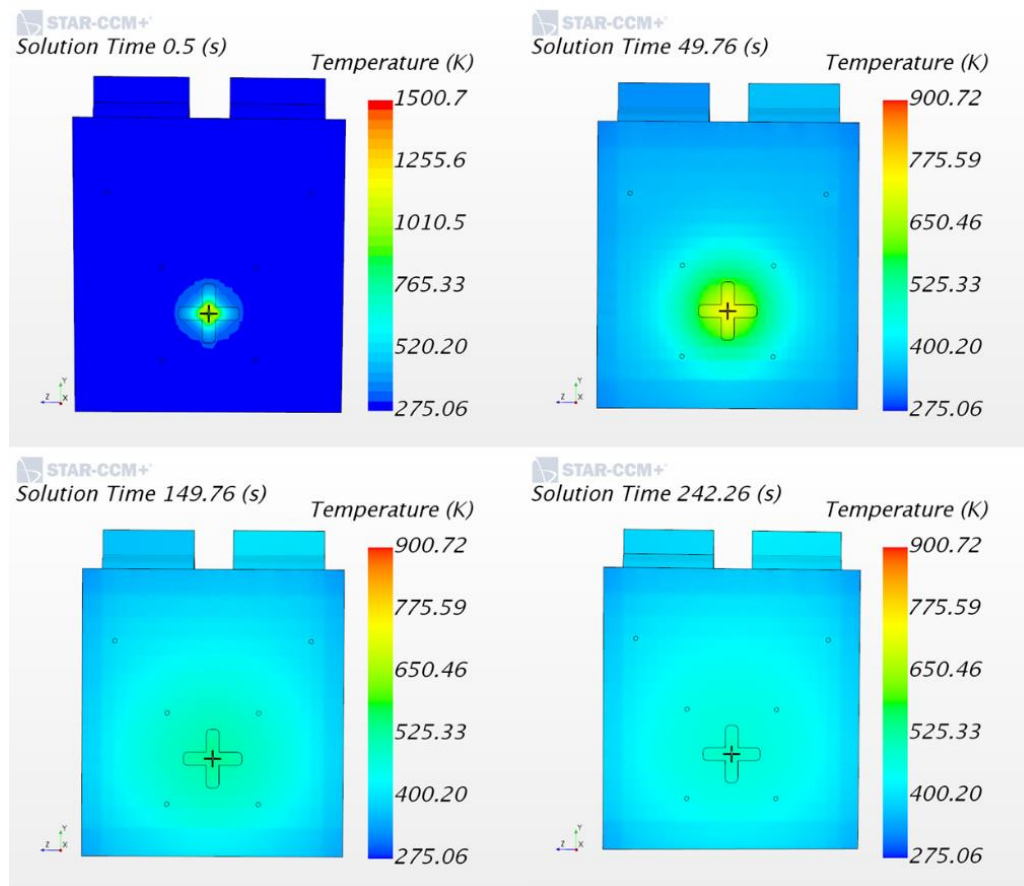


Figure 5.9 - temperature distribution on top side of the cell

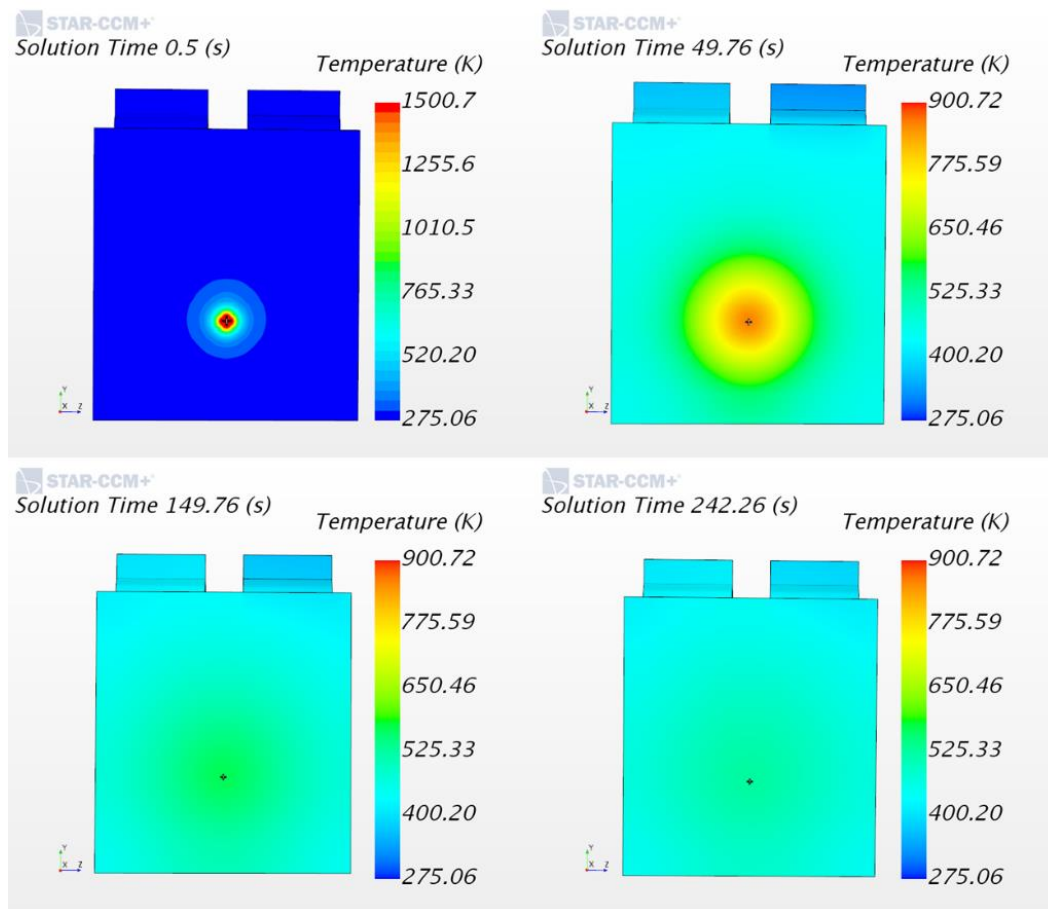


Figure 5.10 - temperature distribution on bottom side of the cell

In Figure 5.11, a comparison between the simulated and measured temperatures in seven points of the cell stack is reported. For each thermocouple, a stripe of values has been defined, considering the results obtained from measurements on five different samples at 100% SoC. A good matching is obtained for the four points surrounding the nail (points 2, 3, 4 and 5), as long as the rise time and the maximum value are considered. Satisfactory results are also obtained for thermocouple 1, put on the bottom of the cell. Some discrepancies, instead, exists between the simulated and measured curves in points 6 and 7. In particular, the simulated curves rise slower than the measured ones, while a matching is still guaranteed in terms of maximum temperature. Such difference may derive by the influence of side effects not taken into account in the modelling, as the gas venting and the boiling of the electrolyte, which may cause a faster temperature increase also far away from the nail, due to the heat transfer by convection.

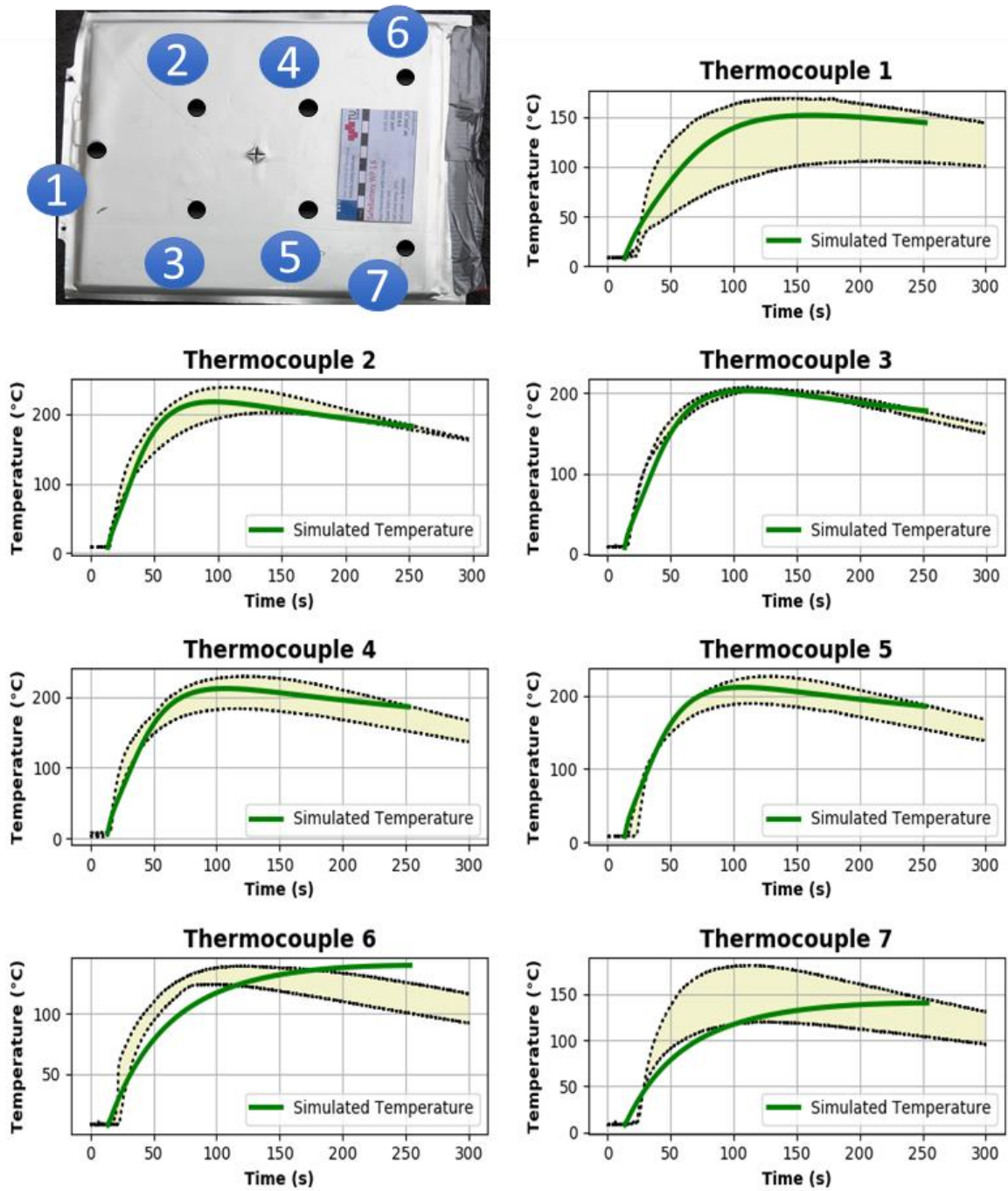


Figure 5.11 - Comparison between simulated and measured temperature at the tabs

6. Conclusions

In this work a FEM multi-physics model for an automotive Lithium-ion pouch battery cell has been developed. This investigation provides support, from a simulation point of view, for the understanding and evaluation of an internal short circuit caused by a nail penetration. In particular, it is able to estimate the voltage response of the tested battery cell and the temperature evolution over the time, with particular focus on the rise time and the maximum value reached during the abuse. Since temperature can trigger Thermal Runaway, this evaluation allows to predict the hazard level, according to the conditions prescribed by the Global Technical Regulation (GTR20) on Electric Vehicle Safety [4].

An extensive literature research has been performed, getting an overview on analytical models based on a detailed description of the electrochemical processes. The complexity of the analytical electrochemical models and the difficulties to measure the needed parameters, led to the proposed empirical model, through the set-up of an equivalent electric circuit. The main advantage of this new approach relies on the few number of parameters to be estimated, which results in a low computational complexity and, in turns, in low time-consuming tests.

The equivalent Electric Circuit Model (ECM) has been derived, exploiting information coming from constant-current discharging curves and electrochemical impedance spectroscopy. Such electrical measurements allowed to characterize the SoC-dependent equilibrium voltage curve and the cell internal impedance for every SoC. In this way, the heat generated can be evaluated simply making use of the Joule law, so that a complex modelling of the internal chemical reactions can be avoided. A first-order R-RC circuit has been calibrated for the fitting of the measurements. Once its main parameters have been regressed, the 1D-ECM has been used as starting point for the set-up of the FEM electro-thermal 3D modelling carried out into STAR-CCM+ environment. The discretization has been performed with a one-to-one correspondence between the elementary blocks coming from the battery-cell volume and the 1D-ECM lumped parameters model. In particular, the impedance of the 1D-ECM has been employed to model the electrical conductivity of the active material layers. Furthermore, the SoC-dependent voltage generator (equilibrium voltage curve) has been implemented through the declaration of boundary/interface voltage values.

Thermal properties of materials and layers have been assigned making use of data coming from literature [5] and direct tests. The correctness of thermal masses and thermal conductivities

is a crucial point for the reliability of the model and its validation, since they are used for the computation of the temperature distribution once the electric current in the cell, caused by the electric load, and the consequent heat generated by the Joule effect have been determined.

The modelling into STAR-CCM+ has been carried out following state-of-the-art methodology of simulation engineering, gradually moving from the characterization of a single element to the complete cell. First validations have been performed with results coming from constant-current discharge procedure in temperature-controlled conditions, then the model has been slightly modified to simulate the nail penetration test, performed with a cross section nail made of steel. The matching obtained between measurements and simulation results has confirmed the good capability of the model in predicting the terminal voltage response and the temperature distribution, also in abuse conditions.

However, the electro-thermal evolution of a Li-ion cell under nail penetration test is a complex phenomenon involving boiling electrolyte, gas venting and exothermal behaviour of materials.

The present work does not consider the effects related to the gas venting and the boiling of the electrolyte, which can cause heat transfer by convection and thus a faster temperature increase in points of the stack far away from the penetrated area and on the tabs. In future works, these effects could be taken into account by modelling the thermal parameters, as the thermal conductivity, the specific heat and the heat transfer coefficient through suitable laws depending on time and temperature. On the other hand, a user-defined heat source can be introduced in the characterization of the active material layers, in order to simulate the occurrence of the exothermic side reactions, which are triggered for temperatures above 150°C. Further improvements can be also obtained by explicitly including in simulation the presence of the pouch bag.

Moreover, since the nail penetration test can be seen as an extreme case of constant-resistance discharge procedure, a new set of measurements could be set-up with the purpose of testing the behaviour of the cell when discharged with a constant-resistance load. Such information may be useful to improve some features of the 1D-equivalent electric circuit model. Finally, in order to improve the robustness, a parametric study can be carried out, in order to examine the predicting capabilities of the model in different working conditions. For example, the effect of the distance of the penetration area from the tabs can be investigated, as well as the impact that the contact resistance between nail and internal layers has on the evolution of

the short circuit behaviour. Furthermore, comparisons with other tests using nails having different geometries and materials can be performed.

References

- [1] X. Feng, M. Ouyang, X. Liu, L. Lu, Y. Xia and X. He, "Thermal runaway mechanism of lithium ion battery for electric vehicles: A review," *Energy Storage Materials* , vol. 10, pp. 246-267, 2017.
- [2] X. Shan, F. Li, D. Wang and H. Cheng, "The smart era of electrochemical energy storage devices," *Energy Storage Material* , vol. 3, pp. 66-68, 2016.
- [3] G. Santos, "Road transport and CO2 emissions: What are the challenges," *Transport Policy* 59, pp. 71-74, 2017.
- [4] UNECE, Global Technical Regulation on the Electric Vehicle Safety (No.20), 2018.
- [5] L. Aiello, G. Kovachev, W. Sinz and C. Ellersdorfer, "In-situ measurement of orthotropic thermal-conductivity on pouch lithium-ion battery and determination of active material properties," 2020.
- [6] X. Zhang, W. Zhang and G. Lei, "A Review of Li-ion Battery Equivalent Circuit Models," *Transactions on electrical and electronic materials*, vol. 17, no. 6, pp. 311-316, 2016.
- [7] A. Dinger, M. Ripley, X. Mosquet, M. Rabi, D. Rizoulis, M. Russo and G. Sticher, "Challenges, Opportunities, and the Outlook to 2020," *Batteries for Electric Cars*, 2010.
- [8] G. L. Plett, Battery Management Systems, Norwood: Artech House, 2015.
- [9] B. V.S., Fundamentals of Electrochemistry, Inc., Hoboken, New Jersey: John Wiley & Sons, 2006.
- [10] P. Vyroubal and T. Kazda, "Equivalent circuit model parameters extraction for lithium ion batteries using electrochemical impedance spectroscopy," *Journal of Energy Storage*, vol. 15, pp. 23-31, 2018.
- [11] M.-C. Pang, Y. Hao, M. Marinescu, H. Wang, M. Chen and G. J. Offer, "Experimental and numerical analysis to identify the performance limiting mechanisms in solid-state lithium cells under pulse operating conditions," *Physical Chemistry Chemical Physics*, 2019.
- [12] D. J. Noelle, M. Wang, A. V. Le, Y. Shi and Y. Qiao, "Internal resistance and polarization dynamics of lithium-ion batteries upon internal shorting," *Applied Energy*, vol. 212, pp. 796-808, 2018.
- [13] N. L. Hamidah, F. M. Wang and G. Nugroho, "The understanding of solid electrolyte interface (SEI) formation and mechanism as the effect of fluoro-o-

- phenylenedimaleimide (F-MI) additive on lithium-ion battery,” *Surface and Interface Analysis*, pp. 345-352, 2018.
- [14] Q.-A. Huang, Y. Shen, Y. Huang, L. Zhang and J. Zhang, “Impedance Characteristics and Diagnoses of Automotive Lithium-Ion Batteries at 7.5% to 93.0% State of Charge,” *Electrochimica Acta*, vol. 219, pp. 751-765, 2016.
- [15] Q.-C. Zhuang, X.-Y. Qiu, S.-D. Xu, Y.-H. Qiang and S.-G. Sun, “Diagnosis of Electrochemical Impedance Spectroscopy in Lithium-Ion Batteries,” *Intechopen*, 2012.
- [16] *The SEI Layer Inside Lithium Batteries Explained (www.upsbatterycenter.com)*, 2018.
- [17] T. R. Jow, S. A. Delp, J. L. Allen, J.-P. Jones and M. C. Smart, “Factors Limiting Li+ Charge Transfer Kinetics in Li-Ion Batteries,” *Journal of the Electrochemical Society*, vol. 165, pp. A361-A367, 2018.
- [18] G. Kovachev, H. Schrottner, G. Gstrein, L. Aiello, I. Hanzu, H. M. R. Wilkening, A. Foitzik, M. Wellm, W. Sinz and C. Ellersdorfer, “Analytical Dissection of an Automotive Li-Ion Pouch Cell,” *Batteries*, vol. 5, no. 67, 2019.
- [19] EA-Electro-Automatik GmbH, *Datasheet EA PSI-9080 3U*, 2015.
- [20] EA-Elektro-Automatik GmbH, *Datasheet EA EL-9080-340 B*, 2015.
- [21] M. M. Hoque, M. A. Hannan and A. B. Mohamed, “Optimal CC-CV charging of lithium-ion battery for charge equalization controller,” *International Conference on Advances in Electrical, Electronic and Systems Engineering*, 2016.
- [22] F. Saidani, F. X. Hutter, R.-G. Scurtu, W. Braunwarth and J. N. Burghartz, “Lithium-ion battery models: a comparative study and a model-based powerline communication,” *Advances in Radio Science*, vol. 15, pp. 83-91, 2017.
- [23] W. Luo, C. Lv, L. Wang and C. Liu, “Study on Impedance Model of Li-ion Battery,” in *6th IEEE Conference on Industrial Electronics and Applications*, 2011.
- [24] S. S. Madani, E. Schaltz and S. K. Kaer, “An Electrical Equivalent Circuit Model of a Lithium Titanate Oxide Battery,” *Batteries*, vol. 5, no. 31, pp. 1-14, 2019.
- [25] Siemens PLM Software, *Battery Design Studio User Guide*, 2018.
- [26] PalmSens, Compact Electrochemical Interfaces, “Electrochemical Impedance Spectroscopy,” [Online]. Available: <https://www.palmsens.com/electrochemical-impedance-spectroscopy-eis/>.
- [27] E. Dickinson, “Electrochemical Impedance Spectroscopy: Experiment, Model and App,” COMSOL, 9 February 2017. [Online]. Available: <https://www.comsol.com/blogs/electrochemical-impedance-spectroscopy-experiment-model-and-app/>.

- [28] W. Zhao, G. Luo and C.-Y. Wang, "Modeling Nail Penetration Process in Large-Format Li-Ion Cells," *Journal of The Electrochemical Society*, vol. 1, no. 162, pp. A207-A217, 2015.
- [29] T. Yamanaka, Y. Takagishi, Y. Tozuka and T. Yamaue, "Modeling lithium ion battery nail penetration tests and quantitative evaluation of the degree of combustion risk," *Journal of Power Sources*, no. 416, pp. 132-140, 2019.
- [30] Siemens STAR-CCM+, "Tutorial Guide".
- [31] T. Yamauchi, K. Mizushima, Y. Satoh and S. Yamada, "Development of a simulator for both property and safety of a lithium secondary battery," *Journal of Power Sources*, vol. 1, no. 136, pp. 99-107, 2004.
- [32] M. Chen, Q. Ye, C. Shi, Q. Cheng, B. Qie, X. Liao, H. Zhai, Y. He and Y. Yang, "New Insights into Nail Penetration of Li-Ion Batteries: Effects of Heterogeneous Contact Resistance," *Batteries & Supercaps*, no. 2, pp. 874-881, 2019.
- [33] J. Zheng, Y. Xu, X. Gao, J. Zheng, H. He and Z. Li, "Transient Thermal Behaviour of Internal Short-circuit in Lithium Iron Phosphate Battery," *International Journal of Electrochemical Science*, vol. 13, pp. 11620-11635, 2018.